

Design, Analysis, and Testing of a Precision Guidance, Navigation, and Control System for a Dual-Spinning Cubesat

Evan Wise & David Miller

May 2013

SSL # 9-13

Design, Analysis, and Testing of a Precision Guidance, Navigation, and Control System for a Dual-Spinning Cubesat

Evan Wise & David Miller

May 2013

SSL # 9-13

This material is declared a work of the U.S. Government and is not
subject to copyright protection in the United States.

This work is based on the text of the thesis by Evan Wise submitted to the
Department of Aeronautics and Astronautics in partial fulfillment of the requirements for the degree
of Master of Science in Aeronautics and Astronautics at the Massachusetts Institute of Technology.
Typographical corrections to the original text were made in §§1.1, 1.2, 1.3.1, 1.3.2, 1.3.3, 2.1.4, 2.3.2,
2.4, 2.4.1.1, 2.4.1.2, 2.5.1, 3.0, 3.2, 3.1.2, 3.2.2, 3.2.5, 4.1.1.1, 4.2.1, 4.2.2, 4.2.3.1, 4.2.3.2, 4.3, and 7.2.

ABSTRACT

THE MICROSIZED MICROWAVE Atmospheric Satellite (Micromas) combines two traditional control approaches: a dual spinner and a three-axis gyrostat. Unlike typical dual spinners, the purpose of Micromas's 2U bus and spinner assembly is to actuate a 1U payload, not to add gyroscopic stiffness. An orthogonal triple reaction wheel assembly from Maryland Aerospace, Inc., will both counter the angular momentum from the payload and rotate the satellite's bus about its orbit-normal vector to maintain bus alignment with the orbital frame. The payload spins about the spacecraft velocity axis to scan successive swaths of the Earth. However, the CubeSat form factor restricts the velocity axis to be along the spacecraft minor axis of inertia. This orientation leaves the spacecraft at a gravity-gradient-unstable equilibrium. Further, imperfect cancellation of the payload's angular momentum induces nutation behavior. An extended Kalman filter is implemented on a 16-bit PIC24 microcontroller to combine gyroscope, limb sensor, and magnetometer data to provide attitude estimation accuracy of approximately 20 arcminutes. Simulations show that the reaction wheels can consistently maintain pointing to within 30 arcminutes for orbits above 400 kilometers with the payload rotating at 0.8 hertz.

DISCLAIMER: The views expressed in this report are those of the author and do not reflect the official policy or position of the United States Air Force, Department of Defense, or the U.S. Government.

Thesis Supervisor: David W. Miller

Title: Jerome C. Hunsaker Professor of Aeronautics & Astronautics

ACKNOWLEDGMENT

This work was performed primarily under contract P07000180248 with M.I.T. Lincoln Laboratory as part of the Micromas program. The author gratefully thanks the sponsors for their generous support that enabled this research.

CONTENTS

1	<i>Introduction</i>	13
1.1	<i>Motivation</i>	13
1.2	<i>Background</i>	13
1.3	<i>Literature Review</i>	15
1.3.1	<i>Cubesats</i>	15
1.3.2	<i>Dual-Spinners</i>	15
1.3.3	<i>Attitude Estimation</i>	16
1.4	<i>Requirements</i>	16
1.5	<i>Concept of Operations</i>	17
2	<i>Attitude Dynamics</i>	19
2.1	<i>Reference Frames</i>	19
2.1.1	<i>The Inertial Frame</i>	20
2.1.2	<i>The Earth-Fixed Frame</i>	21
2.1.3	<i>The Body-Fixed Frame</i>	22
2.1.4	<i>The Orbital Frame</i>	22
2.2	<i>Equations of Motion</i>	23
2.2.1	<i>Euler's Moment Equations</i>	23
2.2.2	<i>Rotation Matrices and Relative Angular Velocities</i>	25
2.3	<i>Why a Simple Spinner Will Not Work</i>	26
2.3.1	<i>Slewing via an External Torque</i>	26
2.3.2	<i>Constant, Nonzero System Angular Momentum</i>	27

2.4	<i>Dual-Spinner Dynamics</i>	28
2.4.1	<i>Slewing via an External Torque</i>	29
2.4.2	<i>Constant, Nonzero System Angular Momentum</i>	31
2.5	<i>Zero-Angular-Momentum System</i>	33
2.5.1	<i>Linear Stability Analysis</i>	34
2.5.2	<i>Wobble</i>	35
3	<i>Hardware</i>	37
3.1	<i>Actuators</i>	37
3.1.1	<i>Reaction Wheels</i>	37
3.1.2	<i>Magnetic Torque Rods</i>	37
3.1.3	<i>Scanner Assembly Motor</i>	38
3.2	<i>Sensors</i>	38
3.2.1	<i>GPS and Why We Aren't Using It</i>	39
3.2.2	<i>Sun Sensors</i>	39
3.2.3	<i>Magnetic Field Measurement</i>	40
3.2.4	<i>Earth Limb Detection</i>	42
3.2.5	<i>Inertial Measurement Unit</i>	43
3.2.6	<i>Scanner Assembly Encoder</i>	43
3.3	<i>Computational Resources Available to the GNC System</i>	43
4	<i>Estimation and Control Approach</i>	45
4.1	<i>Position Estimation</i>	45
4.1.1	<i>Propagation Methods</i>	45
4.1.2	<i>Practical Considerations</i>	46
4.2	<i>Attitude Estimation</i>	47
4.2.1	<i>Review of Extended Kalman Filter</i>	47
4.2.2	<i>Attitude Parameterizations</i>	48
4.2.3	<i>Propagation</i>	49
4.2.4	<i>Update</i>	52
4.2.5	<i>Square Root and Factored Forms</i>	53

4.3	<i>Attitude Control</i>	54
5	<i>Simulation</i>	57
5.1	<i>Design</i>	57
5.1.1	<i>Dynamics</i>	57
5.1.2	<i>Models Used</i>	58
5.2	<i>Results</i>	59
5.2.1	<i>Detumbling</i>	59
5.2.2	<i>Slew</i>	59
5.2.3	<i>Stabilization</i>	61
5.3	<i>Sensitivity Analysis</i>	64
5.3.1	<i>Scanner Assembly Rotor Bearing Axis Misalignment</i>	64
5.3.2	<i>Gyro Axis Misalignment</i>	64
5.3.3	<i>Magnetometer Misalignment</i>	67
5.3.4	<i>Static Earth Sensor Misalignment</i>	67
6	<i>Testing</i>	71
6.1	<i>Introduction</i>	72
6.1.1	<i>Background</i>	72
6.1.2	<i>Test Item Description</i>	72
6.1.3	<i>Test Objectives</i>	72
6.1.4	<i>Limitations</i>	73
6.1.5	<i>Test Resources</i>	74
6.2	<i>Test and Evaluation</i>	74
6.2.1	<i>General Test Objectives</i>	75
6.2.2	<i>Objective 1: Detumbling Mode</i>	75
6.2.3	<i>Mission Suitability</i>	77
7	<i>Conclusions</i>	79
7.1	<i>Novel Work</i>	79

LIST OF FIGURES

1.1	MICROMAS	14
1.2	Orbit Track and Swath Overlap	14
2.1	Precession of the Equinoxes and Nutation of the Poles	20
2.2	The Body-Fixed Frame	22
2.3	The Local Vertical–Local Horizontal Frame	22
2.4	MICROMAS As a Simple Spinner	26
2.5	MICROMAS Maintaining LVLH Alignment with Constant Momentum	27
2.6	Momentum Trading Between Two Orthogonal Reaction Wheels at Each Quarter Cycle (Clockwise)	28
2.7	MICROMAS as a Partially-Despun Dual Spinner.	29
2.8	Reaction Wheel Required Speeds and Torques	32
2.9	MICROMAS as a Zero-Angular-Momentum System	33
2.10	Unbalanced Spacecraft Geometry	36
3.1	Attitude Sensor Locations on MICROMAS	38
3.2	Relative Rotation Sensor Locations on MICROMAS	39
3.3	Angular Error of Sixth-Order/Degree IGRF Model vs. Thirteenth-Order/Degree IGRF Model	41
3.4	The Voyager Spacecraft	42
4.1	General Estimation Architecture: Complementary Feedback	52
5.1	Detumbling Control History and Angular Rate Trajectory	59
5.2	Slew Mode Angle and Rate Trajectory	60
5.3	Slew Mode Control History	60
5.4	Slew Mode Disturbance Torques	61
5.5	Stabilization Mode Angle and Rate Trajectory	61
5.6	Stabilization Mode Angular Error	62
5.7	Stabilization Mode Control History	63
5.8	Stabilization Mode Bias Error Estimate	64
5.9	RMS Pointing Error Due to Varying Rotor Bearing Axis Misalignment	65

5.10	RMS Reaction Wheel Speed Increase Due to Varying Rotor Bearing Axis Misalignment	65
5.11	RMS Pointing Error Due to Varying Gyro Misalignment	66
5.12	RMS Reaction Wheel Speed Increase Due to Varying Gyro Misalignment	66
5.13	RMS Pointing Error Due to Varying Magnetometer Misalignment	67
5.14	RMS Reaction Wheel Speed Increase Due to Varying Magnetometer Misalignment	68
5.15	RMS Pointing Error Due to Varying Cross-Track Static Earth Sensor Misalignment	68
5.16	RMS Reaction Wheel Speed Increase Due to Varying Cross-Track Static Earth Sensor Misalignment	69
5.17	RMS Pointing Error Due to Varying Anti-Ram Static Earth Sensor Misalignment	69
5.18	RMS Reaction Wheel Speed Increase Due to Varying Anti-Ram Static Earth Sensor Misalignment	70
6.1	MICROMAS ADCS Test Platform	71
6.2	Radiometer Payload Inertia Mockup	72
6.3	Linear Stage Mass Adjusters from the Crowell Testbed	72
6.4	MICROMAS Test Avionics Stack	73
6.5	3-DoF Hemispherical Air Bearing	74
6.6	3-DoF Air Bearing and 3-DoF Helmholtz Cage and Drivers	74
6.7	Revolving Earth Limb Simulator	75

1

INTRODUCTION

1.1 MOTIVATION

THE LITERATURE IS rife with ideas for new filters and sensor models for embedded systems, but there is little floating around that actually discusses practical selection and implementation of these things on a very small spacecraft. Most such papers that do exist deal with spacecraft of entirely different form factors than the small satellites preferred by universities today.¹ Cubesats have neither the flight heritage nor component availability of larger spacecraft. So while the reader may not find any new groundbreaking theories of estimation or control, the reader will find a useful synthesis of estimation and control design for processor-limited embedded systems with limited sensor and actuator choices. The thesis is intended to be a combination survey paper, design document, and record of success and failure.

This paper is targeted specifically at newcomers to the Space Systems Laboratory and more generally at students interested in ADCS for small spacecraft, specifically for spacecraft with limited, embedded computing.

1.2 BACKGROUND

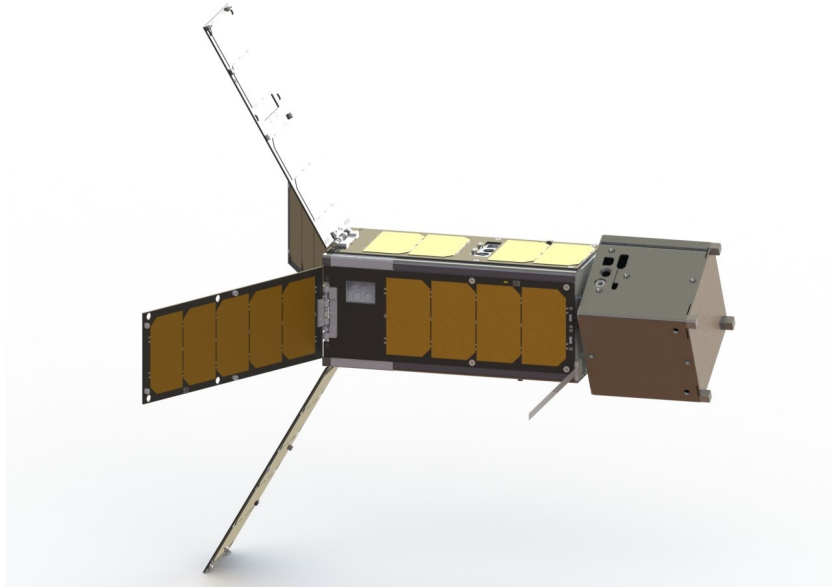
The Micro-sized Microwave Atmospheric Satellite (Micromas) combines two traditional spacecraft control problems: that of a dual spinner and a three-axis gyrostat. Because the scanner assembly, which contains a microwave radiometer for the purposes of all-weather atmospheric sounding,² makes up a comparatively large portion of the spacecraft's mass, it effectively becomes a large rotor such as would be found on a traditional geostationary communications satellite such as INTELSAT IV or the Japanese CS and CS2. Unlike traditional dual spinners, however, the purpose of Micromas's spinner is not to add gyroscopic stiffness.

Rather than for the traditional motivation of added stability, Micromas's arrangement is due to the size limitations of the cubesat form factor: the rotational motion of the scanner allows it to scan the field of view of the payload over adjacent swaths of the Earth's surface and space while the translational mo-

¹ Tisa and Vergez, "Performance Analysis of Control Algorithms for FalconSat-3"; S. Andrews and Morgenstern, "Design, Implementation, Testing, and Flight Results of the TRMM Kalman Filter".

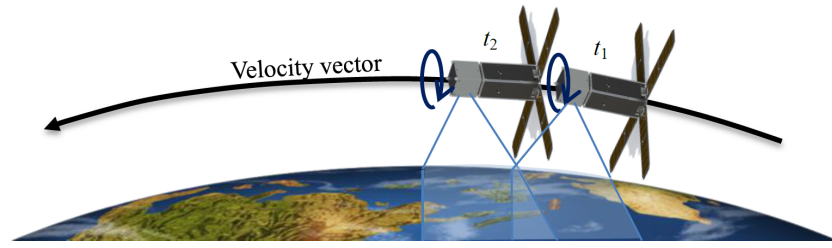
² Blackwell et al., "Improved All-Weather Atmospheric Sounding Using Hyperspectral Microwave Observations".

Figure 1.1: MICROMAS



tion of the satellite through its orbit provides the advancement from swath to swath (see Figure 1.2).

Figure 1.2: Orbit Track and Swath Overlap



Because the payload must be oriented to rotate about the orbital velocity vector throughout the orbit (see Figure 1.2), reaction wheels are needed to both counter the angular momentum from the payload (keeping the bus portion of the spacecraft stationary in the orbital frame) and spin the satellite about its orbit-normal vector to keep the antenna pointing nadir and the payload imaging at nadir.

MICROMAS has three reaction wheels each aligned with a principal axis, a three-axis microelectromechanical system (MEMS) rate gyroscope, two sets of thermopile static Earth limb sensors, a triaxial magnetometer, six coarse sun sensors, and a motor with an optical encoder to rotate the scanner assembly. The reaction wheel assembly, an MAI-400 model, was purchased from Maryland Aerospace, Incorporated, and includes the static Earth sensors as well as a small ARM processor that can accomplish some basic estimation and control tasks. The sun sensors consist of simple photodiodes mounted on six outward

faces of the spacecraft. Most of the spacecraft's estimation and control will be accomplished aboard the spacecraft's primary flight computer, a 16-bit Microchip PIC24 microcontroller. Each of the reaction wheels can be commanded for angular velocity and torque. The rate gyro can determine rotational velocities in all three body axes. The two infrared static Earth sensors between them can determine the nadir vector. The sun sensors can roughly determine the sun vector when the spacecraft is not in eclipse.

Micromas has been designed to a nominal orbit with an inclination of 40 degrees and an altitude of 500 kilometers.

1.3 LITERATURE REVIEW

1.3.1 Cubesats

A cubesat is a satellite form factor developed at California Polytechnic in an attempt to standardize university small satellites and stimulate a market to develop commercial, off the shelf (cots) options for satellite design. Previous cubesats have used passive means of attitude control; a popular solution is permanent magnets to align the satellites with the Earth's magnetic field. The University of Michigan's Radio Aurora Explorer (RAX) uses this option.³ Spacecraft with tighter pointing requirements have used electromagnets. Only recently has technology miniaturization caught up to allow cubesats to employ momentum exchange devices such as reaction wheels. The ExoplanetSat spacecraft uses a two-stage controller with reaction wheels for coarse pointing and a piezoelectric translational stage to position the optics for fine pointing.⁴ Another project called Mothercube uses MEMS electrospray thrusters for individual spacecraft attitude control and multiple spacecraft formation control.

1.3.2 Dual-Spinners

Traditional spinning spacecraft were used for communications. The addition of a despun platform resulted in what is called a "dual-spinner" design. A significant amount of work was done in the 1960s and 1970s with dual-spinner dynamics.⁵ More recent work has examined system damping due to structural flexibility.⁶ The problem is that all of these papers orient the rotor either with the pitch axis of the spacecraft or with an arbitrary inertial pointing direction, which makes sense when taking advantage of gyroscopic stiffness, but does not correspond to Micromas's arrangement. None of the nadir-pointing configurations studied mounted the spinner in the along-track direction.

Communications satellite companies examined problems with spinner balancing in the late 1960s and early 1970s. At Hughes, McIntyre and Gianelli dealt with the wobble that results from imperfectly aligned principal axes of inertia and rotation axes. They describe an exact solution for a platform that is symmetric about the axis of rotation and approximate solutions for asymmetric rotors and platforms.⁷ At Telesat Canada, Wright proposed a system of movable

³ Springmann et al., "The Attitude Determination System of the RAX Satellite".

⁴ Pong et al., "High-Precision Pointing and Attitude Determination and Control on ExoplanetSat".

⁵ See, for example, Likins, "Attitude Stability Criteria for Dual Spin Spacecraft"; Phillips, "Linearization of the Closed-Loop Dynamics of a Dual-Spin Spacecraft".

⁶ Ortiz, "Evaluation of Energy-Sink Stability Criteria for Dual-Spin Spacecraft".

⁷ McIntyre and Gianelli, "Bearing Axis Wobble for a Dual Spin Vehicle".

⁸ Wright, “Wobble Correction for a Dual-Spin Vehicle”.

masses for altering the balance of the rotor on orbit.⁸

1.3.3 Attitude Estimation

Recursive least-squares estimation has a long history with spaceflight. The Apollo Guidance Computer used a variation of a square-root information filter for attitude determination, updating gyro biases with angles measured from pointable optical telescopes.⁹ The Multimission Modular Spacecraft (MMS) demonstrated several advances in quaternion estimation in 1978,¹⁰ and its primary Kalman filter algorithm was summarized and explained by Lefferts, Markley, and Schuster in 1982.¹¹

This attitude determination and control system (ADCS) used an inertial measurement unit (IMU), with two star trackers and a fine sun sensor to update the integrated angle errors and gyro biases. The MMS used a first-order quaternion propagation with a 256-millisecond timestep. Crassidis and Junkins extended the algorithm to the discrete-discrete case in their book¹² using the power series approach given by Markley.¹³ This type of filter (and in fact the same software) was subsequently used in the Rossi X-Ray Timing Explorer and thence adapted for the Tropical Rainfall Measuring Mission (TRMM) for use with a triaxial magnetometer and additional sun sensor.¹⁴

The Triaxial Attitude Determination (TRIAD) method was first developed at the Applied Physics Laboratory and published in 1964 for combining a solar vector measurement with another vector measurement. When Grace Wahba posed her eponymous least-squares single-frame attitude estimation problem in 1965,¹⁵ interest exploded in attitude determination methods, and many variations of many methods were developed to combine attitude information.¹⁶ Tangyun and Shuster summarize the different variations of the TRIAD method.¹⁷

In addition to the sun sensor–magnetometer extended Kalman filter, the TRMM also has an alternative attitude determination mode that uses four static Earth sensors and two digital Sun sensors.¹⁸ It uses a more optimal method than TRIAD to combine the measurements, but results should be analogous to Micromas.

1.4 REQUIREMENTS

The geolocation requirement for Micromas’s payload data is that the total geolocation error of the observations shall be less than 30 percent of the effective pixel diameter (10 percent goal). Since the beamwidth of the spacecraft’s payload is 2.4 degrees, this effectively translates to an error of less than 14.4 arcminutes goal (0.24 degrees) and 43.2 arcminutes threshold (0.72 degrees).

Given the errors introduced from timing and the scanner assembly encoder, the ADCS is left with a threshold requirement of 30 arcminutes pointing knowledge with a goal of 10 arcminutes, and a threshold requirement for pointing of 60 arcminutes with a goal of 30 arcminutes.

⁹ Bill Widnall, personal conversation, 14 March 2013; Don Eyles, personal conversation, 9 April 2013; and Mindell, *Digital Apollo*, p. 103.

¹⁰ Murrell, “Precision Attitude Determination for Multimission Spacecraft”.

¹¹ Lefferts, Markley, and Shuster, “Kalman Filtering for Spacecraft Attitude Estimation”.

¹² Crassidis and Junkins, *Optimal Estimation of Dynamic Systems*, pp. 457–60.

¹³ Markley, “Matrix and Vector Algebra”, p. 755.

¹⁴ S. Andrews and Morgenstern, “Design, Implementation, Testing, and Flight Results of the TRMM Kalman Filter”; S. F. Andrews, Bilanow, and F. Bauer, “Recent Flight Results of the TRMM Kalman Filter”.

¹⁵ Wahba, “A Least Squares Estimate of Satellite Attitude”.

¹⁶ An overview of the main forms of these methods is available in Markley and Mortari, “How to Estimate Attitude from Vector Observations”; Bar-Itzhack and Oshman, “Attitude Determination from Vector Observations”, See also; Markley and Mortari, “New Developments in Quaternion Estimation from Vector Observations”; Markley and F. H. Bauer, *Spacecraft Attitude Determination Methods*; and Markley, “Optimal Attitude Matrix from Two Vector Measurements”.

¹⁷ Tangyun and Shuster, “The Many TRIAD Algorithms”.

¹⁸ Natanson and Glickman, “A Study of TRMM Static Earth Sensor Performance Using On-Orbit Sensor Data”.

In addition to the above, there is a requirement for payload operation during eclipse, so the spacecraft cannot rely on sun sensors for precise attitude determination. While it is possible to rely on gyro propagation during the period of eclipse, the sorts of gyros with the drift rates that could handle the required precision are far outside the budget of Micromas. Thus, the spacecraft must rely on other celestial reference points, such as the stars or Earth.

1.5 CONCEPT OF OPERATIONS

After launch, the spacecraft will deploy from a Poly-Picosatellite Orbital Deployer (P-POD), wait thirty minutes, and use a nichrome burn wire to release the deployable solar panels and monopole antenna. Then the spacecraft will enter the detumbling mode, using a B-dot controller to damp the spacecraft's angular rotation. When the spacecraft has slowed to within the angular rate of change of the geomagnetic field, the spacecraft will enter its slew mode, where it will use its magnetometer and coarse sun sensors to determine attitude and the reaction wheels to slew to align itself with the local-vertical, local-horizontal (LVLH) frame. When the limb is in the field of view of the static Earth sensors, the spacecraft will switch to stabilization mode, spin up the scanner assembly, and begin collecting data with the payload.

2

ATTITUDE DYNAMICS

« Πρός τι δὲ τὰ τοιαῦτα λέγεται, ὅσα αὐτὰ ἀπερ ἐξὶν ἔτέρων εἶναι λέγεται, ἢ ὅπωσδην ἄλλως πρὸς ἔτερον.... ἔξι δὲ καὶ τὰ τοιαῦτα τῶν πρὸς τι oίνον ἔξι, διάθεσις, αἴσθησις, ἐπισήμη, θέσις. πάντα γὰρ τὰ εἰρημένα αὐτὰ ἀπερ ἐξὶν ἔτέρων εἶναι λέγεται καὶ οὐκ ἄλλο τι· ἡ γὰρ ἔξι τινὸς ἔξις λέγεται καὶ ἡ ἐπιστήμη τινὸς ἐπισήμη καὶ ἡ θέσις τινὸς θέσις, καὶ τὰ ἄλλα δὲ ὥσαύτως. »

Those things are called relative, which, being either said to be of something else or related to something else, are explained by reference to that other thing.... There are, moreover, other relatives, e.g. habit, disposition, perception, knowledge, and attitude. The significance of all these is explained by a reference to something else and in no other way. Thus, a habit is a habit of something, knowledge is knowledge of something, attitude is the attitude of something. So it is with all other relatives that have been mentioned.

—Aristotle¹, *Categories*

ANALYSIS OF THE SPACECRAFT’s dynamics allows for a more educated design of ADCS architecture and thus eases the component selection process. The analyses in this chapter also provide a basis to which we can relate subsequent simulation and test results.

¹ trans. E.N. Edgehill, Oxon., 1928; emphasis added by the author. It is interesting to note that *θέσις*, the Greek word for attitude or position, is the same word *thesis* that has come to mean an academic stance and the discussion supporting such.

2.1 REFERENCE FRAMES

As Aristotle noted above, for the attitude of one object to make sense, it must be compared against the attitude of some other object. In the case of an Earth-observing spacecraft, that “something else” is usually the Earth; and so we must define how we are measuring the orientation of the Earth’s reference frame as well as the orientation of the spacecraft’s reference frame. Additionally, since Newton requires an inertial reference frame for us to use calculus properly, we must determine the orientation of the inertial reference frame relative to the Earth’s reference frame.

2.1.1 The Inertial Frame

² In antiquity, this vector pointed to the star γ Arietis (proper name Mesarthim), in the constellation Aries. Because of this alignment, the vernal equinox direction is frequently represented by the astrological symbol for the constellation Aries, the ram's head γ . Because of equinoctial precession, this vector moved into Pisces λ around 70 BC. Regardless, the vernal equinox direction is still frequently called the first point of Aries.

³ Bate, Mueller, and White, *Fundamentals of Astrodynamics*, p. 105.

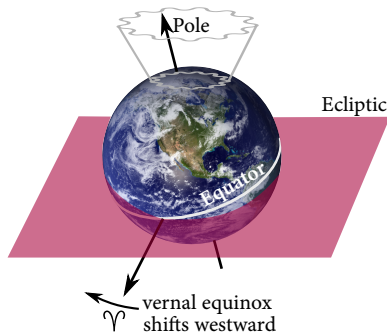


Figure 2.1: Precession of the Equinoxes and Nutation of the Poles. Adapted from Figure 2.9-2 of Bate, Mueller, and White, *Fundamentals of Astrodynamics*, p. 105.

⁴ This mean-of-date frame used less precise precession and nutation models from today. It was originally adopted under the IAU's 1976 resolutions and subsequently modified to use the Fifth Fundamental Catalog (FK5) of celestial objects as fiducial points to define the system.

⁵ Vallado and McClain, *Fundamentals of Astrodynamics and Applications*, p. 160; *The Astronomical Almanac*, p. B25.

The geocentric equatorial reference system (commonly called simply “IJK”) at first examination seems simple: it is centered at the Earth’s center (i.e., geocentric) and has a fundamental plane aligned with the Earth’s equator (i.e., equatorial). Because of this positioning, it is also known as the Earth-centered inertial (ECI) frame. Its primary axis, along \hat{i} , passes through the equator to point at the Sun during the northern hemisphere’s vernal equinox (the first day of spring, wherein the lengths of day and night are equal)—this line also corresponds with the intersection of the Earth’s equatorial plane and the ecliptic plane.² Its second direction, \hat{j} , is normal to the first, similarly passing through the equator, and its third direction, \hat{k} , is oriented along with the geographic north pole, forming a dextral, orthonormal system.

Contention arises when considering that the traditionally-defined geocentric equatorial frame is not, in fact, inertial. The equatorial plane of the Earth is tilted 23.5 degrees relative to the ecliptic plane, causing the equinox to precess; the Earth’s polar axis sweeps out the shape of a cone similar to a wobbling top. The period of this motion is about 26,000 years. Additionally, tidal forces from the moon add an additional perturbation, causing a nutation of the Earth’s motion with a period of 18.6 years.³ This motion is illustrated in Figure 2.1.

The traditional way to account for this effect in astronomical observations is to refer to the locations of the mean equinox and equatorial plane within a certain duration from a particular time, or *epoch*; astrodynamists can achieve a pseudo-inertial frame close enough to a Newtonian inertial system for practical use. This resulting approximation of the equinox at a particular epoch is called a mean-of-date system. The most recent frame of this sort was under the IAU-76/FK5 reference system, using the J2000 epoch (i.e., the location of the mean equator and equinoxes on 1.5 January AD 2000).⁴

The currently accepted geocentric inertial coordinate frame of the International Astronomical Union (IAU) is the Geocentric Celestial Reference Frame (GCRF), adopted with the IAU 2000 resolutions.⁵ Its axes correspond closely to those from the previously accepted IAU-76/FK5 system with the J2000 mean equator and equinox, though it is far “more inertial”: the GCRF’s axes are time-independent and aligned with the International Celestial Reference Frame (ICRF) radio source catalog with its primary axis aligned with a stationary extragalactic radio source, 3C 273, rather than the changing equatorial plane.

For analytical purposes, the mean-of-date system with the epoch at launch should be sufficient, since it results in errors of only arcminutes over the one-year design lifetime of Micromas, which is an order of magnitude smaller than the attitude determination requirements. For precision work, such as for precision orbit determination to geolocate the payload data, the GCRF should be used.

Planetary and stellar ephemerides are described in this reference frame. Abbreviated mean-of-date analytical models are accurate to within an arcminute

for the Sun⁶ (used aboard the spacecraft for attitude determination), and 18 arcminutes for the Moon⁷ (useful for modelling third-body gravitational effects and albedo but not necessary for attitude determination). The most accurate ephemerides are compiled by the Jet Propulsion Laboratory from observational data and are specifically based in a solar-system barycentric form of the ICRF. The DE405 ephemerides are those used for the *Astronomical Almanac*, and are precise to within about 1 milliarcsecond for the inner planets and 100 milliarcseconds for the outer planets⁸—this precision is completely unnecessary for any precision orbit determination modelling or attitude modelling for Micromas.

Because this reference frame is inertial, it is the one with respect to which changing quantities are differentiated and integrated.

2.1.2 The Earth-Fixed Frame

While similar to the ECI frame, the Earth-centered, Earth-fixed (ECEF) frame rotates with the Earth rather than remaining fixed in inertial space. Under the mean-of-date system, the transformation between the ECI frame and the ECEF is a single rotation based on the elapsed time and the mean rotation rate of the Earth. Such a rotation does not account for nutation, precession, or polar motion of the Earth, which can cause errors on the order of tens of kilometers in low Earth orbit.⁹

The International Terrestrial Reference Frame (ITRF2008) is the IAU's terrestrial frame of choice and is periodically updated based on changes in monitoring station locations due to plate tectonics. The U.S. Department of Defense prefers the WGS-84 terrestrial system, which bases its definition on measurements through the Global Positioning System (GPS). Over the years that the ITRF and WGS-84 have been in use, measurement methods (including GPS positioning of the groundstation locations) have converged such that negligible difference (centimeters at Earth's surface) exists between the two systems.¹⁰ With the divorce of the GCRF from an equatorial basis, a more involved transformation must account for the precession and nutation of the Earth through *Earth orientation parameters* (EOPs) in addition to the instantaneous time at the prime meridian (a function of terrestrial time, rather than universal time).

Analysis performed at U.C. Boulder suggests that for positional accuracy on the order of hundreds of meters at LEO, the transformation between the GCRF and ITRF, no EOPs need be used; for accuracy on the order of tens of meters at LEO, only the difference between universal time and coordinated universal time need be accounted for.¹¹

Earth atmospheric, magnetospheric, and gravity models are all described in this reference frame.

⁶ *The Astronomical Almanac*, p. c5; Vallado and McClain, *Fundamentals of Astrodynamics and Applications*, pp. 279–80.

⁷ *The Astronomical Almanac*, p. D22; Vallado and McClain, *Fundamentals of Astrodynamics and Applications*, p. 289.

⁸ Standish, “JPL Planetary and Lunar Ephemerides, DE405/LE405”.

⁹ Bradley et al., “Earth Orientation Parameter Considerations for Precise Spacecraft Operations”.

¹⁰ *The Astronomical Almanac*, p. K13.

¹¹ Bradley et al., “Earth Orientation Parameter Considerations for Precise Spacecraft Operations”.

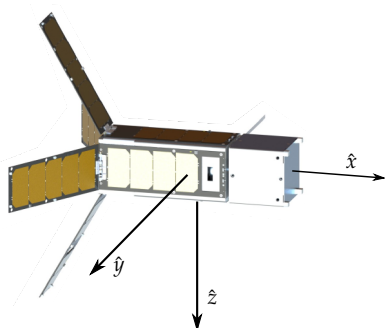


Figure 2.2: The Body-Fixed Frame

2.1.3 The Body-Fixed Frame

Another set of unit vectors $\{\hat{x}, \hat{y}, \hat{z}\}$ constitutes the basis for the body-fixed reference frame \mathcal{F}_B , centered at the center of mass of the spacecraft. The primary axis corresponds to the long axis of the spacecraft, the minor axis of inertia, which should nominally be in the ram, or velocity, direction; the second axis corresponds to the nominal cross-track direction; and the third axis corresponds to the nominal nadir direction (see Figure 2.2).

Ideally, this reference frame would be aligned with the principal axes of the spacecraft, i.e., those axes for which the principal moments of inertia are the diagonal of the inertia tensor and the coupled products of inertia are zero. However, designing the structure requires fitting often oddly-shaped components into a limited area, unevenly distributing the mass across the spacecraft's cross section, and leaving these products of inertia with small, nonzero values. Small trim masses can mitigate this effect, but not entirely remove it. Thus, there is a small rotation between the geometric body frame, to which the sensors and actuators are (nominally) aligned, and the principal axis body frame, to which the mass is aligned. Preliminary analysis will consider the two body frames to be equivalent.

2.1.4 The Orbital Frame

The orbital along-track reference frame with unit vectors $\{\hat{R}, \hat{S}, \hat{W}\}$ travels with the spacecraft like the body frame, but rotates based on the spacecraft's orbital characteristics. Its primary direction \hat{R} is in the radial direction from the center of the Earth to the satellite, \hat{S} is the along-track axis—perpendicular to the radial axis, and parallel to the velocity axis for circular orbits—and \hat{W} is normal to the orbital plane (see Figure 2.3).

The orbital frame is often called the “local vertical–local horizontal” frame because of this satellite-fixed, directional basis. A commonly used variant of the LVLH frame is the roll–pitch–yaw coordinate system (RPY). The roll axis is the same as the \hat{S} axis of the along-track system, the yaw axis is opposite the position vector \hat{R} (i.e., it points nadir), and the pitch axis is opposite the angular momentum vector of the orbit. Because of the more intuitive nature of the RPY reference frame (analogous to the wind-axis reference frame used in aviation), the spacecraft's attitude maneuvers can be described between the body frame and the LVLH frame using a 3–2–1 Euler-axis rotation sequence with Euler angles that measure bank angle (ϕ), elevation (θ), and heading (ψ).¹² Perturbations from the nominal orientation are called roll ($\delta\phi$), pitch ($\delta\theta$), and yaw ($\delta\psi$). Kuipers calls this 3–2–1 sequence the *Aerospace Sequence*,¹³ and Wie prefers it when discussing LVLH maneuvers and derivations.¹⁴ The 3–1–3 sequence is also popular for spacecraft applications, especially for spinning spacecraft and inertial pointing systems that do not consider a local vertical–local horizontal frame.¹⁵ Since Micromas is nominally aligned with the LVLH frame, we will stick to the Aerospace Sequence.

¹² Vallado and McClain, *Fundamentals of Astrodynamics and Applications*, p. 163.

¹³ Kuipers, *Quaternions and Rotation Sequences*, p. 84.

¹⁴ Wie, *Space Vehicle Dynamics and Control*, p. 388.

¹⁵ Wie, *Space Vehicle Dynamics and Control*, p. 365; Markley, “Equations of Motion”.

2.2 EQUATIONS OF MOTION

This section will derive the equations of motion for the most complex satellite design considered for Micromas, i.e., a dual-spinning spacecraft with three additional orthogonally-mounted reaction wheels. The subsequent analysis sections will use simplified versions of the equations of motion, removing terms as components are removed.

These investigations will use the MAI-400 reaction wheel set as a functionally representative example of available cubesat-sized momentum storage devices. Chapter 3 will examine commercial options for such devices in greater detail. The spacecraft's payload and reaction wheels are assumed to be perfectly axisymmetric. The principal axis system is assumed to align with the geometric axis system.

2.2.1 Euler's Moment Equations

The first principle from which our equations of motion will be developed is the rotational analogue of Newton's second law:

$$\frac{d}{dt} \{\vec{H}\}^I = \vec{\tau}_{\text{ext}} \quad (2.1)$$

Since the rotating reference frame, the body frame, is determined based on the rotation of the spacecraft's bus, the angular velocity of the bus $\vec{\omega}_B$ is equal to that of the angular velocity of the body frame with respect to the inertial frame, i.e., $\vec{\omega}_B = \vec{\omega}^{B/I}$. The Micromas spacecraft itself has five individual but connected components that contribute to its angular momentum: the LVLH-stationary bus, \vec{H}_B ; the three reaction wheels, \vec{H}_{RW_i} for $i = 1, 2, 3$; and the rotating payload, \vec{H}_{PL} . Thus

$$\vec{H} = \vec{H}_B + \vec{H}_{PL} + \sum_{i=1}^3 \vec{H}_{RW_i} \quad (2.2)$$

For ease of notation, we will write the sum $\sum_{i=1}^3 \vec{H}_{RW_i}$ as simply \vec{H}_{RW} . If we assume each reaction wheel is perfectly orthogonal to the others, then each component of \vec{H}_{RW} can be thought to represent the angular momentum of each reaction wheel.

Equation 2.3 below explains the derivative of the left-hand side of Equation 2.1 in the spacecraft's body reference frame. Note the Coriolis term taking into account the rotation of the body frame.

$$\frac{d}{dt} \{\vec{H}\}^I = \frac{d}{dt} \{\vec{H}\}^B + \vec{\omega}^{B/I} \times \vec{H} \quad (2.3)$$

Again for ease of notation, and to save space, we will write time derivatives with respect to the body frame—that is in Leibniz notation, $\frac{d}{dt} \{\cdot\}^B$, where \cdot is some generic vector—as an overhead dot in Newton notation: $\dot{\cdot}$. Substituting Equa-

tion 2.3 into Equation 2.1 yields

$$\begin{aligned}\dot{\vec{H}}_B + \dot{\vec{H}}_{PL} + \dot{\vec{H}}_{RW} + \vec{\omega}^{B/I} \times (\vec{H}_B + \vec{H}_{PL} + \vec{H}_{RW}) &= \vec{\tau}_{ext} \\ \dot{\vec{H}}_B + \dot{\vec{H}}_{PL} + \dot{\vec{H}}_{RW} + \vec{\omega}^{B/I} \times \vec{H}_B + \vec{\omega}^{B/I} \times \vec{H}_{PL} + \vec{\omega}^{B/I} \times \vec{H}_{RW} &= \end{aligned}\quad (2.4)$$

The angular momentum of an object is given by

$$\vec{H} = \vec{J} \cdot \vec{\omega} \quad (2.5)$$

where \vec{J} is the inertia dyadic of the object; the time derivative of the angular momentum is thus

$$\dot{\vec{H}} = \dot{\vec{J}} \cdot \vec{\omega} + \vec{J} \cdot \dot{\vec{\omega}} \quad (2.6)$$

Since we are assuming that the reaction wheels and payload are axisymmetric, their inertia dyadics \vec{J}_{RW} and \vec{J}_{PL} do not change during operation. The only inertia dyadic in the system that will change is that of the bus when the solar panels deploy. Since we are examining nominal operation, we can ignore this $\dot{\vec{J}}_B$ term as well. Substituting Equations 2.5 and 2.6 into Equation 2.4 yields the vector form of Euler's moment equation for our spacecraft:

$$\dot{\vec{J}}_B \cdot \dot{\vec{\omega}}^{B/I} + \dot{\vec{J}}_{PL} \cdot \dot{\vec{\omega}}_{PL} + \dot{\vec{J}}_{RW} \cdot \dot{\vec{\omega}}_{RW} + \vec{\omega}^{B/I} \times \dot{\vec{J}}_B \cdot \vec{\omega}^{B/I} + \vec{\omega}^{B/I} \times \dot{\vec{J}}_{PL} \cdot \vec{\omega}_{PL} + \vec{\omega}^{B/I} \times \dot{\vec{J}}_{RW} \cdot \vec{\omega}_{RW} = \vec{\tau}_{ext} \quad (2.7)$$

where the payload and reaction wheel angular velocities ($\vec{\omega}_{PL}$ and $\vec{\omega}_{RW}$) contain the angular motion of the body frame $\vec{\omega}^{B/I}$ as well as their own motions relative to the body frame ($\vec{\Omega}_{PL}$ and $\vec{\Omega}_{RW}$):

$$\vec{\omega}_{PL} = \vec{\omega}^{B/I} + \vec{\Omega}_{PL} \quad (2.8a)$$

$$\vec{\omega}_{RW} = \vec{\omega}^{B/I} + \vec{\Omega}_{RW} \quad (2.8b)$$

Since the angular momentum term derivatives $\dot{\vec{\Omega}}_{RW}$ and $\dot{\vec{\Omega}}_{PL}$ were differentiated with respect to the body frame, we can treat them as internal torques applied to the spacecraft body by the wheels $\vec{\tau}_{RW}$ and spinning payload $\vec{\tau}_{PL}$. If we additionally let $\vec{J} = \vec{J}_B + \vec{J}_{PL} + \vec{J}_{RW}$ and substitute Equations 2.8 into Equation 2.7, this reduces to

$$\underbrace{\vec{J} \cdot \dot{\vec{\omega}}^{B/I} + \vec{\omega}^{B/I} \times \vec{J} \cdot \vec{\omega}^{B/I} + \vec{\tau}_{PL} + \vec{\omega}^{B/I} \times \vec{J}_{PL} \cdot \vec{\Omega}_{PL} + \vec{\tau}_{RW} + \vec{\omega}^{B/I} \times \vec{J}_{RW} \cdot \vec{\Omega}_{RW}}_{\text{System Terms}} + \underbrace{\vec{\tau}_{PL} + \vec{\tau}_{RW}}_{\text{Payload Terms}} + \underbrace{\vec{\omega}^{B/I} \times \vec{J}_{RW} \cdot \vec{\Omega}_{RW}}_{\text{Reaction Wheel Terms}} = \vec{\tau}_{ext} \quad (2.9)$$

¹⁶ In a given frame F, the inertia tensor (also called inertia matrix) of a body J^F is related to the inertia dyadic of that body \vec{J} by the relation

$$\vec{J} = f^T J^F f$$

where f is the basis vector for F

Since we assumed the principal axis frame aligns with the geometric frame, the inertia tensor expressed in the body frame¹⁶ for each part of the system should be diagonal, i.e., $J = \text{diag}(J_x, J_y, J_z)$. We can thus write Equation 2.9 in matrix form as a system of Euler's equations of motion, describing rotations about each

of the spacecraft's principal axes:

$$\underbrace{\begin{bmatrix} \tau_{\text{ext}_x} \\ \tau_{\text{ext}_y} \\ \tau_{\text{ext}_z} \end{bmatrix}}_{\text{External Torques}} = \underbrace{\begin{bmatrix} J_x \dot{\omega}_x \\ J_y \dot{\omega}_y \\ J_z \dot{\omega}_z \end{bmatrix}}_{\text{Whole Spacecraft Terms}} + \underbrace{\begin{bmatrix} (J_z - J_y) \omega_y \omega_z \\ (J_x - J_z) \omega_x \omega_z \\ (J_y - J_x) \omega_x \omega_y \end{bmatrix}}_{\text{Payload Spinner Terms}} + \underbrace{\begin{bmatrix} \tau_{\text{PL}} \\ 0 \\ 0 \end{bmatrix}}_{\text{}} + \underbrace{\begin{bmatrix} 0 \\ J_{\text{PL}} \Omega_{\text{PL}} \omega_z \\ -J_{\text{PL}} \Omega_{\text{PL}} \omega_y \end{bmatrix}}_{\text{}} + \underbrace{\begin{bmatrix} \tau_{\text{RW}_x} \\ \tau_{\text{RW}_y} \\ \tau_{\text{RW}_z} \end{bmatrix}}_{\text{}} + \underbrace{\begin{bmatrix} J_{\text{RW}} (\Omega_{\text{RW}_z} \omega_y - \Omega_{\text{RW}_y} \omega_z) \\ J_{\text{RW}} (\Omega_{\text{RW}_x} \omega_z - \Omega_{\text{RW}_z} \omega_x) \\ J_{\text{RW}} (\Omega_{\text{RW}_y} \omega_x - \Omega_{\text{RW}_x} \omega_y) \end{bmatrix}}_{\text{Reaction Wheel Terms}} \quad (2.10)$$

2.2.2 Rotation Matrices and Relative Angular Velocities

An analysis of Micromas's pointing depends upon the spacecraft's alignment with the local vertical-local horizontal frame. We can use the Aerospace Sequence to get the Euler angles between the spacecraft body frame and the LVLH frame:

$$\mathbf{C}^{\text{B/O}} = \begin{bmatrix} \cos \theta \cos \psi & \cos \theta \sin \psi & -\sin \theta \\ \sin \phi \sin \theta \cos \psi - \cos \phi \sin \psi & \sin \phi \sin \theta \sin \psi + \cos \phi \cos \psi & \sin \phi \cos \theta \\ \cos \phi \sin \theta \cos \psi + \sin \phi \sin \psi & \cos \phi \sin \theta \sin \psi - \sin \phi \cos \psi & \cos \phi \cos \theta \end{bmatrix} \quad (2.11)$$

We can describe the spacecraft's motion relative to the orbital frame by the relation

$$\vec{\omega}^{\text{B/I}} = \vec{\omega}^{\text{B/O}} + \vec{\omega}^{\text{O/I}} \quad (2.12)$$

where, for a circular orbit, the orbital reference frame's angular velocity relative to the inertial frame is simply $-n\hat{\mathbf{o}}_2$, the mean motion of the orbit, which is equivalent to the instantaneous angular velocity over all of the circular orbit. This quantity is

$$n = \sqrt{\frac{\mu_{\oplus}}{a^3}} \quad (2.13)$$

where μ_{\oplus} is the gravitational constant for the Earth and a is the orbit's semimajor axis (which is the radius for circular orbits). For a 500-kilometer orbit, this quantity amounts to

$$n = \sqrt{\frac{398,600.5 \frac{\text{km}^3}{\text{s}^2}}{(6,378.137 \text{ km} + 500 \text{ km})^3}} = 1.1068 \frac{\text{mrad}}{\text{s}}$$

The components of $\vec{\omega}^{\text{B/O}}$ from Equation 2.12 can be expressed in the body frame as

$$\begin{aligned} \boldsymbol{\omega}^{\text{B/O}} &= (\dot{\phi} + \text{Rot}_1(\phi)\dot{\theta} + \text{Rot}_1(\phi)\text{Rot}_2(\theta)\dot{\psi}) \\ &= \begin{bmatrix} 1 & 0 & -\sin \theta \\ 0 & \cos \phi & \sin \phi \cos \theta \\ 0 & -\sin \phi & \cos \phi \cos \theta \end{bmatrix} \begin{bmatrix} \dot{\phi} \\ \dot{\theta} \\ \dot{\psi} \end{bmatrix} \end{aligned} \quad (2.14)$$

and so the components of angular velocity of the body frame with respect to the inertial frame expressed in the body frame are

$$\begin{aligned}\boldsymbol{\omega}^{B/I} &= \boldsymbol{\omega}^{B/O} - n\mathbf{C}^{B/O} \begin{bmatrix} 0 \\ 1 \\ 0 \end{bmatrix} \\ &= \begin{bmatrix} 1 & 0 & -\sin\theta \\ 0 & \cos\phi & \sin\phi\cos\theta \\ 0 & -\sin\phi & \cos\phi\cos\theta \end{bmatrix} \begin{bmatrix} \dot{\phi} \\ \dot{\theta} \\ \dot{\psi} \end{bmatrix} - n \begin{bmatrix} \cos\theta\sin\psi \\ \sin\phi\sin\theta\sin\psi + \cos\phi\cos\psi \\ \cos\phi\sin\theta\sin\psi - \sin\phi\cos\psi \end{bmatrix} \quad (2.15)\end{aligned}$$

For our linear stability analyses, we really only care about small perturbational angles $\delta\phi$, $\delta\theta$, $\delta\psi$, and small perturbational rates $\dot{\phi}$, $\dot{\theta}$, $\dot{\psi}$. We can thus linearize the relationships between the reference frames using the small angle assumption and ignoring higher-order terms. Equation 2.11 becomes

$$\mathbf{C}^{B/O} \approx \begin{bmatrix} 1 & \delta\psi & -\delta\theta \\ -\delta\psi & 1 & \delta\phi \\ \delta\theta & -\delta\phi & 1 \end{bmatrix} \quad (2.16)$$

and Equation 2.15 becomes

$$\omega_x \approx \delta\dot{\phi} - n\delta\psi \quad (2.17a)$$

$$\omega_y \approx \delta\dot{\theta} - n \quad (2.17b)$$

$$\omega_z \approx \delta\dot{\psi} + n\delta\phi \quad (2.17c)$$

Assuming we are also dealing with small perturbational angular accelerations, we can find the time derivatives of Equations 2.17 as

$$\dot{\omega}_x \approx \delta\ddot{\phi} - n\delta\dot{\psi} \quad (2.18a)$$

$$\dot{\omega}_y \approx \delta\ddot{\theta} \quad (2.18b)$$

$$\dot{\omega}_z \approx \delta\ddot{\psi} + n\delta\dot{\phi} \quad (2.18c)$$

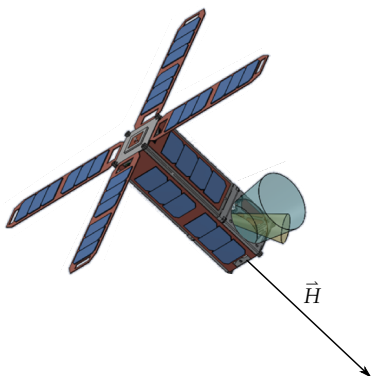


Figure 2.4: Micromas As a Simple Spinner

¹⁷ This type of precession is different from precession usually discussed in classical mechanics, such as in the movement of a top in a gravitational field—for a good explanation, see Markley, “Response to Torques”, p. 498.

2.3 WHY A SIMPLE SPINNER WILL NOT WORK

Momentum-biased systems are often chosen for inertial-pointing applications because the gyroscopic stiffness afforded by the rotating body tends to resist disturbance torques. For Micromas, a momentum-biased system could offer gyroscopic stiffness about the pitch and yaw axes, which would be beneficial in rejecting transient drag effects from varying atmospheric density.

2.3.1 Slewing via an External Torque

Moving the angular momentum of the system requires an external torque (called “precession”;¹⁷ see Equation 2.1). To maintain the spacecraft’s alignment with the LVLH frame, we would need to slew at a rate equal to the angular velocity

of the spacecraft's orbit, which is the mean motion described in Equation 2.13. Determining the magnitude of the required torque τ_{req} to precess a momentum-biased vehicle at this slew rate¹⁸ can be determined with

$$\tau_{\text{req}} = H\omega_{\text{slew}} \quad (2.19)$$

where H is the magnitude of the angular momentum of the rotating system and ω_{slew} is the rate at which we want to slew the system. For a simple spinner, the system's angular momentum is simply its moment of inertia about the axis of rotation J_x times its spin rate Ω_{spin} , which is nominally 0.8 hertz. Substituting this definition along with Equation 2.13 into Equation 2.19 gets us

$$\begin{aligned} \tau_{\text{req}} &= J_x \Omega_{\text{spin}} n \\ &= \left[385.6 \text{ kg}\cdot\text{cm}^2 \left(\frac{1 \text{ m}}{100 \text{ cm}} \right)^2 \right] \left[\left(2\pi \frac{\text{rad}}{\text{cycle}} \right) (0.8 \text{ Hz}) \right] \left(1.1068 \times 10^{-3} \frac{\text{rad}}{\text{s}} \right) \\ &= 0.21452 \text{ mN}\cdot\text{m} \end{aligned} \quad (2.20)$$

for an orbital altitude of 500 kilometers.

Given that our only means of exerting external torque on our spacecraft, short of mounting thrusters, is using the magnetic torque rods, then the most torque we could expect from them can be determined by the product of the maximum available magnetic dipole and the maximum magnetic field we can expect:

$$\begin{aligned} \tau_{\text{magnetic}} &= (0.15 \text{ A}\cdot\text{m}^2) (65 \mu\text{T}) \\ &= 9.75 \mu\text{N}\cdot\text{m} \end{aligned}$$

Thus, slewing in this manner exceeds our actuator capabilities by roughly two orders of magnitude.¹⁹

2.3.2 Constant, Nonzero System Angular Momentum

Since Micromas does not possess enough torque to precess the entire angular momentum bias of a simple spinner, it must leave its angular momentum oriented in a constant direction. Because of this arrangement, a simple spinner version of Micromas must exchange the momentum of the spacecraft between internal storage devices (such as reaction wheels) to maintain proper orientation of the radiometer payload as the spacecraft traverses its orbit.

Figure 2.5 illustrates the changing orientation of Micromas through its orbit despite a constant angular momentum vector. At point (a), because the angular momentum vector is aligned with the orbital along-track vector (the "ram" direction), the momentum storage devices do not have to compensate for the momentum bias. Note that at point (c), the momentum storage device would have to account for *twice* the angular momentum produced by the rotating system. For a simple spinner rotating at 0.8 hertz, this angular momentum would be $2(193.8 \text{ mN}\cdot\text{m}\cdot\text{s}) = 387.6 \text{ mN}\cdot\text{m}\cdot\text{s}$, which is an order of magnitude in excess of the MAI-400 reaction wheel set's momentum storage capability.

¹⁸ Eterno, "Attitude Determination and Control", p. 372.

¹⁹ Additionally, in a low-inclination orbit,

controllability about the pitch axis would be minimal due to the cross-track alignment of the magnetic field.

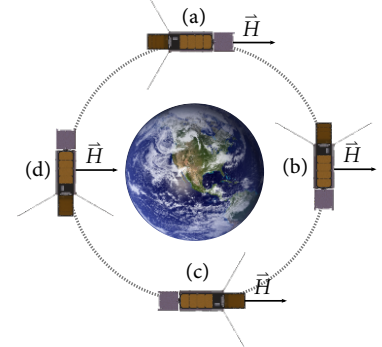


Figure 2.5: Micromas Maintaining LVLH Alignment with Constant Momentum

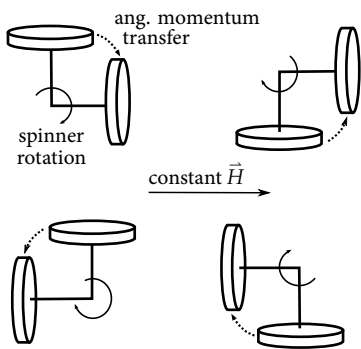


Figure 2.6: Momentum Trading Between Two Orthogonal Reaction Wheels at Each Quarter Cycle (Clockwise)

Additionally, at points (b) and (d) in the orbit, the momentum storage devices must trade between themselves the entirety of the spacecraft's momentum four times during the course of a single rotation of the spacecraft (see Figure 2.6 for a worst-case orientation of two wheels alternately parallel to the angular momentum vector). Because the spacecraft is spinning at 0.8 hertz, this amounts to trading the momentum several times a second, which levies internal torque requirements on the momentum storage devices.

Since the spacecraft is spinning, the reaction wheel speeds would need to be sinusoidally periodic, which would require the sinusoidal application of torque. Since the torque is sinusoidal, any given quarter cycle can represent any other given quarter cycle in the waveform. Because of this similarity, we can examine a single transfer of momentum between wheels as representative of all angular momentum transfers. The time t_{transfer} over which this transfer would take place is a quarter of the period of the spin, or

$$t_{\text{transfer}} = \frac{1}{4} \left(\frac{2\pi}{\Omega_{\text{spin}}} \right) \quad (2.21)$$

If we know we need to transfer $H = 193.8 \text{ mN}\cdot\text{m}\cdot\text{s}$ during this time, we find

$$H = \bar{\tau} t_{\text{transfer}} \quad (2.22)$$

where $\bar{\tau} = \frac{2}{\pi} \tau_{\max}$ is the time-average value of the sinusoidal torque. Rearranging Equation 2.22 and substituting Equation 2.21 yields

$$\begin{aligned} \tau_{\max} &= J_x \Omega_{\text{spin}}^2 \\ &= \left[385.6 \text{ kg}\cdot\text{cm}^2 \left(\frac{1 \text{ m}}{100 \text{ cm}} \right)^2 \right] \left[\left(2\pi \frac{\text{rad}}{\text{cycle}} \right) (0.8 \text{ Hz}) \right]^2 \\ &= 974.3 \text{ mN}\cdot\text{m} \end{aligned} \quad (2.23)$$

which is almost five orders of magnitude greater than the maximum torque available to the MAI-400's reaction wheels. No miniature reaction wheel set could realistically transfer momentum fast enough between its wheels to keep a simple spinner aligned with the LVLH frame.

2.4 DUAL-SPINNER DYNAMICS

In this configuration, only the radiometer payload portion of the spacecraft rotates (see Figure 2.7). This dual-spinner design with a despun platform could both reduce the external torque required to precess the remaining angular momentum (for a precessing system) and also reduce the momentum that the reaction wheels would have to trade (for a constant-momentum system). Working with such a configuration would require slowly spinning up the payload at a rate that the magnetorquers could counter—the external magnetic torque has to balance the internal payload motor torque to keep the platform despun. In addition to reducing the angular momentum of the system, the despun platform

offers a place to mount higher-gain directional antennas for communications and less complex and costly attitude sensors such as static Earth sensors. A despun platform also removes the high torque requirement for trading system momentum between the wheels in a constantly-rotating reaction wheel assembly.

Equation 2.24 gives a dynamical description of the dual-spinner's motion (it is simply Equation 2.10 with the reaction wheel terms removed):

$$\begin{bmatrix} 0 \\ 0 \\ 0 \end{bmatrix} = \begin{bmatrix} J_x \dot{\omega}_x \\ J_y \dot{\omega}_y \\ J_z \dot{\omega}_z \end{bmatrix} + \begin{bmatrix} (J_z - J_y) \omega_y \omega_z \\ (J_x - J_z) \omega_x \omega_z \\ (J_y - J_x) \omega_x \omega_y \end{bmatrix} + \begin{bmatrix} \tau_{PL} \\ 0 \\ 0 \end{bmatrix} + \begin{bmatrix} 0 \\ J_{PL} \Omega_{PL} \omega_z \\ -J_{PL} \Omega_{PL} \omega_y \end{bmatrix} \quad (2.24)$$

To maintain LVLH alignment, the spacecraft's angular velocity must match that of the movement of the LVLH reference frame with respect to the inertial frame. This will result in a secular slew in the spacecraft's pitch axis and perturbational slews in the roll and yaw axes. Substituting Equations 2.17 and 2.18 into Equation 2.24 and ignoring higher-order terms thus yields

$$0 = J_x \delta \ddot{\phi} + n(-J_x + J_y - J_z) \delta \dot{\psi} + n^2 (J_y - J_z) \delta \phi \quad (2.25a)$$

$$-n J_{PL} \Omega_{PL} \delta \phi = J_y \delta \ddot{\theta} + J_{PL} \Omega_{PL} \delta \dot{\psi} \quad (2.25b)$$

$$-n J_{PL} \Omega_{PL} = J_z \delta \ddot{\psi} + n(J_x - J_y + J_z) \delta \dot{\phi} + n^2 (-J_x + J_y) \delta \psi - J_{PL} \Omega_{PL} \delta \dot{\theta} \quad (2.25c)$$

2.4.1 Slewing via an External Torque

We can see the required precession torques on the left side of Equations 2.25. The pitch torque from 2.25b is perturbational in nature, but the yaw torque from 2.25c is predictably constant and follows the form of the predicted precession torque from Equation 2.19.

2.4.1.1 ACTUATOR REQUIREMENTS Unlike the case of the simple spinner, only the payload is rotating, so we need to account for only its moment of inertia, J_{PL} :

$$\begin{aligned} \tau_{prec} &= -n J_{PL} \Omega_{PL} \\ &= \left(1.1068 \times 10^{-3} \frac{\text{rad}}{\text{s}} \right) \left[1.71 \text{ g}\cdot\text{m}^2 \left(\frac{1 \text{ kg}}{1000 \text{ g}} \right) \right] \left[\left(2\pi \frac{\text{rad}}{\text{cycle}} \right) (0.8 \text{ Hz}) \right] \\ &= 9.513 \mu\text{N}\cdot\text{m} \end{aligned}$$

We know from examining the simple spinner case that we can get a maximum of 9.75 microneutron-meters of torque from the magnetorquers. However, precessing the spinner's angular momentum magnetically would not work in all parts of the orbit, since the geomagnetic field is not consistently that strong.

2.4.1.2 LINEAR STABILITY ANALYSIS: PRECESSION If we take the Laplace transform of this system, we can determine the short-term system behavior based on the system poles. Wie performs a similar stability analysis for a simple LVLH-aligned spacecraft subject to gravity-gradient torque. He showed that for small

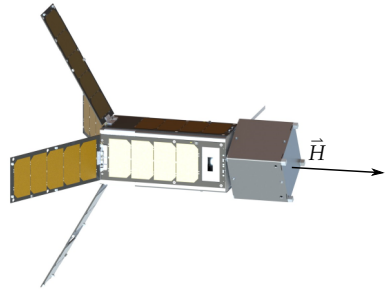


Figure 2.7: Micromas as a Partially-Despun Dual Spinner. Note the smaller angular momentum of this system relative to the simple spinner as shown in Figure 2.4.

angles, the pitch axis stability is decoupled from the roll and yaw axes;²⁰ unfortunately, with the payload momentum bias, this decoupling is no longer the case, as the off-axis terms in Equation 2.25b show. The system is described in the Laplace domain as

$$\begin{bmatrix} 0 \\ 0 \\ -n\frac{J_{PL}}{J_z}\Omega_{PL} \end{bmatrix} = \begin{bmatrix} s^2 + n^2\frac{J_y - J_z}{J_x} & 0 & n\frac{-J_x + J_y - J_z}{J_x}s \\ n\frac{J_{PL}}{J_y}\Omega_{PL} & s^2 & \frac{J_{PL}}{J_y}\Omega_{PL}s \\ n\frac{J_x - J_y + J_z}{J_z}s & -\frac{J_{PL}}{J_z}\Omega_{PL}s & s^2 + n^2\frac{-J_x + J_y}{J_z} \end{bmatrix} \begin{bmatrix} \delta\phi(s) \\ \delta\theta(s) \\ \delta\psi(s) \end{bmatrix} \quad (2.26)$$

Note the forcing term on the left hand side, which is the constant precession torque. We can find the poles of this system by setting the characteristic polynomial to zero; that is, setting the determinant of the dynamics matrix to zero and solving for s . Doing so, we find that

$$s = 0, 0, \pm ni, \pm \sqrt{n^2\left(\frac{-J_y^2}{J_x J_z} + \frac{J_y}{J_z} + \frac{J_y}{J_x} - 1\right) - \frac{J_{PL}^2}{J_y J_z}\Omega_{PL}^2} \quad (2.27)$$

Thence we can derive necessary and sufficient conditions for balancing the spacecraft to achieve marginal stability.

We can also attempt to perform a linear stability analysis of the system as it is affected by environmental torques. At this point, we do not know much about the design and shape of the spacecraft other than its general mass characteristics and alignments, so attempting to quantify torques such as those due to aerodynamic drag or solar radiation pressure becomes impossible, because we do not know about solar panel alignment or antennas. However, the gravity gradient torque depends only upon the inertia characteristics of the system, so we can still see if analyzing gravity gradient torque is a useful pursuit. It is important to note, though, that since the spacecraft will be in LEO, the drag torque may exceed the gravity gradient torque.

$$-3n^2(J_y - J_z)\delta\phi = J_x\delta\ddot{\phi} + n(-J_x + J_y - J_z)\delta\dot{\psi} + n^2(J_y - J_z)\delta\phi \quad (2.28a)$$

$$-nJ_{PL}\Omega_{PL}\delta\phi - 3n^2(J_x - J_z)\delta\theta = J_y\delta\ddot{\theta} + J_{PL}\Omega_{PL}\delta\dot{\psi} \quad (2.28b)$$

$$-nJ_{PL}\Omega_{PL} = J_z\delta\ddot{\psi} + n(J_x - J_y + J_z)\delta\dot{\phi} + n^2(-J_x + J_y)\delta\psi - J_{PL}\Omega_{PL}\delta\dot{\theta} \quad (2.28c)$$

And in Laplace space:

$$\begin{bmatrix} 0 \\ 0 \\ -n\frac{J_{PL}}{J_z}\Omega_{PL} \end{bmatrix} = \begin{bmatrix} s^2 + 4n^2\frac{J_y - J_z}{J_x} & 0 & n\frac{-J_x + J_y - J_z}{J_x}s \\ n\frac{J_{PL}}{J_y}\Omega_{PL} & s^2 + 3n^2\frac{J_x - J_z}{J_y} & \frac{J_{PL}}{J_y}\Omega_{PL}s \\ n\frac{J_x - J_y + J_z}{J_z}s & -\frac{J_{PL}}{J_z}\Omega_{PL}s & s^2 + n^2\frac{-J_x + J_y}{J_z} \end{bmatrix} \begin{bmatrix} \delta\phi(s) \\ \delta\theta(s) \\ \delta\psi(s) \end{bmatrix} \quad (2.29)$$

Setting the determinant of this dynamics matrix to zero and solving for s yields an insoluble mess that is not helpful for determining necessary and sufficient conditions for spacecraft design. Since the maximum gravity gradient torques (which occur at a 45-degree dip angle) should be so much smaller than the required precession torques anyway²¹, this omission should not be a problem.

²¹ $\tau_{max} = -3n^2(J_x - J_z)/\sqrt{2}$
 $= -\frac{3}{\sqrt{2}}(1.1068 \times 10^{-3} \frac{\text{rad}}{\text{s}}) \times$
 $\left[(385.6 - 647.0) \text{ kg}\cdot\text{cm}^2 \left(\frac{1\text{m}}{100\text{cm}}\right)^2\right]$
 $= 67.9 \text{ nN}\cdot\text{m}$

2.4.2 Constant, Nonzero System Angular Momentum

Since we know that precessing the entirety of the system's momentum with the spacecraft's actuators is unrealistic, we can also consider keeping the system's angular momentum constant and trading it between momentum storage devices as the spacecraft rotates. Since we have reaction wheels, our dynamical equation of motion is (assuming a hypothetical infinite-bandwidth controller)

$$\begin{bmatrix} 0 \\ 0 \\ 0 \end{bmatrix} = \begin{bmatrix} J_x \dot{\omega}_x \\ J_y \dot{\omega}_y \\ J_z \dot{\omega}_z \end{bmatrix} + \begin{bmatrix} (J_z - J_y) \omega_y \omega_z \\ (J_x - J_z) \omega_x \omega_z \\ (J_y - J_x) \omega_x \omega_y \end{bmatrix} + \begin{bmatrix} \tau_{PL} \\ 0 \\ 0 \end{bmatrix} + \begin{bmatrix} 0 \\ J_{PL} \Omega_{PL} \omega_z \\ -J_{PL} \Omega_{PL} \omega_y \end{bmatrix} + \begin{bmatrix} \tau_{RW_x} \\ \tau_{RW_y} \\ \tau_{RW_z} \end{bmatrix} + \begin{bmatrix} J_{RW} (\Omega_{RW_z} \omega_y - \Omega_{RW_y} \omega_z) \\ J_{RW} (\Omega_{RW_x} \omega_z - \Omega_{RW_z} \omega_x) \\ J_{RW} (\Omega_{RW_y} \omega_x - \Omega_{RW_x} \omega_y) \end{bmatrix} \quad (2.30)$$

For our triaxial reaction wheel set, we can trade the payload's angular momentum between the roll and yaw axis wheels and use the pitch axis wheel to keep the spacecraft aligned with the LVLH frame:

$$H_{RW_x} = H_{PL} \cos v - H_{PL} \quad (2.31a)$$

$$H_{RW_y} = n J_y \quad (2.31b)$$

$$H_{RW_z} = -H_{PL} \sin v \quad (2.31c)$$

where for a circular orbit the spacecraft's true anomaly $v = nt$. Note that the x and z wheels are a quarter cycle out of phase. We can determine the reaction wheel speeds to command simply by dividing both sides by the reaction wheels' angular momentum:

$$\Omega_{RW_x} = \frac{J_{PL}}{J_{RW}} \Omega_{PL} \cos nt - \frac{J_{PL}}{J_{RW}} \Omega_{PL} \quad (2.32a)$$

$$\Omega_{RW_y} = n \frac{J_y}{J_{RW}} \quad (2.32b)$$

$$\Omega_{RW_z} = -\frac{J_{PL}}{J_{RW}} \Omega_{PL} \sin nt \quad (2.32c)$$

Differentiating Equations 2.31 with respect to time nets us the required reaction wheel torques:

$$\tau_{RW_x} = -n J_{PL} \Omega_{PL} \sin nt \quad (2.33a)$$

$$\tau_{RW_y} = 0 \quad (2.33b)$$

$$\tau_{RW_z} = -n J_{PL} \Omega_{PL} \cos nt \quad (2.33c)$$

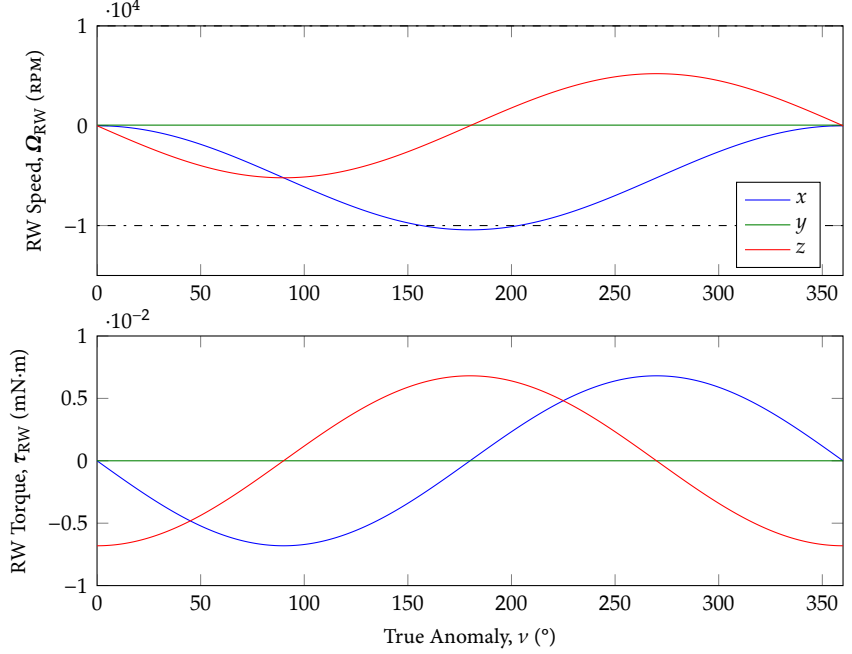
2.4.2.1 ACTUATOR REQUIREMENTS

These required reaction wheel commands are shown in Figure 2.8.

With a despun platform, the reaction wheel assembly does not rotate at 0.8 hertz with the spacecraft body, negating the need for such a high reaction wheel torque requirement as the simple spinner case. Reaction wheel angular momentum storage then becomes the limiting factor. Recalling location (c) in Figure 2.5, the maximum angular momentum that the wheels would need to store

would be twice the angular momentum of the rotating payload— $2(6.2 \text{ mN}\cdot\text{m}\cdot\text{s}) = 12.4 \text{ mN}\cdot\text{m}\cdot\text{s}$ —which, while not an order of magnitude above the available momentum storage, still exceeds the capabilities of the MAI-400's actuators.

Figure 2.8: Reaction Wheel Required Speeds and Torques. Note the required x reaction wheel speed crossing the maximum available speed on $\nu \in (160^\circ, 200^\circ)$.



²² James R. Wertz, “Torque-Free Motion”, p. 490.

2.4.2.2 LINEAR STABILITY ANALYSIS: NUTATION In the absence of external torques, a momentum-biased system is subject to nutation should the axis of rotation become misaligned with a principal axis of the spacecraft.²²

With the sinusoidal description of reaction wheel angular momentum, we cannot perform a linear stability analysis applicable to all points in the orbit; thus we will examine each quarter of the orbit, i.e., the four points from Figure 2.5. We can substitute Equations 2.17, 2.18, 2.32 and 2.33 into Equation 2.30 to obtain kinematic equations of motion for each of the four points in the orbit under review:

Point (a)

$$\begin{aligned} 0 &= J_x \delta \ddot{\phi} + n(-J_x - J_z) \delta \dot{\psi} - n^2 J_z \delta \phi \\ 0 &= J_y \delta \ddot{\theta} + J_{PL} \Omega_{PL} (n \delta \phi + \delta \dot{\psi}) \\ 0 &= J_z \delta \ddot{\psi} + n(J_x + J_z) \delta \dot{\phi} - n^2 J_x \delta \psi - J_{PL} \Omega_{PL} \delta \dot{\theta} \end{aligned}$$

Point (c)

$$\begin{aligned} 0 &= J_x \delta \ddot{\phi} + n(-J_x - J_z) \delta \dot{\psi} - n^2 J_z \delta \phi \\ 0 &= J_y \delta \ddot{\theta} + J_{PL} \Omega_{PL} (-n \delta \phi - \delta \dot{\psi}) \\ 0 &= J_z \delta \ddot{\psi} + n(J_x + J_z) \delta \dot{\phi} - n^2 J_x \delta \psi + J_{PL} \Omega_{PL} \delta \dot{\theta} \end{aligned}$$

Point (b)

$$\begin{aligned} 0 &= J_x \delta \ddot{\phi} + n(-J_x - J_z) \delta \dot{\psi} - n^2 J_z \delta \phi - J_{PL} \Omega_{PL} \delta \dot{\theta} \\ 0 &= J_y \delta \ddot{\theta} + J_{PL} \Omega_{PL} (-n \delta \psi + \delta \dot{\phi}) \\ 0 &= J_z \delta \ddot{\psi} + n(J_x + J_z) \delta \dot{\phi} - n^2 J_x \delta \psi \end{aligned}$$

Point (d)

$$\begin{aligned} 0 &= J_x \delta \ddot{\phi} + n(-J_x - J_z) \delta \dot{\psi} - n^2 J_z \delta \phi + J_{PL} \Omega_{PL} \delta \dot{\theta} \\ 0 &= J_y \delta \ddot{\theta} + J_{PL} \Omega_{PL} (n \delta \psi - \delta \dot{\phi}) \\ 0 &= J_z \delta \ddot{\psi} + n(J_x + J_z) \delta \dot{\phi} - n^2 J_x \delta \psi \end{aligned}$$

And in the Laplace domain:

$$\begin{aligned}
 & \text{Point (a)} \\
 \begin{bmatrix} 0 \\ 0 \\ 0 \end{bmatrix} &= \begin{bmatrix} s^2 - n^2 \frac{J_z}{J_x} & 0 & n \frac{-J_x - J_z}{J_x} s \\ n \frac{J_{PL}}{J_y} \Omega_{PL} & s^2 & \frac{J_{PL}}{J_y} \Omega_{PL} s \\ n \frac{J_x + J_z}{J_z} s & -\frac{J_{PL}}{J_z} \Omega_{PL} s & s^2 - n^2 \frac{J_x}{J_z} \end{bmatrix} \begin{bmatrix} \delta\phi(s) \\ \delta\theta(s) \\ \delta\psi(s) \end{bmatrix} \quad \begin{bmatrix} 0 \\ 0 \\ 0 \end{bmatrix} = \begin{bmatrix} s^2 - n^2 \frac{J_z}{J_x} & 0 & n \frac{-J_x - J_z}{J_x} s \\ -n \frac{J_{PL}}{J_y} \Omega_{PL} & s^2 & -\frac{J_{PL}}{J_y} \Omega_{PL} s \\ n \frac{J_x + J_z}{J_z} s & \frac{J_{PL}}{J_z} \Omega_{PL} s & s^2 - n^2 \frac{J_x}{J_z} \end{bmatrix} \begin{bmatrix} \delta\phi(s) \\ \delta\theta(s) \\ \delta\psi(s) \end{bmatrix} \\
 & \text{Point (b)} \\
 \begin{bmatrix} 0 \\ 0 \\ 0 \end{bmatrix} &= \begin{bmatrix} s^2 - n^2 \frac{J_z}{J_x} & -\frac{J_{PL}}{J_x} \Omega_{PL} s & n \frac{-J_x - J_z}{J_x} s \\ \frac{J_{PL}}{J_y} \Omega_{PL} s & s^2 & -n \frac{J_{PL}}{J_y} \Omega_{PL} \\ n \frac{J_x + J_z}{J_z} s & 0 & s^2 - n^2 \frac{J_x}{J_z} \end{bmatrix} \begin{bmatrix} \delta\phi(s) \\ \delta\theta(s) \\ \delta\psi(s) \end{bmatrix} \quad \begin{bmatrix} 0 \\ 0 \\ 0 \end{bmatrix} = \begin{bmatrix} s^2 - n^2 \frac{J_z}{J_x} & 0 & n \frac{-J_x - J_z}{J_x} s \\ -\frac{J_{PL}}{J_y} \Omega_{PL} s & s^2 & n \frac{J_{PL}}{J_y} \Omega_{PL} \\ n \frac{J_x + J_z}{J_z} s & 0 & s^2 - n^2 \frac{J_x}{J_z} \end{bmatrix} \begin{bmatrix} \delta\phi(s) \\ \delta\theta(s) \\ \delta\psi(s) \end{bmatrix} \\
 & \text{Point (d)}
 \end{aligned}$$

And setting the characteristic polynomial to zero and solving for s gives us the nutational poles of the system at Points (a)–(d):

$$\text{Points (a) \& (c): } s = 0, 0, \pm ni, \pm \sqrt{-\frac{J_{PL}^2}{J_y J_z} \Omega_{PL}^2 - n^2} \quad (2.34a)$$

$$\text{Points (b) \& (d): } s = 0, 0, \pm ni, \pm \sqrt{-\frac{J_{PL}^2}{J_x J_y} \Omega_{PL}^2 - n^2} \quad (2.34b)$$

Note the switch of the roll and yaw inertiae in the denominators of the last poles between quadrants.

An option not examined would be to counter some portion of the angular momentum produced by the rotating payload and precess the rest with magnetic torque. However, the angular momentum estimator required for such a solution levies additional requirements on computing resources atop those already required for attitude estimation. This solution may be useful if a zero-momentum system proves untenable.

2.5 ZERO-ANGULAR-MOMENTUM SYSTEM

A three-axis-stabilized dual spinner offers most of the advantages of a traditional dual-spinner with a despun platform, e.g., a stationary platform on which to mount attitude sensors and antennas. Additionally, since there is no net angular momentum vector (assuming the controllers for the reaction wheels and payload spinner do well), no torque is required to precess any residual momentum, and nutation does not occur. To effect this sort of system, a momentum storage device in the stationary bus would have to completely counter the angular momentum produced by the rotating payload, such as a reaction wheel coaxial with the payload spinner rotation (see Figure 2.9).

The dynamics of this arrangement are the same as those for the momentum-biased system:

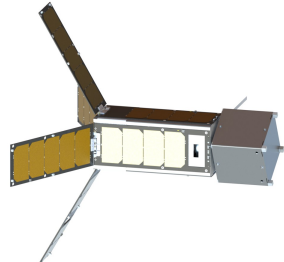


Figure 2.9: Micromas as a Zero-Angular-Momentum System

$$\begin{bmatrix} 0 \\ 0 \\ 0 \end{bmatrix} = \begin{bmatrix} J_x \dot{\omega}_x \\ J_y \dot{\omega}_y \\ J_z \dot{\omega}_z \end{bmatrix} + \begin{bmatrix} (J_z - J_y) \omega_y \omega_z \\ (J_x - J_z) \omega_x \omega_z \\ (J_y - J_x) \omega_x \omega_y \end{bmatrix} + \begin{bmatrix} \tau_{PL} \\ 0 \\ 0 \end{bmatrix} + \begin{bmatrix} 0 \\ J_{PL} \Omega_{PL} \omega_z \\ -J_{PL} \Omega_{PL} \omega_y \end{bmatrix} + \begin{bmatrix} \tau_{RW_x} \\ \tau_{RW_y} \\ \tau_{RW_z} \end{bmatrix} + \begin{bmatrix} J_{RW} (\Omega_{RW_z} \omega_y - \Omega_{RW_y} \omega_z) \\ J_{RW} (\Omega_{RW_x} \omega_z - \Omega_{RW_z} \omega_x) \\ J_{RW} (\Omega_{RW_y} \omega_x - \Omega_{RW_x} \omega_y) \end{bmatrix} \quad (2.35)$$

2.5.1 Linear Stability Analysis

We know that in the zero-momentum system, the angular momenta of the payload scanner assembly and the reaction wheels should counter each other, i.e., $\vec{0} = \vec{H}_{PL} + \vec{H}_{RW}$, or more specifically, $0 = J_{PL} \Omega_{PL} + J_{RW} \Omega_{RW_x}$. In the event that the reaction wheel controller does not perfectly coordinate with the payload spinner controller—such as from quantization error or misalignment of the rotation axes—a small bias momentum $\delta\vec{H} = \vec{H}_{PL} + \vec{H}_{RW}$ could result. If we assume that the bias does not result from misalignment of the rotation axes, we can make some simplifying assumptions for our analysis, specifically $\delta H_x = J_{PL} \delta \Omega_{PL} + J_{RW} \delta \Omega_{RW_x}$. This section will analyze the ramifications of such bias momenta on the stability of the spacecraft.

We want to examine behavior in the presence of a payload momentum offset:

$$\Omega_{PL} = \Omega_{PL_{nom}} + \delta \Omega_{PL} \quad (2.36)$$

Just as with the momentum-biased system, we can determine the reaction wheel speeds from the desired overall momentum:

$$\Omega_{RW_x} = -\frac{J_{PL}}{J_{RW}} \Omega_{PL_{nom}} + \delta \Omega_{RW_x} \quad (2.37a)$$

$$\Omega_{RW_y} = n \frac{J_y}{J_{RW}} + \delta \Omega_{RW_y} \quad (2.37b)$$

$$\Omega_{RW_z} = \delta \Omega_{RW_z} \quad (2.37c)$$

No torques should result from these constant speeds.

We can substitute Equations 2.17, 2.18, 2.36, and 2.37 into Equation 2.35 to obtain a kinematic description of the spacecraft's motion:

$$0 = J_x \delta \ddot{\phi} + n(-J_x - J_z) \delta \dot{\psi} - n^2 J_z \delta \phi - n J_{RW} \delta \Omega_{RW_z} \quad (2.38a)$$

$$0 = J_y \delta \ddot{\theta} \quad (2.38b)$$

$$0 = J_z \delta \ddot{\psi} + n(J_x + J_z) \delta \dot{\phi} - n^2 J_x \delta \psi - n J_{PL} \delta \Omega_{PL} + n J_{RW} \delta \Omega_{RW_x} \quad (2.38c)$$

In the Laplace domain, this becomes

$$\begin{bmatrix} n \frac{J_{RW}}{J_x} \delta \Omega_{RW_z} \\ 0 \\ -n \frac{J_{PL}}{J_z} \delta \Omega_{PL} - n \frac{J_{RW}}{J_z} \delta \Omega_{RW_x} \end{bmatrix} = \begin{bmatrix} s^2 - n^2 \frac{J_z}{J_x} & 0 & n \frac{-J_x - J_z}{J_x} s \\ 0 & s^2 & 0 \\ n \frac{J_x + J_z}{J_z} s & 0 & s^2 - n^2 \frac{J_x}{J_z} \end{bmatrix} \begin{bmatrix} \delta \phi(s) \\ \delta \theta(s) \\ \delta \psi(s) \end{bmatrix} \quad (2.39)$$

and the poles are

$$s = 0, 0, ni, ni, -ni, -ni \quad (2.40)$$

So, the quantization errors do not adversely affect the system's stability, but they could result in a small momentum bias. With the worst-case errors, the required precession torques are

$$\begin{aligned} \tau_x &= n \frac{J_{RW}}{J_x} \delta\Omega_{RW_z} \\ &= \left(1.1068 \times 10^{-3} \frac{\text{rad}}{\text{s}}\right) \frac{1.1268 \times 10^{-5} \text{ kg}\cdot\text{m}^2}{385.6 \text{ kg}\cdot\text{cm}^2 \left(\frac{1 \text{ m}}{100 \text{ cm}}\right)^2} \left[(15^\circ/\text{s}) \left(\frac{\pi \text{ rad}}{180^\circ}\right)\right] \\ &= 84.67 \text{ nN}\cdot\text{m} \\ \tau_z &= -n \frac{J_{PL}}{J_z} \delta\Omega_{PL} - n \frac{J_{RW}}{J_z} \delta\Omega_{RW_x} \\ &= -\left(1.1068 \times 10^{-3} \frac{\text{rad}}{\text{s}}\right) \frac{1.224 \times 10^{-3} \text{ kg}\cdot\text{m}^2}{647.0 \text{ kg}\cdot\text{cm}^2 \left(\frac{1 \text{ m}}{100 \text{ cm}}\right)^2} \left(16.755 \times 10^{-3} \frac{\text{rad}}{\text{s}}\right) \\ &\quad - \left(1.1068 \times 10^{-3} \frac{\text{rad}}{\text{s}}\right) \frac{1.1268 \times 10^{-5} \text{ kg}\cdot\text{m}^2}{647.0 \text{ kg}\cdot\text{cm}^2 \left(\frac{1 \text{ m}}{100 \text{ cm}}\right)^2} \left[(15^\circ/\text{s}) \left(\frac{\pi \text{ rad}}{180^\circ}\right)\right] \\ &= -401.3 \text{ nN}\cdot\text{m} \end{aligned}$$

which are well within the capabilities of the magnetorquers to precess.

2.5.2 Wobble

Work done at Hughes Aircraft in the late 1960s and early 1970s established an analytical framework for dual-spinner wobble caused by bearing-axis misalignment.²³ Further work by Telesat Canada suggested straightforward means for wobble mitigation with adjustable masses; these masses could even be actuated to counter changing inertiae in flight due to propellant expenditure.²⁴ For Micromas, the masses will be trimmed before launch.

We can use the Hughes framework to determine how precisely the masses and inertias need be aligned.

2.5.2.1 STATIC IMBALANCE Static imbalance results from a misalignment ϵ of the bearing spin axis and the center of mass of the rotor. It is described by

$$\epsilon = \frac{\omega_{\text{wobble}} J_y}{\Omega_{PL} m_{PL} r_0} \quad (2.41)$$

where ϵ is the payload rotor's center of mass offset normal to the bearing axis, ω_{wobble} is the maximum allowable wobble rate, m_{PL} is the mass of the payload, and r_0 is the distance between the system center of mass and the ideal center of

²³ McIntyre and Gianelli, "Bearing Axis Wobble for a Dual Spin Vehicle".

²⁴ Wright, "Wobble Correction for a Dual-Spin Vehicle".

mass of the payload rotor. For Micromas, this works out to

$$\epsilon = \frac{\left[1^{\circ}/\text{s} \left(\frac{\pi \text{ rad}}{180^{\circ}}\right)\right] \left[645.7 \text{ kg}\cdot\text{cm}^2 \left(\frac{1 \text{ m}}{100 \text{ cm}}\right)^2\right]}{\left[0.8 \text{ Hz} \left(\frac{2\pi \text{ rad}}{\text{cycle}}\right)\right] (1 \text{ kg})(0.14 \text{ m})} = 1.6 \text{ mm}$$

assuming no other disturbance.

2.5.2.2 DYNAMIC IMBALANCE Dynamic imbalance results from a misalignment δ of the bearing spin axis and a principal axis of inertia of the rotor:

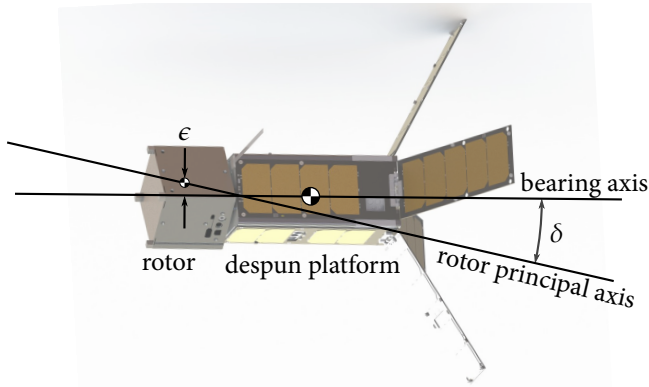
$$\delta = \frac{\omega_{\text{wobble}} J_y}{\Omega_{\text{PL}} (J_{\text{PL}} - J_{\text{PL}_t})} \quad (2.42)$$

where δ is the angle between the rotational principal axis of inertia of the rotor and the bearing spin axis and J_{PL_t} is the transverse moment of inertia of the payload about the payload center of mass. For Micromas, this works out to

$$\delta = \frac{\left[1^{\circ}/\text{s} \left(\frac{\pi \text{ rad}}{180^{\circ}}\right)\right] \left[645.7 \text{ kg}\cdot\text{cm}^2 \left(\frac{1 \text{ m}}{100 \text{ cm}}\right)^2\right]}{\left[0.8 \text{ Hz} \left(\frac{2\pi \text{ rad}}{\text{cycle}}\right)\right] \left[(12 - 29) \text{ kg}\cdot\text{cm}^2 \left(\frac{1 \text{ m}}{100 \text{ cm}}\right)^2\right]} = -7.5^{\circ}$$

assuming no other disturbance.

Figure 2.10: Unbalanced
Spacecraft Geometry



3

HARDWARE

“ Real men do ‘Hardware.’ They also abstain from eating quiche. ”

—Dick Battin¹

¹ With apologies, as this quotation is taken out of context. From Battin, “Some Funny Things Happened on the Way to the Moon”

THIS CHAPTER DETAILS the selection and modelling of the ADCS hardware. The models developed are used as a baseline for testing and characterization, as well as the simulation developed in Chapter 5.

3.1 ACTUATORS

3.1.1 Reaction Wheels

Maryland Aerospace’s MAI-400 reaction wheel assembly contains three orthogonally-mounted reaction wheels and provides enough angular momentum storage to meet the requirements; specifically 11.8 millinewton·meter·seconds:

$$H_{\text{req}} = (1.224 \times 10^{-3} \text{ kg}\cdot\text{m}^2) \left[0.8 \text{ Hz} \left(2\pi \frac{\text{rad}}{\text{cycle}} \right) \right] \\ = 6.2 \text{ mN}\cdot\text{m}\cdot\text{s}$$

which leaves a margin of 48 percent of the x -axis reaction wheel’s capability available after cancelling the payload’s angular momentum.

These reaction wheels were chosen based not only on their superior angular momentum storage capability compared to the rest of the cubesat form factor reaction wheel assemblies on the market but also because of the integrated torque rods and ADCS computer.²

3.1.2 Magnetic Torque Rods

Torque rods are simple electromagnets. Since Micromas is in LEO, the Earth’s magnetic field is sufficiently strong to be able to torque against using these torque rods for the purposes of rate damping during the spacecraft’s detumbling

² More information on this selection can be found in G. Getliffe et al. “Design Review for a Micro-sized Microwave Atmospheric Satellite,” 16.851 Term Paper, Mass. Inst. of Tech., Cambridge, MA, December 2010; and E. Wise, “Micromas Reaction Wheel Trade Study,” v. 1.1, Space Systems Laboratory Report, Mass. Inst. of Tech., Cambridge, MA, 25 October 2011.

mode and momentum dumping from the reaction wheels during the spacecraft's other modes. The torque rods selected are contained within the MAI-400 reaction wheel assembly and offer an effective magnetic dipole of 0.15 ampere·meters² after duty cycling to avoid saturating the magnetometer.

3.1.3 Scanner Assembly Motor

Because of the difficulty of replacing the brushes in a motor that is supposed to operate continuously for a year (and also located in space), the team opted to use a brushless direct current (DC) motor. Motors of this type have long been in use in reaction wheels and control moment gyros.³ Because such motors can exhibit cogging at low rates, the team chose an Aeroflex z-0250-050-3-104 Zero-Cogging Brushless DC Motor with eight poles for more precise position and velocity controllability.

3.2 SENSORS

Upon first examination of Micromas's attitude determination requirements, engineers familiar with space systems would likely suggest using star sensors for attitude estimation.⁴ Unfortunately, no commercial, off-the-shelf (COTS) solutions are available for cubesats within Micromas's desired development schedule.

Figure 3.1: Attitude Sensor Locations on Micromas

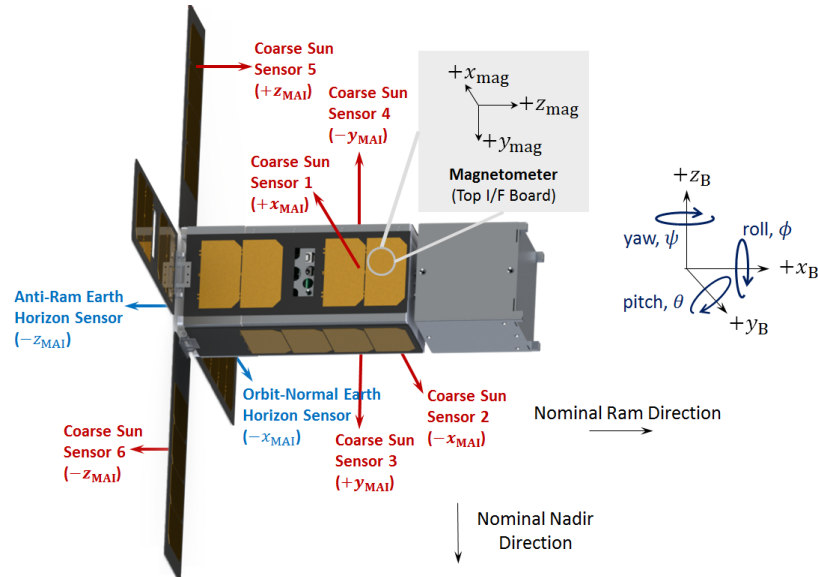


Figure 3.1 illustrates the locations of the attitude sensors selected for Micromas. They include six coarse Sun sensors in the form of simple photodiodes mounted on the outward faces of the solar panels, two thermopile static Earth sensors located within the reaction wheel assembly's chassis, and a triaxial flux-

³ Chobotov, *Spacecraft Attitude Dynamics and Control*, p. 69.

⁴ James Richard Wertz, Everett, and Puschell, *Space Mission Engineering*, p. 583.

gate magnetometer located on the top avionics interface board. Other sensors measure relative rotation rates and are shown in Figure 3.2. These sensors include three reaction wheel tachometers located in the reaction wheel set, a MEMS IMU situated next to the magnetometer, and an optical quadrature encoder for the scanner assembly.

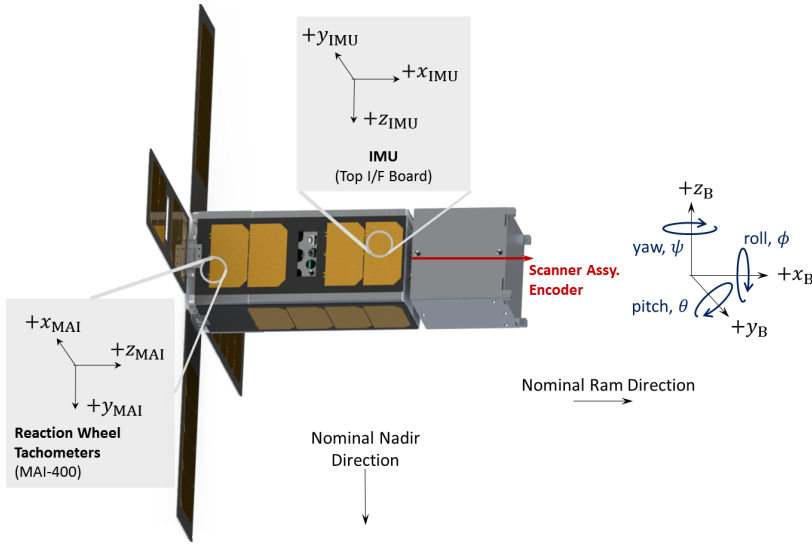


Figure 3.2: Relative Rotation Sensor Locations on Micromas

3.2.1 GPS and Why We Aren't Using It

A Global Positioning System (GPS) receiver offers precise ECEF position and velocity knowledge as well as a precise time signal. Unfortunately, it also requires a zenith-facing antenna, space in the avionics board stack, and electrical power. Given that frequent position updates (more than ~ 0.1 hertz) are unnecessary with orbit propagation, electrical power is not a particular issue since the receiver can be duty-cycled. The principal issue with the 3U cubesat form factor is limited space. Adding a GPS receiver board within Micromas would mean removing one of the other boards, all of which are necessary for the operation of the spacecraft, and none of which can be redesigned without significant effort expended to deal with issues due to electromagnetic interference (especially with magnetometer data and communications). The next, larger iteration of Micromas should feature a GPS receiver.

3.2.2 Sun Sensors

Sun sensors offer a measurement of the sun's position relative to the body's reference frame on the spacecraft. This measurement is compared against an on-board ephemeris to determine angular error. Some sun sensors can give a solar vector estimate with an error only on the order of an arcminute. Unfortunately,

these sensors are expensive, bulky, and only function during daylight. Since Micromas needs to be able to maintain tight pointing in eclipse, fine sun sensors make little sense to use. Additionally, sensors that can maintain tight pointing usually have a narrow field of view. Having sun sensors with a large field of view is useful for maneuvering the spacecraft when the object of the narrow sensor's field of view is outside of that sensor's field of view.

Coarse sun sensors usually consist of current sensors on solar panels or photodiodes. The MAI-400 reaction wheel assembly contains an analog to digital converter that can convert conditioned analog photodiode signals to a sun vector measurement. With simple sensors on six outward orthogonal faces of the spacecraft, a rough estimate of the sun's direction $\vec{R}_{\text{Sun}}^{\text{B}}$ can be obtained via Equation 3.1:

$$\vec{R}_{\text{Sun}_i}^{\text{B}} = k_{\text{SS}_i} \frac{V_{\text{SS}_i} + b_{\text{SS}_i}}{V_{\text{SS}_{\max}}} \quad \text{for } i = 1, 2, 3, \quad (3.1)$$

where k_{SS_i} is the gain for sensor pair i , V_{SS_i} is the voltage measured by sensor i , b_{SS_i} is the bias for sensor i , and $V_{\text{SS}_{\max}}$ is the maximum voltage measurable by the sensors. This is a 3-vector because even with a strong albedo affecting a nadir-facing sensor, the sensor on the opposite side will see the appreciably brighter sun. The dimmer measurement is simply thrown out. When the Earth's albedo and the sun vector are close to the same direction, then angular errors can result.

The analytical approximation of the solar ephemeris provided in the *Astronomical Almanac* results in a mean-equator of date vector between the Earth and the sun to an accuracy on the order of 0.01 degrees, which is an order of magnitude within our estimation requirements. This is the approximation used by the MAI-400 for determining the sun vector, so the PIC24 will not have to implement a solar ephemeris algorithm.

The sun vector as determined by the sun sensors is compared against the sun vector provided by the solar ephemeris approximation to provide a reference vector for determining the difference between the body reference frame and the inertial reference frame.

3.2.3 Magnetic Field Measurement

Like the sun sensors, a magnetometer takes an environmental measurement and compares it to an onboard model to determine the angle between the measured and predicted vector.

The MAI-400 was designed to use PNI's Micromag3 triaxial fluxgate magnetometer, which has a resolution of 32 nanoteslas per least significant bit. This magnetometer has flight heritage aboard the University of Michigan's Radio Aurora Explorer (RAX) spacecraft.⁵ The measurements from this magnetometer are compared against a sixth-order International Geomagnetic Reference Field 2011 (IGRF11) model of the Earth's magnetic field⁶ to determine the dif-

⁵ Springmann et al., "The Attitude Determination System of the RAX Satellite".

⁶ Finlay et al., "International Geomagnetic Reference Field".

ference between the body-fixed magnetic field vector (measured) and the inertial magnetic field vector (modelled). It currently uses 2005 epoch coefficients, though Figure 3.3 shows that the 2005 epoch model produces unacceptable angular error over the entirety of the orbit. Figure 3.3 also shows that the use of the

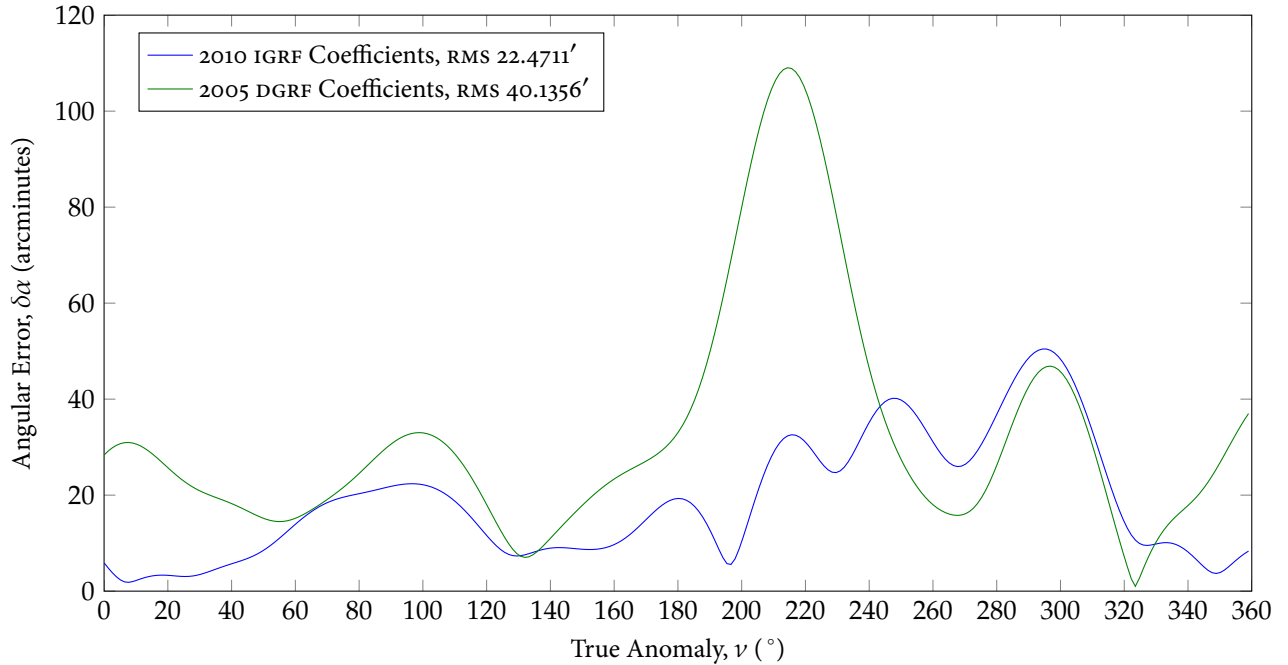


Figure 3.3: Angular Error of Sixth-Order/Degree IGRF Model vs. Thirteenth-Order/Degree IGRF Model. Note that the thirteenth-order model to which the two sixth-order models are compared uses 2010 coefficients.

2010 epoch sixth-order model (at least when compared to the thirteenth-order model, which is the highest available for the IGRF11) produces angular errors of almost a degree over the course of a single orbit. To meet the tight pointing requirements, it will be necessary to use a higher-order magnetic field model for yaw determination.

Problems may also emerge given that the spacecraft itself is a source of local magnetic fields. The reaction wheels consist of three brushless DC motors that generate small magnetic fields. MAI recommends mounting the magnetometer at least 5 inches away from the reaction wheels to avoid interference; however, such mounting will place the magnetometer directly next to the larger brushless DC motor necessary to spin the scanner assembly. It will be necessary to characterize the magnetic field generated by this motor and its variation over its rotation in order to remove the bias it introduces to the magnetometer measurements. Additionally, current flowing through the spacecraft's electronics may produce a small bias within the magnetic field measurements.



Figure 3.4: The Voyager Spacecraft. The magnetometer is located at the end of the long boom. Image Credit: <http://voyager.jpl.nasa.gov/spacecraft/>

⁷ Battin, "Some Funny Things Happened on the Way to the Moon"

⁸ "Spacecraft Earth Horizon Sensors".

⁹ Chen and J. R. Wertz, "Analysis of SMS-2 Attitude Sensor Behavior Including OABIAS Results"; Natanson and Glickman, "A Study of TRMM Static Earth Sensor Performance Using On-Orbit Sensor Data"; Phenneger et al., "Infrared Horizon Sensor Modeling for Attitude Determination and Control".

¹⁰ Bhanderi, "Spacecraft Attitude Determination with Earth Albedo Corrected Sun Sensor Measurements".

¹¹ Lerner, "Three-Axis Attitude Determination".

¹² Hashmall and Sedlak, "An Algorithm for Converting Static Earth Sensor Measurements into Earth Observation Vectors".

“ A good plan now is better than a perfect plan next week. ”

—GEN George S. Patton, Jr., USA

Ideally, we would mount additional magnetometers on the deployable solar panels, far from the magnetic disturbances of the motors and spacecraft circuitry, which we could then filter to obtain a more accurate estimation of the local geomagnetic field. Such a tactic was used on the Voyager series of deep space probes (see Figure 3.4). Unfortunately, both cost and schedule do not allow for the mounting of these magnetometers, so we will have to pay extra attention to the characterization of the scanner assembly's magnetic field and incorporating these data in the attitude estimator and controller.

3.2.4 Earth Limb Detection

“ A few weeks before the launch, the Navigator Command Module Pilot, Jim Lovell, spent a few hours practicing on the earth-horizon sextant simulator at M.I.T. What he consistently called the 'horizon' was actually about 20 miles above the real horizon. Great! Jim Lovell could be calibrated and his bias number loaded into the flight computer. ”

—Dick Battin⁷

Unfortunately, automated Earth limb sensors are not as easily calibrated as CAPT Lovell: horizon definition is less defined at lower altitudes because of the Earth's atmosphere. Optical sensors such as cameras or arrays of infrared sensors can take advantage of measuring the curvature of the Earth, rather than simply the amount of Earth in view. Unfortunately, optical sensors do not work during eclipse, and arrays of infrared sensors are bulky and expensive. The earliest limb sensors were spinning detectors that traced a swath of the Earth's surface and noted the angles where the sensor crossed the limb to view space.⁸ On-orbit data compared against other attitude sensors suggest that the noise floor of local weather phenomena at the limb affects the albedo to a point where without a very precise albedo model, the limb measurement cannot be more precise than c. 0.1 degrees.⁹ Such albedo models have seen an increase in fidelity in recent years, though they tend to take up a significant amount of processor time.¹⁰

MICROMAS uses two sets of thermopile type static Earth sensors to measure temperature, which corresponds to the amount of the limb that is in the field of view of the sensor. From these values can be determined the spacecraft's dip angles for pitch and roll (see their orientations in Figure 3.1). While MICROMAS uses the simple method described in Wertz's book¹¹ to combine dip angle measurements, more optimal methods exist, though they are computationally expensive.¹²

These sensors see the infrared radiation provided by the Earth's limb. Filters

can be added to limit them to the emission spectra of particular gasses in the atmosphere that have a more uniform distribution, such as carbon dioxide. Even with a filter, though, weather can still affect sensor measurements, so these static Earth sensors will be unable to achieve better than 0.1 degrees (20 arcminutes) accuracy with their measurements.

3.2.5 Inertial Measurement Unit

The continued miniaturization of electromechanical devices allows Micromas to carry its own rate gyro in the form of an Analog Devices ADIS16334 IMU. Gyros are subject to environmentally sensitive biases that result from changes in temperature and linear acceleration, as well as small variations in scale factor for each axis, and very small misalignments that could result in small coupling between axes in the measurements. The ADIS16334 offers a resolution of 0.0125 degrees per second per least significant bit, an in-run bias stability of 0.0072 degrees per second, and an angular random walk of 2 degrees per root hour. The reader can refer to Rogers's work¹³ and Lawrence's work¹⁴ on gyro models for more information.

The purpose of the gyro is not to measure attitude directly but rather to propagate the attitude estimate between attitude measurements. Because of this, even the somewhat large gyro drift rate present in the ADIS16334 (at least as compared to the precise instruments traditionally used for spacecraft) cannot unduly upset the attitude estimate of the spacecraft, since the estimate is corrected by the more precise attitude sensors.

3.2.6 Scanner Assembly Encoder

Because the scanner assembly's motor is a brushless DC motor, the motor controller needs to know the relative angular position of the rotor about its rotation to determine timing for the application of current to the motor. Additionally, the angular position information is provided to the payload for the purposes of geolocating its data. The ADCS needs the encoder for determining the speed of the scanner assembly's rotation for the purposes of counteracting the scanner assembly's angular momentum.

For Micromas, we have selected MicroE's Mercury 1500V optical quadrature encoder to measure a MicroE 301-00075 rotary encoder grating, providing an encoder resolution of 45 arcseconds per count. This is well within the rotation angle knowledge requirement of 6 minutes of arc.

3.3 COMPUTATIONAL RESOURCES AVAILABLE TO THE GNC SYSTEM

Micromas's primary flight computer, a PIC24F, has flight heritage on multiple cubesats (Caerus/Mayflower, DICE-1, and DICE-2). While the microcontroller has only hardware fixed-point, it does offer a software floating-point application

¹³ Rogers, *Applied Mathematics in Integrated Navigation Systems*.

¹⁴ Fallon, "Gyroscope Models".

programming interface (API), though the floating-point implementation is an order of magnitude slower than the fixed point. Current tests using the floating-point API running an extended Kalman filter with a six-by-six covariance matrix show that the ADCS should take no more than 15 percent of the microcontroller's clock time (chapter 4 has more information about filter selection).

Two options exist if during testing we discover that the current controller and estimator design are insufficient to meet requirements. The PIC24E, while having no flight heritage, is a pin-for-pin replacement for the PIC24F and is significantly faster. The team's preliminary radiation tests show that the PIC24E should hold up to the space environment. If the speed increase of the PIC24E is insufficient, contracting with Maryland Aerospace would allow the team to run ADCS code on the more powerful ARM processor within the reaction wheel assembly.

Spacecraft with finer pointing requirements should consider using hardware designed for performing vector and matrix operations quickly, such as digital signal processors (DSPs), or purpose-designing their own processing hardware on a field-programmable gate array (FPGA). The ExoplanetSat spacecraft has taken the latter approach.¹⁵

¹⁵ Pong et al., "High-Precision Pointing and Attitude Determination and Control on ExoplanetSat".

4

ESTIMATION AND CONTROL APPROACH

“ The advancement and perfection of mathematics are intimately connected with the prosperity of the State. ”

—Napoleon

PRIORITARILY, THE GNC SYSTEM of Micromas concerns itself with the estimation and control of the spacecraft’s attitude—however, several of the models used in attitude determination rely upon the spacecraft’s knowledge of its position, as well as the current time. Thus, the approach section will begin with a discussion of position estimation.

4.1 POSITION ESTIMATION

Position estimation would most easily be accomplished via an onboard GPS receiver, since a GPS receiver can provide position, velocity, and time information to an unparalleled degree of accuracy without carrying an atomic clock; however, as mentioned in Section 3.2.1, power and space limitations preclude including a GPS in the spacecraft. Micromas mitigates the lack of precision time measurement by carrying a temperature-compensated crystal oscillator as a time reference, being updated every communication pass as to the time offset between the spacecraft’s avionics elapsed time and Coordinated Universal Time. Still, given the tight pointing requirements, an analysis of the available position determination methods is necessary.

4.1.1 Propagation Methods

4.1.1.1 ANALYTICAL METHODS The primary analytical methods that concern Micromas are Kepler’s problem, and the Simplified General Perturbations, version 4 (SGP4). Typically solving Kepler’s problem requires numerical iteration; the MAI-400 simplifies the problem to a circular orbit, reducing Kepler’s prob-

lem to

$$v(t) = v_{\text{epoch}} + n(t - t_{\text{epoch}}) \quad (4.1)$$

The problem with this formulation is that no orbit is perfectly circular. The eccentricity will result in cyclical errors in true anomaly estimation.

The **SGP4** propagator is used for propagation of two-line element sets (**TLES**) by the North American Aerospace Defense Command (**NORAD**). It was developed from the 1950s through the 1980s as a method of propagating the orbits of all of the trackable objects in the sky with the era's limited computers.¹ With today's computers, however, numerical integration can perform a superior job of such mass propagation; nevertheless, **TLES** are still the common means for dissemination of orbit data (and, of course, **NORAD** is kind enough to provide these data to everyone with an internet connection).

According to the documentation, **SGP4** has an expected error of a kilometer at epoch. The propagator's relatively poor performance results from truncated analytical approximations of higher-order gravitational terms as well as an abbreviated atmospheric drag model (**NORAD** does not know the precise drag characteristics of all spacecraft in orbit, which are both spacecraft- and spacecraft-attitude-dependent). However, given that we know this information, since we built the spacecraft, we should be able to develop our own filter using the **TLE** data and incorporating our knowledge of the spacecraft's characteristics to obtain a more accurate position estimate.

4.1.1.2 NUMERICAL METHODS Two primary methods exist for numerically propagating an orbit: Cowell's formulation and Encke's method. Cowell's formulation is probably the most apparent method: simply sum the forces external to the satellite and integrate them numerically to find velocity and position. Encke's method looks at variations of forces about an osculating reference orbit. Because the method looks only at the small differences between the osculating orbit and the actual orbit, more numerical precision can be achieved for the same speed, or the simulation can run faster for the same precision. The osculating orbit must be periodically updated when the differences between the two become too large.

The **MAI-400** also has a Cowell's formulation numerical propagator that uses an **RK4** integrator with an integration step size of one second. This propagator models the gravitational force of the Earth as a point mass and includes the perturbation due to J_2 , the second zonal harmonic term of Earth's gravity. This model does not account for drag.

4.1.2 Practical Considerations

In the last year, a member of the M.I.T. Space Systems Laboratory, Brian Coffee, conducted a study in conjunction with the Aerospace Corporation involving both their GPS receiver-equipped **PSSCT-2** small spacecraft² as well as a number of cubesats active from the summer of 2011 to the summer of 2012. The **PSSCT-2** spacecraft has a very similar orbit to that expected for **Micromas** as well a similar

² Coffee, Cahoy, and Bishop, "Propagation of CubeSats in LEO Using NORAD Two Line Element Sets: Accuracy and Update Frequency".

mass and shape characteristics. The positional errors between PSSCT-2's GPS measurements and the SGP4-propagated TLEs were consistently on the order of a kilometer, with the largest error along-track, and negligible error radially. A survey of the cubesats noted that said cubesats saw at most 36 hours between TLE updates. Thus, Micromas can expect epoch knowledge of its position within about a kilometer and daily ephemeris updates.

4.2 ATTITUDE ESTIMATION

Micromas uses a discrete-discrete multiplicative extended Kalman filter with complementary feedback. This section will explain the reasoning behind such a selection and the theory behind it.

4.2.1 Review of Extended Kalman Filter

The continuous time nonlinear model for the system dynamics with additive noise is given by

$$\dot{x}(t) = f(x(t)) + g(w(t)) \quad (4.2)$$

where $x(t)$ is the state vector at time t , f represents the nonlinear system dynamics functional, g represents the noise dynamics functional, and $w(t) \sim \mathcal{N}(\mathbf{0}, \mathbf{W})$ represents the process noise. The measurement dynamics equation is a discrete process and is given as

$$y_k = h(x(t)) + v_k \quad (4.3)$$

where y_k is the measurement vector at timestep k , h represents the nonlinear measurement dynamics functional, and $v_k \sim \mathcal{N}(\mathbf{0}, \mathbf{R}_k)$ represents the measurement noise. These noises are uncorrelated, white, Gaussian noise processes.

The state vector for a discrete-time process at timestep k is represented by x_k .

$$x_{k+1} = \phi(x_k) + \gamma(w(t)) \quad (4.4)$$

where ϕ represents the discrete nonlinear system dynamics functional, γ represents the discrete noise dynamics functional, and $w_k \sim \mathcal{N}(\mathbf{0}, \mathbf{W}_k)$ represents the discrete process noise.

The *a priori* estimate of the state at timestep k (a mean of a Gaussian distribution) is given by $\hat{x}_{k|k-1}$ and the *a posteriori* by $\hat{x}_{k|k}$, where the $\hat{\cdot}$ denotes an estimated quantity or quantities. The *a priori* state estimate noise covariance at timestep k is given by $\mathbf{Q}_{k|k-1}$ and the *a posteriori* by $\mathbf{Q}_{k|k}$. Given that the Kalman filter is a linear model, the system dynamics must be linearized from timestep to timestep, using the *a posteriori* estimate from the previous iteration to form

the Jacobians of the system and measurement dynamics:

$$\Phi_k = \left. \frac{\partial f(x)}{\partial x} \right|_{x=\hat{x}_{k|k-1}} \quad (4.5)$$

$$\mathbf{H}_k = \left. \frac{\partial h(x)}{\partial x} \right|_{x=\hat{x}_{k|k-1}} \quad (4.6)$$

The discrete-time state propagation (prediction) equations use the discrete state dynamics:

$$\hat{x}_{k+1|k} = \Phi_k \hat{x}_{k|k} \quad (4.7)$$

$$\mathbf{Q}_{k+1|k} = \Phi_k \mathbf{Q}_{k|k} \Phi_k^T + \Gamma_k \mathbf{W}_k \Gamma_k^T \quad (4.8)$$

and the discrete-time update (filter) equations use the discrete measurement dynamics:

$$\mathbf{L}_k = \mathbf{Q}_{k|k-1} \mathbf{H}_k^T \left(\mathbf{H}_k \mathbf{Q}_{k|k-1} \mathbf{H}_k^T + \mathbf{R}_k \right)^{-1} \quad (4.9)$$

$$\hat{x}_{k|k} = \hat{x}_{k|k-1} + \mathbf{L}_k (\mathbf{y}_k - \mathbf{h}(\hat{x}_{k|k-1})) \quad (4.10)$$

$$\mathbf{Q}_{k|k} = (\mathbf{I} - \mathbf{L}_k \mathbf{H}_k) \mathbf{Q}_{k|k-1} \quad (4.11)$$

Since the covariance matrices \mathbf{Q} , \mathbf{W} , and \mathbf{R} must be symmetric and positive definite, the state estimate noise covariance matrix should be symmetrized after every step: $\mathbf{Q} = \frac{1}{2}(\mathbf{Q} + \mathbf{Q}^T)$. Though it adds operations, the Joseph formulation for covariance update can also give better numerical stability:

$$\mathbf{Q}_{k|k} = (\mathbf{I} - \mathbf{L}_k \mathbf{H}_k) \mathbf{Q}_{k|k-1} (\mathbf{I} - \mathbf{L}_k \mathbf{H}_k)^T + \mathbf{L}_k \mathbf{R}_k \mathbf{L}_k^T \quad (4.12)$$

4.2.2 Attitude Parameterizations

Markley gives a comprehensive overview of attitude parameterization methods in Chapter 12 of *Spacecraft Attitude Determination and Control*, so only a brief comparison of the methods will be given here. When propagating attitude information over time, the four-element quaternion is preferable to the nine-element direction cosine matrix (DCM) or the three Euler angles; the DCM requires more memory space and processor time for its nine elements, and the Euler angles require additional processor time for trigonometric operations. For both of these reasons, quaternions are the preferable means of storing and propagating attitude information in a computer.³ For further discourse on quaternions and their peculiar algebra, the reader should refer to Kuipers's work.⁴ Micromas uses a scalar-first quaternion formulation.

Kalman filtering with multiplicative quaternion estimation works slightly differently from typical Kalman filters—rather than using an “additive” innovation, which can quickly destroy the normalization of the attitude quaternion, we use a multiplicative error quaternion: $\delta q \equiv q^{-1} \otimes \hat{q}$, rather than $\delta q \equiv q - \hat{q}$ (\otimes represents the quaternion multiplication operation). Because the quaternion has four parameters with one constraint equation, but three degrees of freedom,

³ Markley and F. H. Bauer, “Attitude Error Representations for Kalman Filtering”, “Attitude Representations for Kalman Filtering”.

⁴ Kuipers, *Quaternions and Rotation Sequences*.

the covariance matrix of the quaternion has one eigenvalue that is zero. With the additive formulation, numerical issues can cause the zero eigenvalue to become negative, resulting in a non-positive definite state covariance matrix, causing the filter to diverge.⁵

The solution chosen for the MMS spacecraft in 1978 and many spacecraft since uses two parameterizations of the attitude state: one the full quaternion $q \in \mathbb{R}^4$ for state propagation and one a three-element error vector $\delta\alpha$ for update and covariance propagation. This error vector could take the form of a modified Rodrigues parameter, but for this spacecraft, we will follow the convention of MMS and use the changes in Euler angles. This approach is also being used on ExoplanetSat, an analogous cubesat with tight pointing requirements.⁶ The error quaternion is related to the error vector by

$$\delta q \approx \begin{bmatrix} 1 \\ \frac{\delta\alpha}{2} \end{bmatrix} \quad (4.13)$$

where the $\delta\alpha \in \mathbb{R}^3$ term corresponds to roll, pitch, and yaw errors in the inertial rotation from the estimated body frame to the actual body frame.

4.2.3 Propagation

Propagation of the state estimate and state estimate noise covariance between measurements about some nonlinear reference trajectory distinguishes the extended Kalman filter from the regular, linear Kalman filter. Typically propagation is accomplished via numerical integration of a model of the system's dynamics. ExoplanetSat propagates the state in this manner, propagating the spacecraft's attitude and angular rate. The downside of this approach is carrying around potentially cumbersome system dynamics equations, such as Equation 2.10. Such a model requires additional processor time to account for the environmental models that determine external torques.

A gyroscope allows for direct measurements of the attitude rate and mitigates the effect of modelling errors. The less-complex gyro dynamics become the system dynamics, and the gyro measurement noise becomes the process noise. This type of filtering is called *complementary filtering*, because one set of sensors is used to update another based on the strengths and weaknesses of each set of sensors.⁷

4.2.3.1 PROCESS MODEL A more general model of gyro drift than the one described in Chapter 3 is used for the Kalman filter. The gyro measurements ω_{meas} are treated as a first-order Markov process; that is, the sum of a white noise drift, random bias, and random walk drift):

$$\omega_{\text{meas}} = \omega + \beta + \eta_v \quad (4.14)$$

where $\omega \in \mathbb{R}^3$ are the components of the actual spacecraft angular velocity in the body frame; $\beta \in \mathbb{R}^3$ is the random-walk term, the drift-rate bias, with

⁵ Tweddle, "Computer Vision Based Navigation for Spacecraft Proximity Operations", pp. 210–12.

⁶ Pong et al., "High-Precision Pointing and Attitude Determination and Control on ExoplanetSat".

⁷ Brown and Hwang, *Introduction to Random Signals and Applied Kalman Filtering*, p. 313.

$\dot{\beta} = \eta \sim \mathcal{N}(\mathbf{0}_{3 \times 1}, \sigma_u^2 \mathbf{I}_{3 \times 3})$; and $\eta_v \sim \mathcal{N}(\mathbf{0}_{3 \times 1}, \sigma_v^2 \mathbf{I}_{3 \times 3})$ is the drift-rate noise. Several studies performed in the 1970s suggest this model is adequate for precision gyros, though they also caution that an exponentially-correlated noise model may be more appropriate for some types of gyros.⁸ Analog Devices, the gyro manufacturer, suggests that this model is appropriate for their MEMS gyros, so long as the on-chip temperature compensation is properly calibrated.⁹ Beyond the nominal temperature range, a thermal bias estimator may be necessary.¹⁰

⁸ Truncule, Koenigsberg, and Harris, "Spectral Density Measurements and Gyro Noise"; Farrenkopf, "Generalized Results for Precision Attitude Reference Systems Using Gyros".

⁹ Weinberg, "Calibrating iMEMS Gyroscopes".

¹⁰ Galante and Sanner, "A Non-linear Adaptive Filter for Gyro Thermal Bias Error Cancellation".

Because we are modelling the gyro measurements as a random walk process, we also have to carry around the gyro biases in the state. The estimated state is thus $m\hat{v}cx = [\hat{q}^T \hat{\beta}^T]^T$. The first-order quaternion kinematics are

$$\dot{q} = \frac{1}{2} \begin{bmatrix} 0 \\ \omega \end{bmatrix} \otimes q \quad (4.15)$$

For the angular velocity to be multiplied by a quaternion, it must be promoted to a *pure* quaternion, that is, a quaternion with a zero scalar term. The kinematics can be rewritten in matrix form as

$$\dot{q} = \frac{1}{2} \Omega(\omega) q \quad (4.16)$$

where

$$\Omega(\omega) = \begin{bmatrix} 0 & \omega^T \\ -\omega & -\omega^\times \end{bmatrix} \quad (4.17)$$

The $^\times$ symbol denotes the skew-symmetric, or cross product, matrix derived from the associated vector. This matrix takes the form

$$z = \begin{bmatrix} z_1 \\ z_2 \\ z_3 \end{bmatrix} \rightarrow z^\times \equiv \begin{bmatrix} 0 & -z_3 & z_2 \\ z_3 & 0 & -z_1 \\ -z_2 & z_1 & 0 \end{bmatrix} \quad (4.18)$$

4.2.3.2 DISCRETE PROPAGATION A numerical integrator determines the state estimate from timestep to timestep. ExoplanetSat uses an RK4 integrator to this purpose.¹¹ Crassidis and Junkins point out that this step can easily be adapted to discrete time dynamics. The linearized discrete-time system dynamics Φ_k are related to the linearized continuous-time dynamics by

$$\Phi_k = e^{F(t)\Delta t} \quad (4.19)$$

In the case of our quaternion kinematics, the linearized continuous-time kinematics are $F(t) = \Omega(\omega(t))$. While the matrix exponential is typically estimated via a truncated power series of the form $e^A = \sum_{n=0}^{\infty} \frac{1}{n!} A^n$, Markley notes that we can take advantage of the skew symmetry of Ω to find an exact solution:¹²

$$\begin{aligned} e^{\frac{1}{2}\Omega\Delta t} &= \sum_{j=0}^{\infty} \frac{\left(\frac{1}{2}\Omega\Delta t\right)^j}{j!} \\ &= \sum_{k=0}^{\infty} \left[\frac{\left(\frac{1}{2}\Omega\Delta t\right)^{2k}}{(2k)!} + \frac{\left(\frac{1}{2}\Omega\Delta t\right)^{2k+1}}{(2k+1)!} \right] \end{aligned} \quad (4.20)$$

¹¹ Pong et al., "High-Precision Pointing and Attitude Determination and Control on ExoplanetSat".

¹² Markley, "Matrix and Vector Algebra", p. 755.

Since with the symmetry we have

$$\Omega^{2k} = (-1)^k \|\omega\|^{2k} \mathbf{I}_{4 \times 4} \quad (4.21a)$$

$$\Omega^{2k+1} = (-1)^k \|\omega\|^{2k} \Omega \quad (4.21b)$$

We can substitute these identities (Equations 4.21) into Equation 4.20 to get

$$e^{\frac{1}{2}\Omega \Delta t} = \mathbf{I}_{4 \times 4} \sum_{k=0}^{\infty} \frac{(-1)^{2k} \left(\frac{1}{2}\|\omega\|\Delta t\right)^{2k}}{(2k)!} + \frac{\Omega}{\|\omega\|} \sum_{k=0}^{\infty} \frac{(-1)^k \left(\frac{1}{2}\|\omega\|\Delta t\right)^{2k+1}}{(2k+1)!} \quad (4.22)$$

If we notice that the first series of Equation 4.22 is the sine series and the second is the cosine series, we can rewrite Equation 4.22 as our discrete quaternion state transition matrix $\Omega_k(\omega_k, \Delta t)$,

$$\begin{aligned} e^{\frac{1}{2}\Omega \Delta t} &= \mathbf{I}_{4 \times 4} \cos \frac{1}{2}\|\omega\|\Delta t + \frac{\Omega}{\|\omega\|} \sin \frac{1}{2}\|\omega\|\Delta t \\ \Omega_k(\omega, \Delta t) &= \end{aligned} \quad (4.23)$$

giving us

$$\hat{q}_{k+1|k} = \Omega_k(\hat{\omega}, \Delta t) \hat{q}_{k|k} \quad (4.24)$$

Since we are not estimating gyro bias rate, we cannot propagate our estimated gyro bias states, so they remain constant from timestep to timestep until the next update step occurs. Our state estimate noise covariance monitors the error-state $\delta\alpha$ rather than the quaternion and thus requires an error-state transition matrix Φ_k , different from the state transition matrix described above:

$$\mathbf{Q}_{k+1|k} = \Phi_k \mathbf{Q}_{k|k} \Phi_k^T + \Gamma_k \mathbf{W}_k \Gamma_k^T \quad (4.25)$$

where $\Gamma_k = \begin{bmatrix} -\mathbf{I}_{3 \times 3} & \mathbf{0}_{3 \times 3} \\ \mathbf{0}_{3 \times 3} & -\mathbf{I}_{3 \times 3} \end{bmatrix}$ and discretizing our process noise covariance $\mathbf{W}(t)$ yields¹³

$$\mathbf{W}_k = \begin{bmatrix} \left(\sigma_v^2 \Delta t + \frac{1}{3} \sigma_u^2 \Delta t^3\right) \mathbf{I}_{3 \times 3} & \left(\frac{1}{2} \sigma_u^2 \Delta t^2\right) \mathbf{I}_{3 \times 3} \\ \left(\frac{1}{2} \sigma_u^2 \Delta t^2\right) \mathbf{I}_{3 \times 3} & \left(\sigma_u^2 \Delta t\right) \mathbf{I}_{3 \times 3} \end{bmatrix} \quad (4.26)$$

Because the gyros do not give us information on the gyro bias states, the error-state transition matrix is somewhat sparse. Like the quaternion state transition matrix, the error-state transition matrix can also be derived using a power series and cross-product matrix symmetries.¹⁴

$$\Phi_k = \begin{bmatrix} \Phi_{k11} & \Phi_{k12} \\ \mathbf{0}_{3 \times 3} & \mathbf{I}_{3 \times 3} \end{bmatrix} \quad (4.27a)$$

where

$$\Phi_{k11} = \mathbf{I}_{3 \times 3} - \frac{\hat{\omega}_k^\times}{\|\hat{\omega}_k\|} \sin \|\hat{\omega}_k\|\Delta t + \frac{(\hat{\omega}_k^\times)^2}{\|\hat{\omega}_k\|^2} (1 - \cos \|\hat{\omega}_k\|\Delta t) \quad (4.27b)$$

$$\Phi_{k12} = -\Delta t \mathbf{I}_{3 \times 3} - \frac{\hat{\omega}_k^\times}{\|\hat{\omega}_k\|} (1 - \cos \|\hat{\omega}_k\|\Delta t) + \frac{(\hat{\omega}_k^\times)^2}{\|\hat{\omega}_k\|^3} (\|\hat{\omega}_k\|\Delta t - \sin \|\hat{\omega}_k\|\Delta t) \quad (4.27c)$$

¹³ Crassidis and Junkins note that this approximation ignores the coupling effects of the cross-product term in the system dynamics, but that the approximation is valid with a sampling rate below Nyquist's limit. For a sample rate of 0.25 seconds and a safety of 10, the angular rate cannot exceed $\|\hat{\omega}\| < \frac{\pi/10}{0.25 \text{ s}} = 72^\circ/\text{s}$, well in excess of the actuators' capabilities. Crassidis and Junkins, *Optimal Estimation of Dynamic Systems*, pp. 166, 460.

¹⁴ Crassidis and Junkins, *Optimal Estimation of Dynamic Systems*, p. 459.

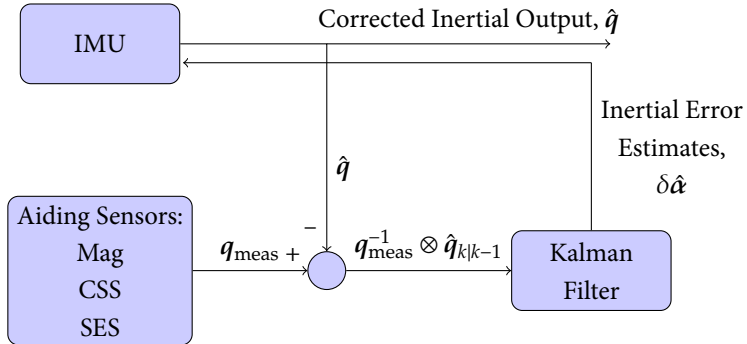
Since the gyro noise variances should remain constant, if we can ensure a constant sampling time Δt , we can calculate \mathbf{W}_k for all k . However, timing jitter due to higher-priority tasks in the real-time operating system may result in inconsistent gyro sampling, so this matrix will likely need to be calculated online along with Ω_k and Φ_k .

4.2.4 Update

The advantage of the complementary filter is that the time-varying reference trajectory (usually propagated from a model) is measured directly from the gyros. Because of this, the filter operates only on the system *errors*, rather than the system itself.¹⁵ For the attitude quaternion, this system error is reduced to the three terms for small angles between timesteps, $\delta\alpha$.

¹⁵ Brown and Hwang, *Introduction to Random Signals and Applied Kalman Filtering*, p. 394.

Figure 4.1: General Estimation Architecture: Complementary Feedback



4.2.4.1 MEASUREMENT MODEL An ideal filter of this sort would calculate the predicted nadir vector and magnetic field vector for the measurement sensitivity matrix \mathbf{H}_k ; however, these data are already combined in the MAI-400 via the TRIAD method before they arrive at the extended Kalman filter. While the TRIAD method is suboptimal, the method remains viable because of the difference in accuracy between data from the Earth horizon sensor (accurate on the order of 0.1 degrees), and magnetometer (accurate on the order of 0.5 degrees because of the truncated magnetic field model). There do exist more optimal methods for combining data from sensors with closer accuracy and noise characteristics (such as from a star sensor).¹⁶

Typically the measurement sensitivity matrix is the Jacobian of the measurements with respect to the states, or $\mathbf{H}_k = \frac{\partial \mathbf{y}_k}{\partial \mathbf{x}_k}$. Because the measurements the Kalman filter sees are already in the form used for update and propagation, the measurement sensitivity matrix is simply

$$\begin{aligned}\mathbf{H}_k &= \left[\begin{array}{cc} \frac{\partial \alpha_{\text{meas}}}{\partial \alpha} & \frac{\partial \alpha_{\text{meas}}}{\partial \beta} \end{array} \right] \\ &= \left[\begin{array}{cc} \mathbf{I}_{3 \times 3} & \mathbf{0}_{3 \times 3} \end{array} \right]\end{aligned}\quad (4.28)$$

This sensitivity matrix is a linearization of the measurement error about the current estimated state.

¹⁶ Markley and Mortari, “How to Estimate Attitude from Vector Observations”.

This type of filtering is called *decentralized filtering*.¹⁷ While we can determine the filter's effective measurement noise covariance matrix with our knowledge of the sensor noises and the TRIAD process (i.e., the TRIAD's estimation noise covariance matrix),¹⁸ it may be more effective to determine this quantity experimentally, given that the sensor noise is likely colored, and the transformation is nonlinear.

4.2.4.2 INNOVATION, FILTER GAIN, AND ERROR-STATE ESTIMATE The measurement innovation is calculated from the vector part of the quaternion multiplication of the measured attitude and the propagated state:

$$\begin{bmatrix} \tilde{y}_k \\ \frac{y_k}{2} \end{bmatrix} = q_{\text{meas}}^{-1} \otimes \hat{q}_{k|k-1} \quad (4.29)$$

The Kalman filter gain is simply calculated from Equation 4.9. With the innovation updating the error-state rather than the attitude quaternion, the update equation must be adapted from Equation 4.10, because the error-state estimate is discarded every timestep and the innovation is multiplicative, as shown in Equation 4.29. This alteration results in the following:

$$\begin{bmatrix} \delta\hat{\alpha} \\ \delta\hat{\beta} \end{bmatrix} = L_k y_k \quad (4.30)$$

Updating the state estimate noise covariance simply uses Equation 4.11.

To reconstruct the estimated error quaternion from the set of estimated error Euler angles $\delta\hat{\alpha}$, we use

$$\delta\hat{q} = \begin{bmatrix} \sqrt{1 - \frac{\delta\hat{\alpha}^T \delta\hat{\alpha}}{4}} \\ \frac{\delta\hat{\alpha}}{2} \end{bmatrix} \quad (4.31)$$

and thence we can update the attitude quaternion estimate:

$$\hat{q}_{k|k} = \hat{q}_{k|k-1} \otimes \delta\hat{q}^{-1} \quad (4.32)$$

Updating the gyro bias estimate is similarly straightforward:

$$\hat{\beta}_{k|k} = \hat{\beta}_{k|k-1} + \delta\hat{\beta} \quad (4.33)$$

The updated bias can be used in the next propagation steps to determine the estimated angular velocity from the rate gyro:

$$\hat{\omega}_{k|k} = \omega_{\text{meas}} - \hat{\beta}_{k|k} \quad (4.34)$$

4.2.5 Square Root and Factored Forms

As noted in Chapter 3, Micromas does not have the advantage of a floating-point unit. There are several adaptations of Kalman filters¹⁹ that require additional operations but evidence superior numerical stability, even with the truncation

¹⁷ Brown and Hwang, *Introduction to Random Signals and Applied Kalman Filtering*, p. 391.

¹⁸ This derivation is given in Tangyin and Shuster, "The Many TRIAD Algorithms"; and Markley, "Attitude Determination Using Vector Observations".

¹⁹ A recent NASA paper compares the performance of many of these implementations along with other filters: Kimber and Welch, "Comparison of Nonlinear Filtering Techniques for Lunar Surface Roving Navigation"; For a more comprehensive summary, c.f. Grewal and A. P. Andrews, *Kalman Filtering: Theory and Practice using MATLAB*.

errors inherent with fixed-point arithmetic. The advantage of using such a filter would be using the significantly-faster fixed-point arithmetic than the software floating-point arithmetic available to Micromas's PIC24.

The first such type of filter is called a square-root filter because it uses the Cholesky square root of the state covariance for propagation. J. E. Potter developed this filter for the MIT Instrumentation Lab for the Apollo mission, which was limited to a 15-bit fixed-point computer.²⁰ Later developments, called U-D factored forms or UDU^T filters offer the same significant numerical advantages as the square-root form with fewer operations by operating on the upper-triangular and diagonal factors of the state covariance.²¹

Unfortunately, these filter forms require a much greater investment of time for filter design to minimize the issues with saturation and quantization inherent in fixed-point math. Recent work designing a filter that decomposes the state covariance matrix into standard deviations and correlation coefficients, called the $\sigma-\rho$ filter, has resulted a straightforward framework for choosing scaling normalization terms to deal with saturation issues.²²

Should subsequent testing show that the current extended Kalman filter is too computationally burdensome, the $\sigma-\rho$ filter may offer a solution.

4.3 ATTITUDE CONTROL

Control design for spacecraft has seen significant advancement in the past two decades. In the 1980s, the cutting edge in maneuver design involved solving nonlinear two-point boundary value problems in seven, ten, or thirteen states to obtain an optimal reaction wheel torque and speed policy to slew about the eigenaxis between the current and desired attitude.²³ In 1993, Bilimoria and Wie showed that, counterintuitively, the eigenaxis slew is *not* the optimal slew in time or actuator usage.²⁴ Recent work has advanced on this notion to determine the optimal slew.²⁵ While such methods are intriguing, they completely monopolize the PIC24's processor time and would reduce the control cycle to a fraction of a hertz.

Micromas is structurally rigid and does not need to slew rapidly. Without a worry of upsetting structural resonances or meeting slew time constraints, high-jerk maneuvers are acceptable, and with the straightforward nature of (admittedly non-optimal) eigenaxis slew maneuvers, the control law can be extremely simple. Micromas thus borrows the nonlinear proportional-derivative control law employed by Christopher Pong for the reaction wheel controller on ExoplanetSat:²⁶

$$\tau_{RW} = \hat{\omega} \times (\mathbf{J}\hat{\omega} + \mathbf{H}_{RW} + \mathbf{H}_{PL}) - \tau_{dist} - \mathbf{K}_p \alpha_{err} - \mathbf{K}_d \omega_{err} \quad (4.35)$$

The first two terms constitute the feedback linearization, negating the nonlinearities of the system. Currently, for τ_{dist} , the controller only calculates the magnetic disturbance torques from the torque rods because the environmental torques are so small, especially in proportion to the 4-hertz control cycle. \mathbf{K}_p

²⁰ Potter and Stern, "Statistical Filtering of Space Navigation Measurements".

²¹ Bierman, *Factorization Methods for Discrete Sequential Estimation*.

²² Grewal and Kain, "Kalman Filter Implementation With Improved Numerical Properties".

²³ Junkins and Turner, *Optimal Spacecraft Rotational Maneuvers*, pp. 267–307.

²⁴ Bilimoria and Wie, "Time-Optimal Three-Axis Reorientation of a Rigid Spacecraft".

²⁵ Fleming, Sekhavat, and Ross, "Minimum-Time Reorientation of a Rigid Body".

²⁶ Pong et al., "High-Precision Pointing and Attitude Determination and Control on ExoplanetSat", p. 12.

and \mathbf{K}_d are the proportional and derivative controller gains, respectively; α_{err} is twice the vector part of the quaternion error²⁷, or $\left[\sim \frac{\alpha_{\text{err}}^T}{2} \right]^T = \hat{\mathbf{q}}^{-1} \otimes \mathbf{q}_{\text{cmd}}$; and $\boldsymbol{\omega}_{\text{err}} = \hat{\boldsymbol{\omega}} - \boldsymbol{\omega}_{\text{cmd}}$ is the angular velocity error.

As pointed out by Wie,²⁸ the closed-loop system dynamics can be simplified to second-order if the rotation angle is less than 90 degrees. The controller gains are scaled by the spacecraft's inertia tensor \mathbf{J} and parameterized by desired closed-loop natural frequency, ω_n , and damping ratio, ζ :

$$\mathbf{K}_p = \omega_n^2 \mathbf{J} \quad (4.36)$$

$$\mathbf{K}_d = 2\zeta\omega_n \mathbf{J} \quad (4.37)$$

We can then use simple pole-placement techniques to determine the closed-loop response of the system. Like ExoplanetSat, we will the closed-loop bandwidth to a conservative 0.04 hertz (100 times slower than the 4-hertz command rate) with closed-loop damping of $\zeta = 1/\sqrt{2} \approx 0.707$.

For the nominal nadir-pointing mode, the commanded attitude and rate values are set to the inertial to LVLH attitude quaternion $\mathbf{q}^{O/I}$ as determined by the guidance algorithm and the nominal orbital rate n :

$$\mathbf{q}_{\text{cmd}} = \mathbf{q}^{O/I} \otimes \begin{bmatrix} 1 \\ 0 \\ 0 \\ 0 \end{bmatrix} \quad (4.38)$$

$$\boldsymbol{\omega}_{\text{cmd}} = \begin{bmatrix} 0 \\ -n \\ 0 \end{bmatrix} \quad (4.39)$$

where n is the orbital mean motion from Equation 2.13.

For the slew mode, these values are set to limit the maximum angular velocity experienced by the spacecraft. If structural vibration testing determines later on that a structural resonance mode can occur at a low enough frequency, this value can be altered along with the derivative gain to avoid exciting the mode.

²⁷ For small attitude errors, such as would be seen during the LVLH stabilization mode, this α_{err} is the same thing as the Euler angular error from the commanded attitude.

²⁸ Wie, Weiss, and Arapostathis, "Quaternion Feedback Regulator for Spacecraft Eigenaxis Rotations".

5

SIMULATION

COMPUTER SIMULATION OFFERS a method of verifying the performance of the controllers and estimators using much higher fidelity models of the space environment than are used in the estimators and controllers themselves. This simulation will be validated by air-bearing testing. While the air-bearing and attendant environmental emulation equipment (e.g., spherical air bearing, three-degree-of-freedom Helmholtz cage, sun simulator, Earth limb simulator) cannot precisely replicate the dynamics of the space environment, they can provide validation for those parts of the simulation that do.

5.1 DESIGN

5.1.1 Dynamics

Computer simulation allows for performing parameter sweeps for varying parameter perturbations, such as inertia tensor variations from the model used in the estimator and controller, misalignments of sensor and actuator alignment from orthogonal with the spacecraft's principal axes of inertia. The dynamics of our truth model thus do not make the same assumptions as those for the estimator and controller design.

The orbital integrator currently uses Cowell's formulation for determining the spacecraft ephemeris and its rotational analogue for determining the spacecraft's rotational trajectory; future implementations may switch to Encke's method for ephemeris propagation because of the method's improved speed and numerical accuracy.¹ The integrator itself uses the fourth-order Runge-Kutta method with a fixed timestep of 0.05 seconds. This integrator was chosen because of its stability, small truncation error, and the ease of altering the step size. The simulation is implemented in MATLAB Simulink, which offers the advantage of a visual interface similar to that of an analog computer.

The goal of the simulation is not to replicate the position of the spacecraft to some set number of meters or its attitude to some set number of arcseconds; rather it is to test the controller and estimator using models that can provide for

¹ Bate, Mueller, and White, *Fundamentals of Astrodynamics*, p. 390; Vallado and McClain, *Fundamentals of Astrodynamics and Applications*, p. 522.

a realistic robustness analysis without taking overlong to run.

5.1.2 Models Used

5.1.2.1 GRAVITY The primary force affecting the spacecraft is the gravitational force of the Earth. Being in LEO, the effects of oblateness will be more pronounced than in further orbits;² thus the simulation's model of the Earth's gravitational force uses the EGM2008 gravity field model of degree 120.

To speed calculation, the gravity gradient torque calculation treats the Earth as a point mass; since the spacecraft is so short, changes in the gravitational potential gradient over the length of the spacecraft are negligible. If the spacecraft had long appendages, such as antennas or a gravity gradient boom, including the J_2 term in the torque calculation might have been appropriate.³

5.1.2.2 ATMOSPHERE The primary torque affecting the spacecraft is atmospheric drag. The atmospheric density model used is the U.S. Standard Atmosphere 1976. For small angles off the nominal orientation, self-shadowing of the outer surfaces of the spacecraft is negligible, though future development of the simulation may use ray tracing to take account for self-shadowing.

5.1.2.3 MAGNETOSPHERE The simulation uses a 13th-order magnetospheric model; such a high-order model is necessary to compare against the model aboard the spacecraft—Figure 3.3 shows the divergence of the spacecraft's magnetospheric model from the high-order model.

5.1.2.4 PLANETARY EPHEMERIDES The sun vector is returned by the same analytical model described in chapter 2.

5.1.2.5 SENSOR MODELS All of the sensor models account for saturation and quantization effects as well as output noise commensurate with their specification sheets. Additional details are noted below:

- Magnetometer

The magnetometer experiences a small bias field due to the proximity of the scanner assembly motor. Because this field has not been fully characterized, the model uses a static value for the bias.

- Static Earth Sensor

Ideally, the limb itself with albedo variation as well as the thermopile and mask topology would be modelled to determine the simulated nadir vector measurement;⁴ however, Maryland Aerospace has not cemented their sensor design yet. Thus, data from this sensor is modelled as a nadir vector perturbed around a random error cone with Gaussian noise with variance worse than that expected by the designed sensors.

- Gyroscope

Since the gyro is temperature-compensated and the sample rate is so low,

² Vallado and McClain, *Fundamentals of Astrodynamics and Applications*, p. 549.

³ Gottlieb, “Fast gravity, Gravity Partials, Normalized Gravity, Gravity Gradient Torque and Magnetic Field”.

⁴ Phenneger et al., “Infrared Horizon Sensor Modeling for Attitude Determination and Control”; Keat et al., “Earth Horizon Modeling and Application to Static Earth Sensors on TRMM Spacecraft”.

both temperature effects and high-frequency rolloff are ignored in the gyro model.

5.1.2.6 ACTUATOR MODELS The actuator models likewise account for saturation and quantization effects. The reaction wheels experience a deadband from -50 to 50 RPM.

5.2 RESULTS

5.2.1 Detumbling

The detumbling simulation was run assuming a worst-case tipoff rate of 20 degrees per second. Figure 5.1 shows that the B-dot controller was able to detumble the spacecraft in approximately 100 minutes. Using magnetorquers alone, the controller was able to achieve rates of less than 1 degree per second.

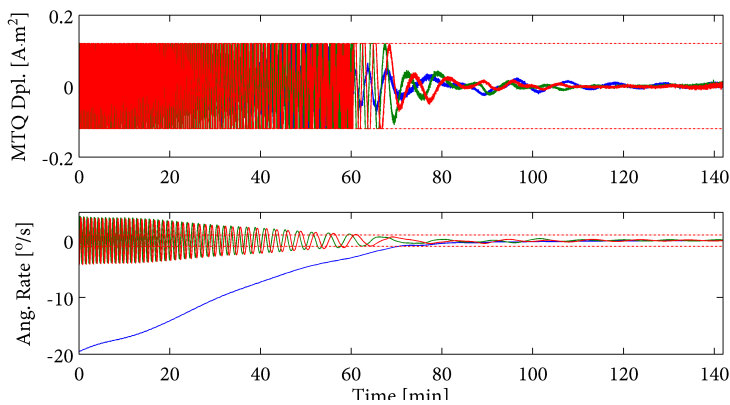


Figure 5.1: Detumbling Control History and Angular Rate Trajectory with an Initial Tipoff of 20 Degrees per Second

5.2.2 Slew

The slew mode simulation slews the spacecraft from an arbitrary pointing attitude to align the spacecraft with the LVLH frame. Figure 5.2 shows that this slew is achieved in approximately three minutes. The control law ensures a smooth spinup, coast, and spin-down eigenaxis slew profile. The low angular rates illustrated in the lower plot are achieved by saturating the angular error in the PD attitude controller; without this saturation, the spacecraft would slew as fast as possible to reach the desired attitude.

Figure 5.3 shows the control history for the slew mode. The spin-up and spin-down torques are clearly marked, almost looking like a bang-off-bang controller. The small magnetic dipoles are working to continually dump reaction wheel momentum.

Figure 5.4 illustrates that as the spacecraft approaches its nominal alignment, the gravity gradient and aerodynamic drag torques approach zero—this is be-

Figure 5.2: Slew Mode Angle and Rate Trajectory

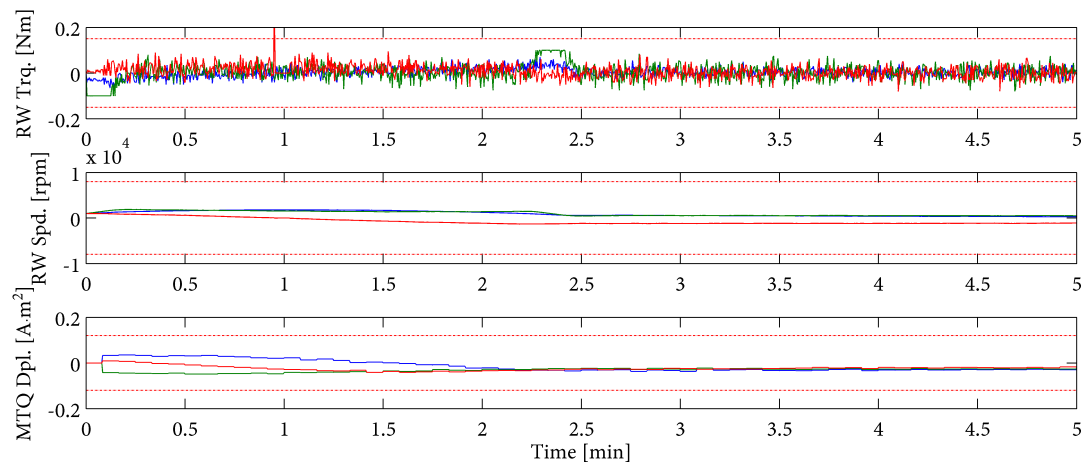
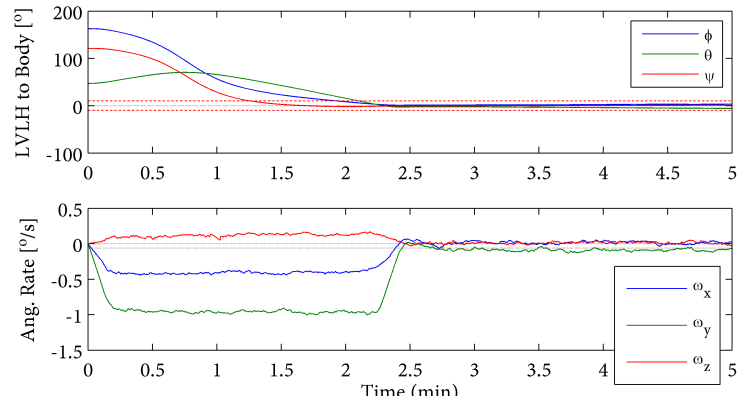


Figure 5.3: Slew Mode Control History

cause the spacecraft is at an unstable equilibrium point for those torques when aligned with the LVLH frame.

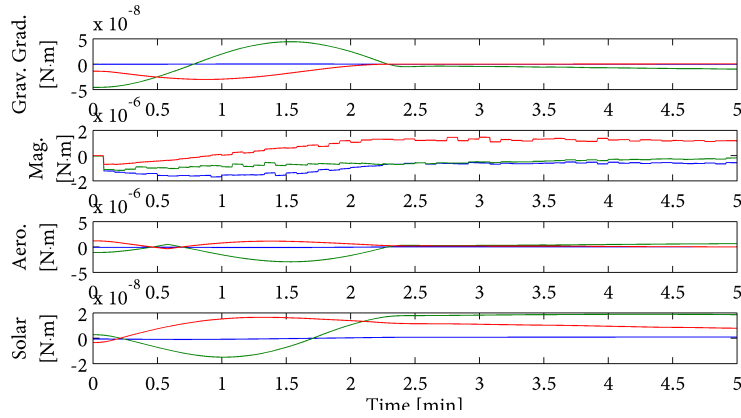


Figure 5.4: Slew Mode Disturbance Torques

5.2.3 Stabilization

The stabilization mode simulation assumes that the spacecraft has acquired the Earth's limb in its static Earth sensors' field of view and that the payload is spinning at its nominal rotational velocity of 0.83 hertz. This simulation lasts for a complete orbit. Figure 5.5 shows the trajectories for angle and rate over the course of the orbit.

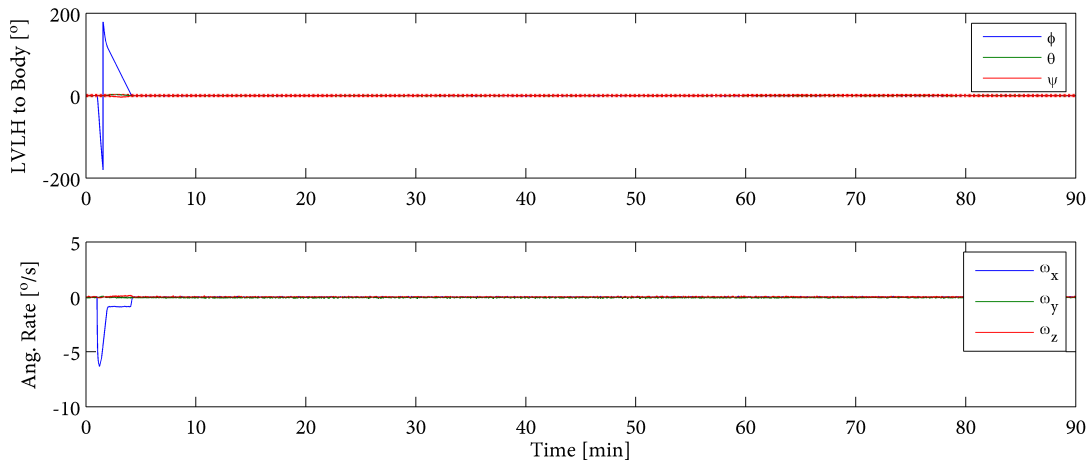


Figure 5.5: Stabilization Mode Angle and Rate Trajectory

While not a separate control mode, the payload spinup operation does offer enough challenges to warrant further scrutiny. Initial analysis shows that the torque transient resultant from overcoming the initial static friction of the bearing exceeds the torque available to the reaction wheels—this results in a large

transient at the beginning of the stabilization mode, shown in Figure 5.5. The constant negative rate about the *y-axis* is to rotate the spacecraft once per orbit and to maintain nadir pointing.

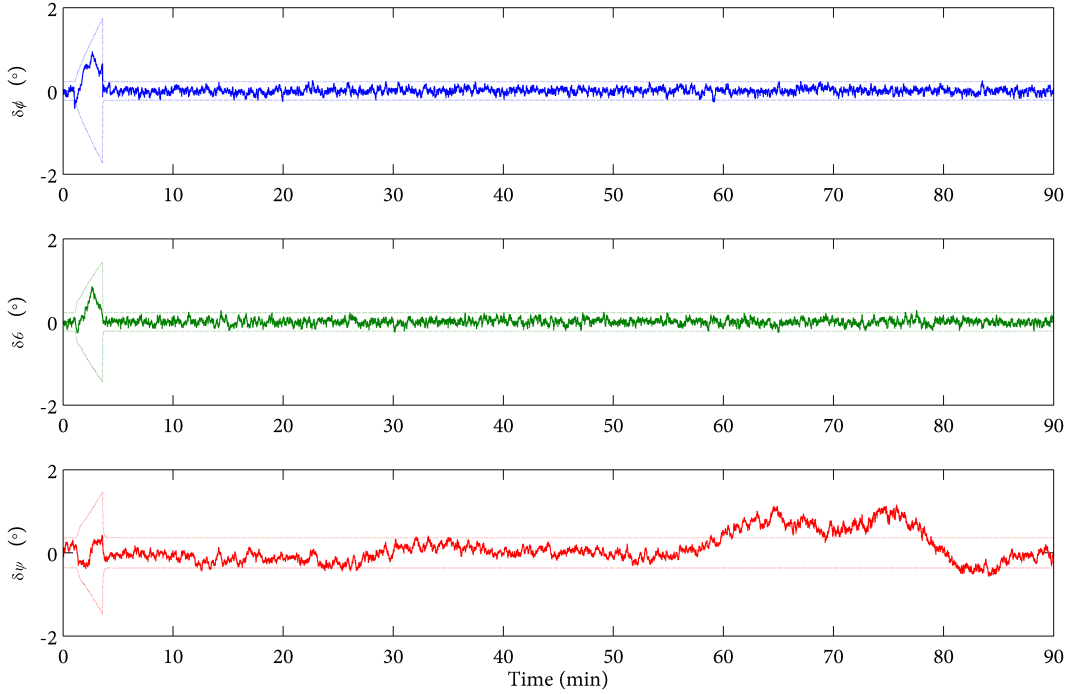


Figure 5.6: Stabilization Mode Angular Error

Figure 5.6 shows the angular errors for all three axes over the course of the orbit. The roll error (ϕ) and pitch error (θ) are both 6 arcminutes RMS; this is due to the accurate Earth horizon sensor. The yaw error (ψ), however is 23 arcminutes RMS—this larger error is due to the error in the magnetic field model. Note the deviation in pointing for the *yaw axis* between the 50 and 70 minute mark—these fluctuations correspond directly with the spikes on Figure 3.3 showing the difference between the sixth-order and thirteenth-order magnetic field models.

Figure 5.7 shows the control history for the stabilization mode throughout the spacecraft's orbit. Note in the reaction wheel speed plot that the spacecraft's *x wheel* is biased at approximately two-thirds of its maximum speed; this is because the *x* wheel is countering the angular momentum of the rotating scanner assembly.

Finally, Figure 5.8 shows estimated bias error for the stabilization mode throughout the spacecraft's orbit. Note the consistent estimate; once the bias has converged, LVLH stabilization does not see particularly nonlinear dynamics to dis-

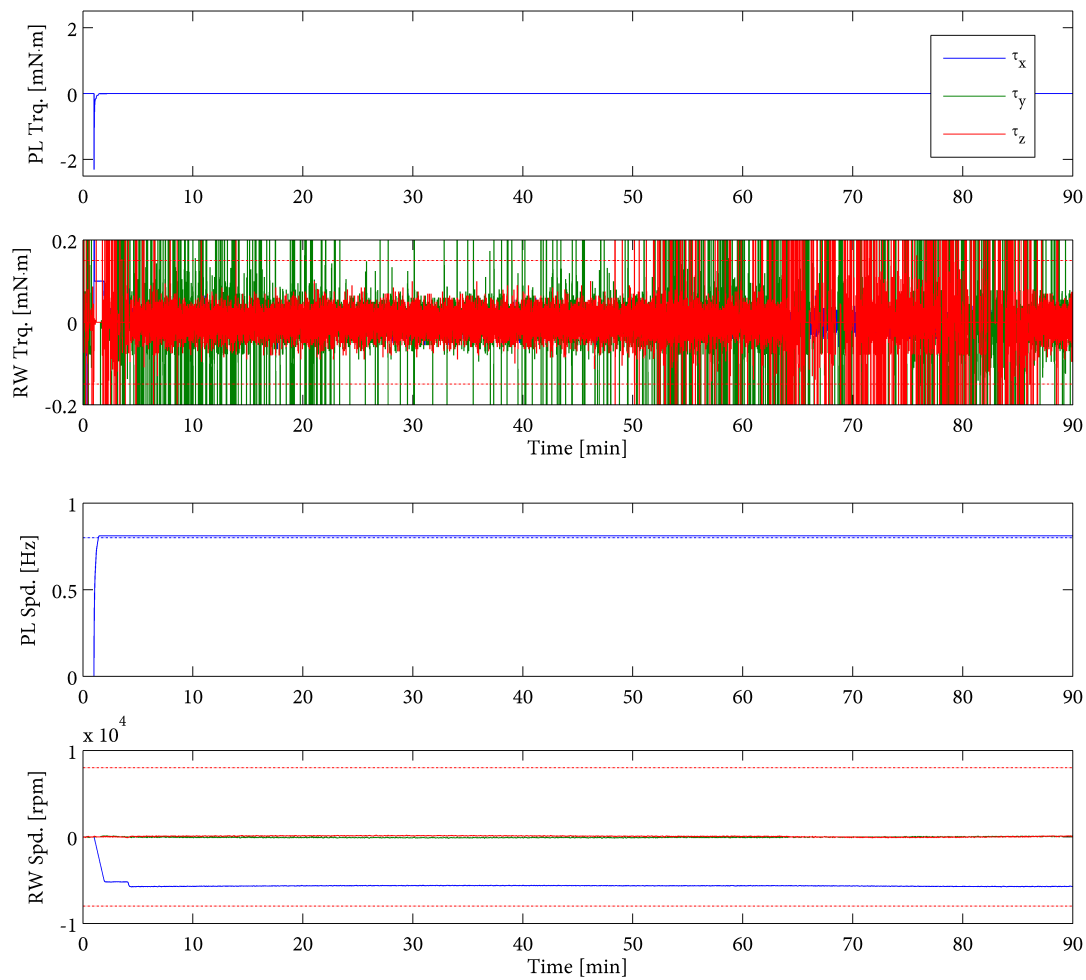


Figure 5.7: Stabilization Mode Control History

rupt the estimation.

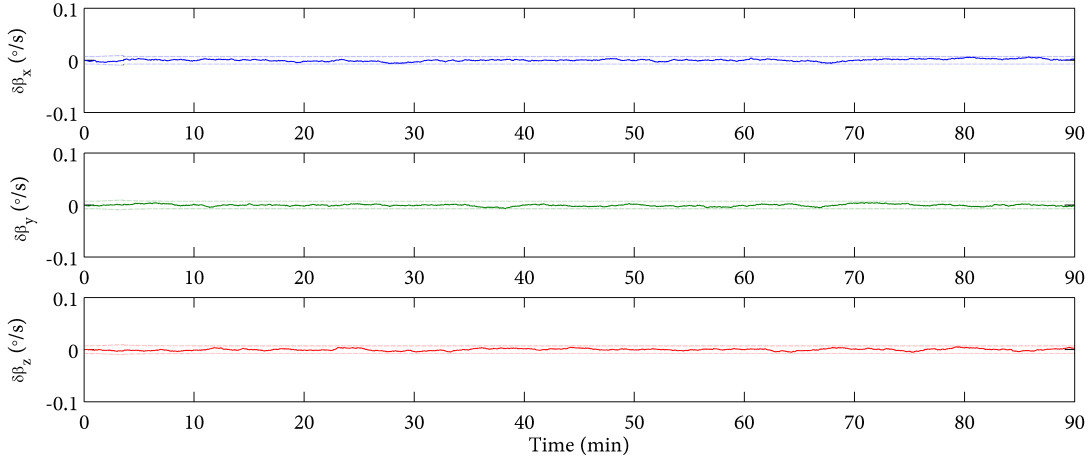


Figure 5.8: Stabilization Mode Bias Error Estimate

5.3 SENSITIVITY ANALYSIS

In perturbing the alignments of our sensors and actuators, we can analyze the estimator and controller robustness of the system by examining changes in actuator usage and estimation error. The sensor locations are shown in Figures 3.1 and 3.2

5.3.1 Scanner Assembly Rotor Bearing Axis Misalignment

In chapter 2 we examined the open-loop wobble effects of a misaligned payload rotor bearing axis. This section examines the closed-loop, controlled effect of such a misalignment. Figure 5.9 shows the errors in pointing due to misalignments from 0 to 5 degrees about the spacecraft's pitch axis. The figure shows that pointing error is not appreciably affected, a testament to the controller robustness. However, the reaction wheels must counter the wobble induced by the misalignment, and thus see increased RMS speeds, as shown in Figure 5.10.

5.3.2 Gyro Axis Misalignment

Attitude determination depends significantly on gyro measurements for attitude propagation between sensor measurements. However, the estimate of the gyro bias is corrected by the attitude sensors. Intuition suggests that once the filter has converged, the gyro misalignment should be absorbed in the estimated gyro bias terms. The lack of effect of gyro misalignment is illustrated in Figures 5.11 and 5.12.

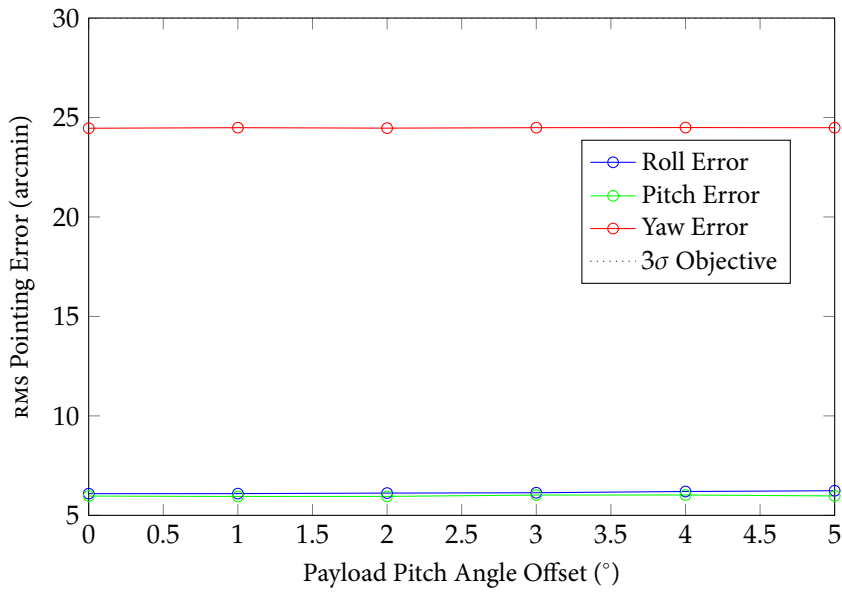


Figure 5.9: RMS Pointing Error Due to Varying Rotor Bearing Axis Misalignment

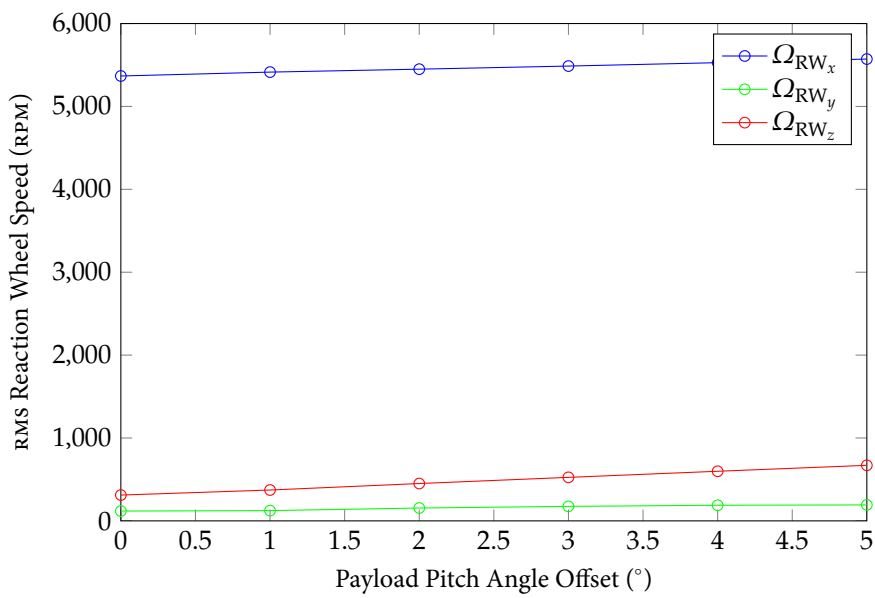


Figure 5.10: RMS Reaction Wheel Speed Increase Due to Varying Rotor Bearing Axis Misalignment

Figure 5.11: RMS Pointing Error
Due to Varying Gyro Misalignment

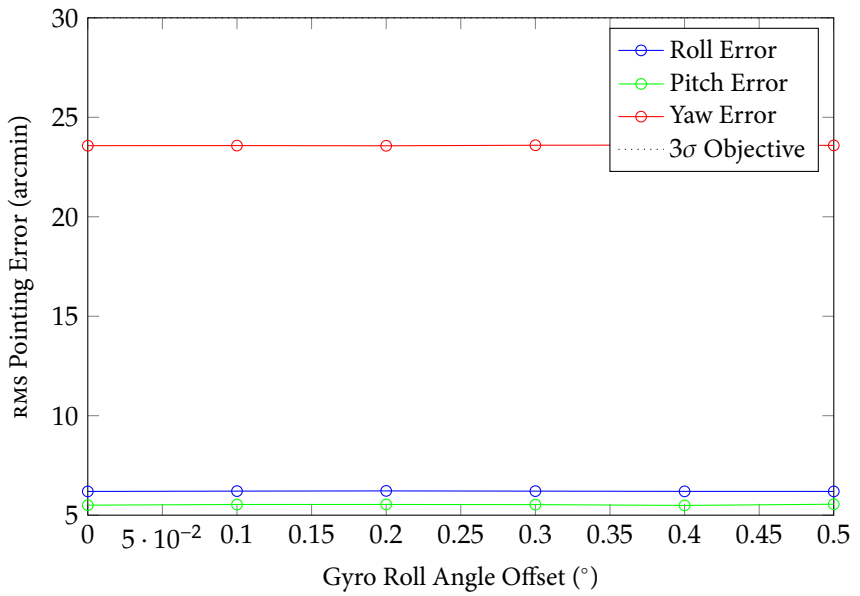
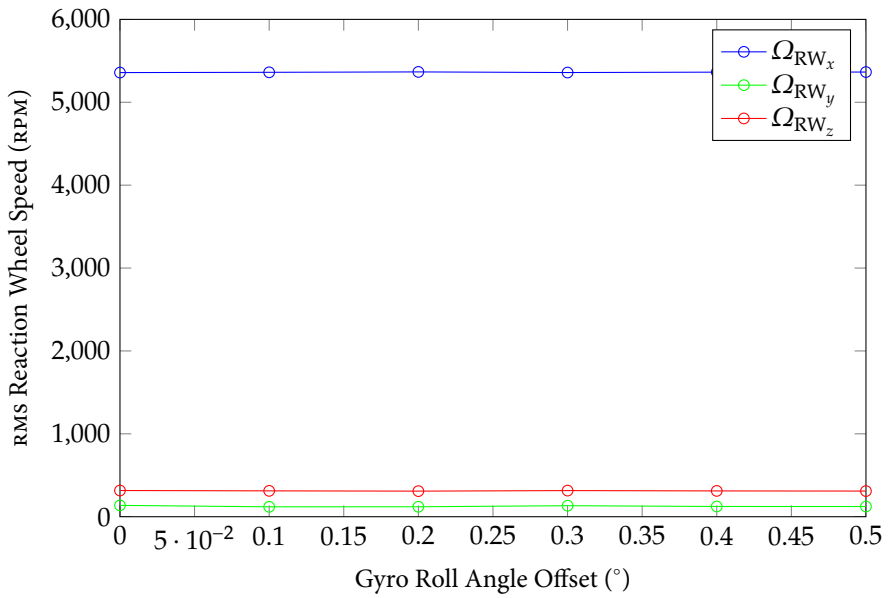


Figure 5.12: RMS Reaction Wheel Speed Increase Due to Varying Gyro Misalignment



5.3.3 Magnetometer Misalignment

Since this sensor is used for yaw determination, this misalignment should result only in yaw errors. Unlike the gyro, misalignment of the magnetometer cannot be corrected by another sensor, though extensive ground-based batch processing with Earth oblateness modelling can derive some yaw information from the limb sensor measurements. Additionally, ground-based batch processing of with the coarse sun sensor measurements should also return useful information. Misalignment of the magnetometer is most likely to be about the spacecraft's x -axis due to circuit board layout.

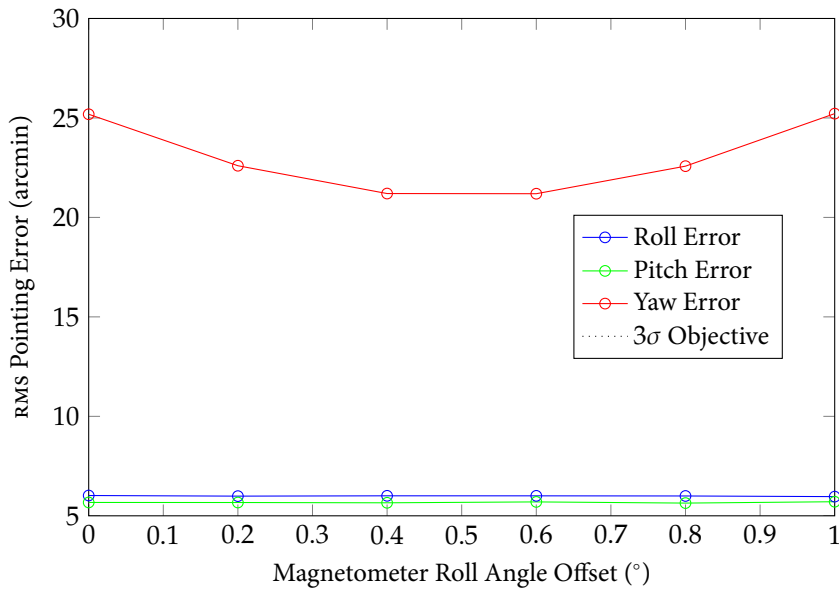


Figure 5.13: RMS Pointing Error Due to Varying Magnetometer Misalignment

5.3.4 Static Earth Sensor Misalignment

Since most of the attitude determination depends on the static Earth sensors, effort must be made to mount them as precisely as possible and characterize their alignment early in the mission by comparing their measurements to the sun sensor data.

5.3.4.1 CROSS-TRACK SENSOR Figures 5.15 and 5.16 show the effects of misalignments of the cross-track sensor.

5.3.4.2 ANTI-RAM SENSOR Figures 5.17 and 5.18 show the effects of misalignments of the anti-ram sensor.

Figure 5.14: RMS Reaction Wheel Speed Increase Due to Varying Magnetometer Misalignment

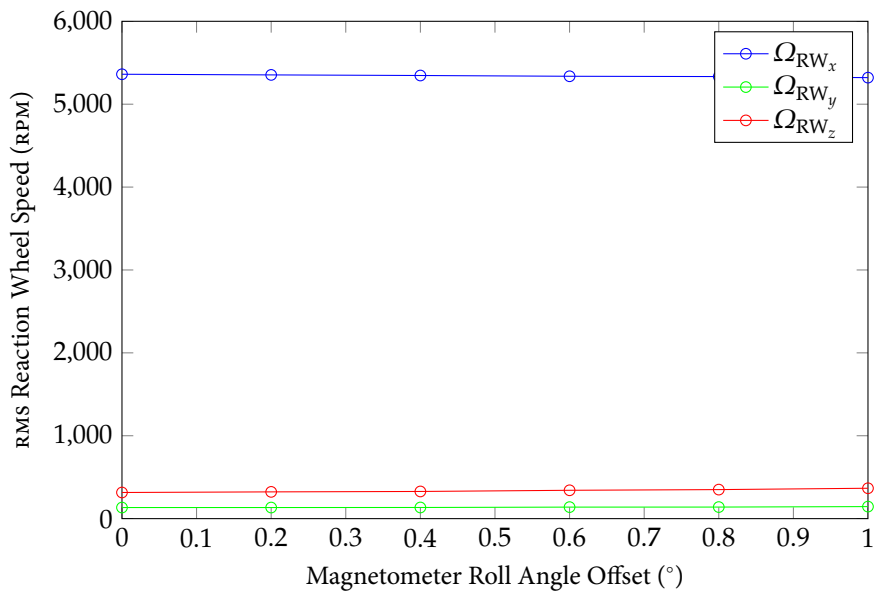
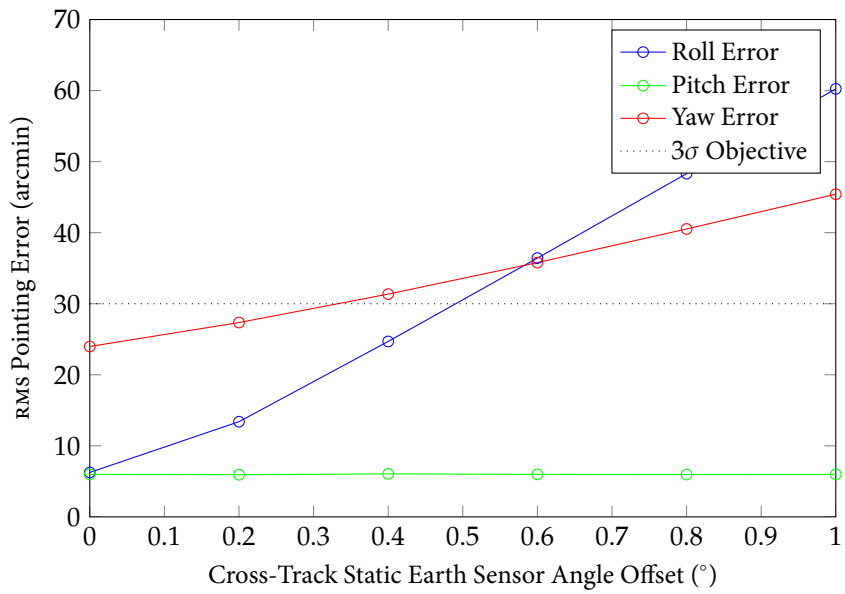


Figure 5.15: RMS Pointing Error Due to Varying Cross-Track Static Earth Sensor Misalignment



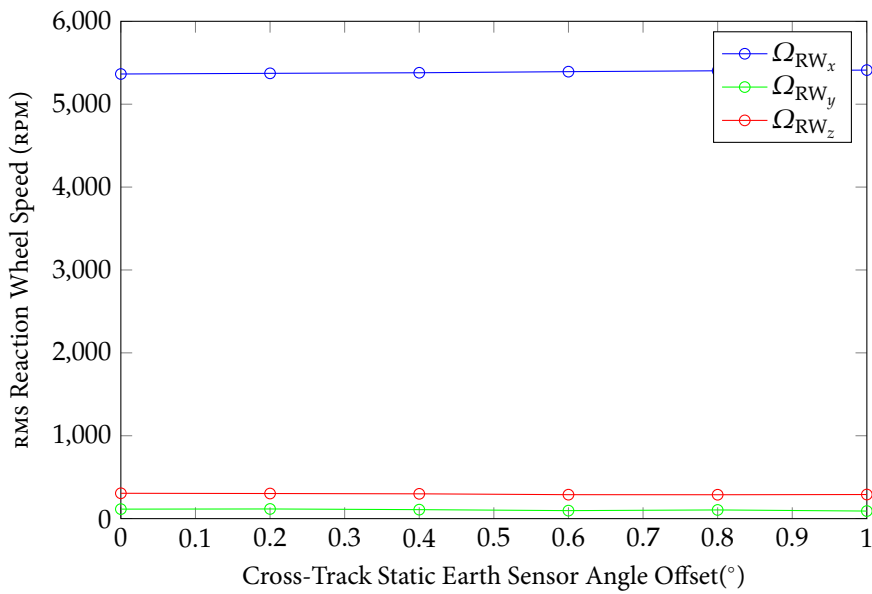


Figure 5.16: RMS Reaction Wheel Speed Increase Due to Varying Cross-Track Static Earth Sensor Misalignment

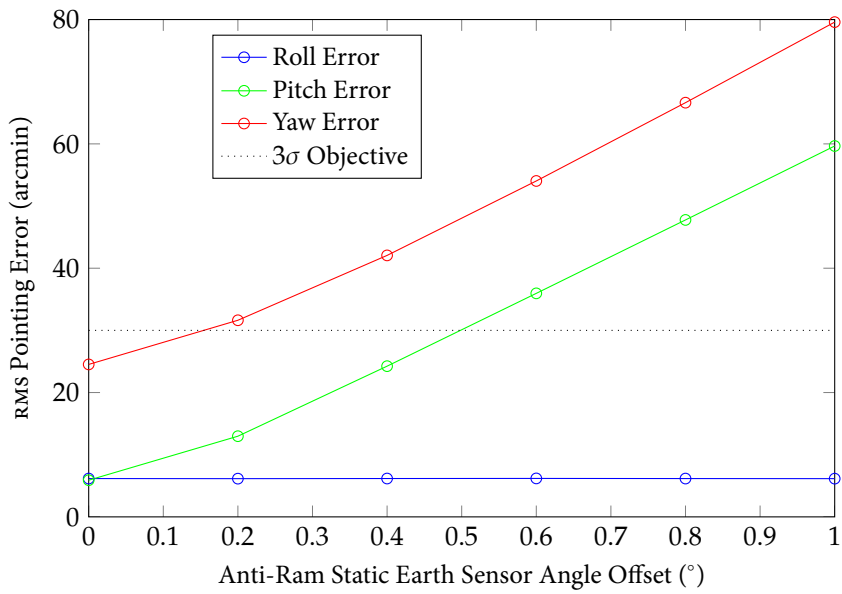
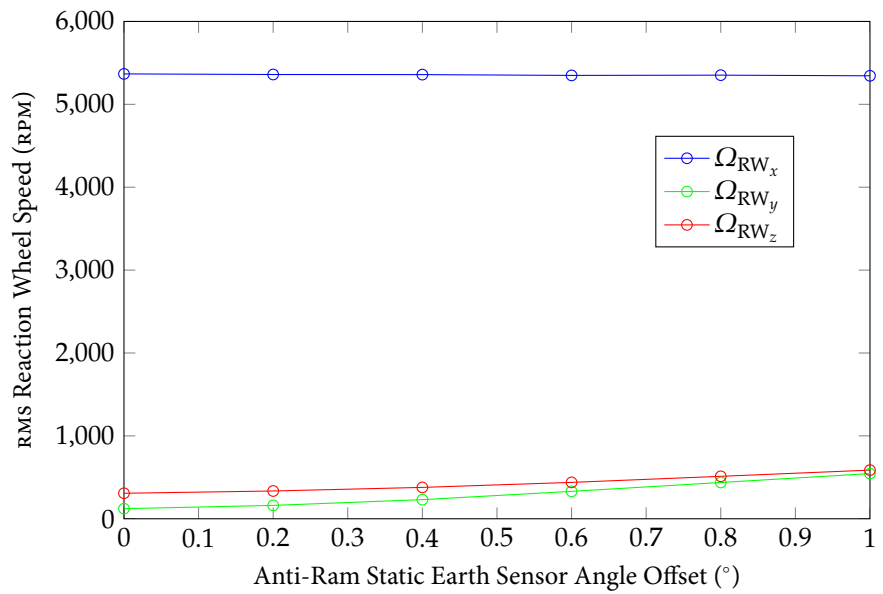


Figure 5.17: RMS Pointing Error Due to Varying Anti-Ram Static Earth Sensor Misalignment

Figure 5.18: RMS Reaction Wheel Speed Increase Due to Varying Anti-Ram Static Earth Sensor Misalignment



6

TESTING

“ The joy of engineering is to find a straight line on a double logarithmic diagram. ”

—Thomas Koenig

UNFORTUNATELY FOR MR.KOENIG, not all of the required hardware arrived in time for actual results publication, but this chapter will still lay out the testing plan. This test program is an evaluation of the performance of the attitude determination and control system for the Micromas spacecraft. Graduate students in the M.I.T. Space Systems Laboratory will conduct the tests.

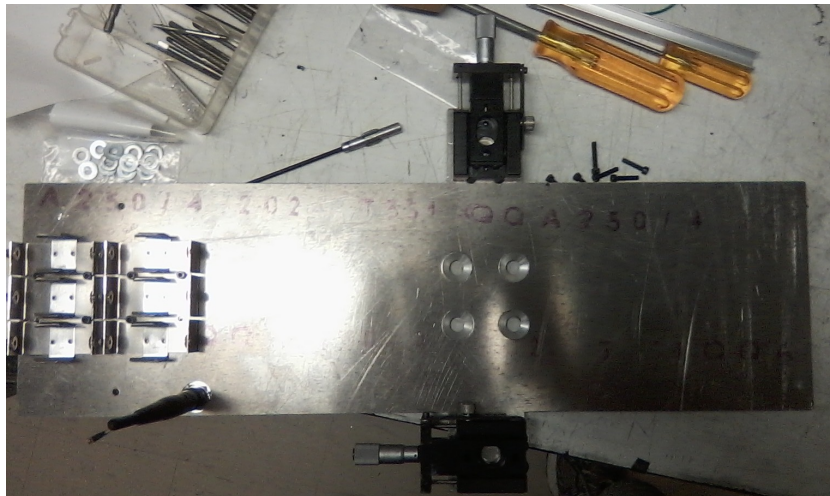


Figure 6.1: Micromas ADCS Test Platform. Note the battery holders on the left, the antenna below them, and the linear stages in the center.

6.1 INTRODUCTION

6.1.1 Background

In order to validate the models developed for simulating the space environment for the development of the spacecraft's estimator and controller, the lab created an attitude dynamics testing facility to emulate the dynamics of the orbital environment as closely as is practicable in atmosphere. A simulacrum of the spacecraft will be used in the testing facility to evaluate the accuracy of the model's predictions as to the estimation and pointing performance of the ADCS design.

6.1.2 Test Item Description

The Micromas ADCS testbed (Figure 6.1), manufactured by the M.I.T. Space Systems Laboratory, will substitute for the actual Micromas spacecraft for the majority of the ADCS dynamical testing. The testbed is equipped with the MAI-400 reaction wheel assembly, six coarse sun sensors mounted analogously to the mounting schema of the actual spacecraft, the majority of the avionics stack of the Micromas spacecraft, the scanner assembly, a mass and inertia mockup of the radiometer payload (Figure 6.2), and six fine mass adjusters for the purposes of centering the testbed's mass with the center of rotation. These fine mass adjusters were borrowed from a previous air bearing project in the lab.¹ Tests on the previous testbed found that gravity gradient torques could be substantial even with small offsets of the testbed's center of mass from its center of rotation. Crowell's solution was to mount small masses on precision linear stages from an optical bench (Figure 6.3).

The MAI-400 reaction wheel assembly includes three orthogonal reaction wheels, tachometers for said wheels, two orthogonal infrared thermopile static Earth sensors, an analog to digital interface for six coarse sun sensors. The avionics stack for the testbed includes engineering models of the bottom and top custom interface boards, a motherboard with a PIC24F microcontroller and MHX Microhard S-band modem and radio, and a ClydeSpace electrical power system with batteries (Figure 6.4).

This testbed is considered functionally representative of the flight spacecraft for the purposes of this evaluation.

6.1.3 Test Objectives

The overall test objective of this effort is to determine the performance of the ADCS with comparisons to the ADCS simulation predictions. Specific test objectives include the following:

6.1.3.1 RATE DAMPING Determine the magnetic dipoles and torques produced by the magnetic torque coils, detumbling time, and rate determination accuracy of the ADCS testbed operating in the B-dot rate damping mode and statistically compare with the damping rates and times predicted by the ADCS simulation.

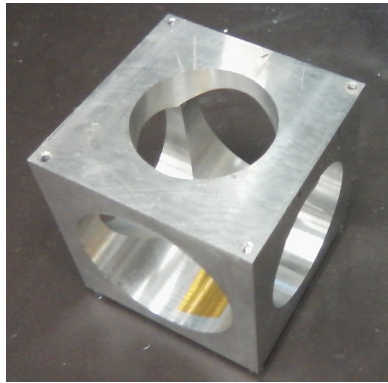


Figure 6.2: Radiometer Payload Inertia Mockup

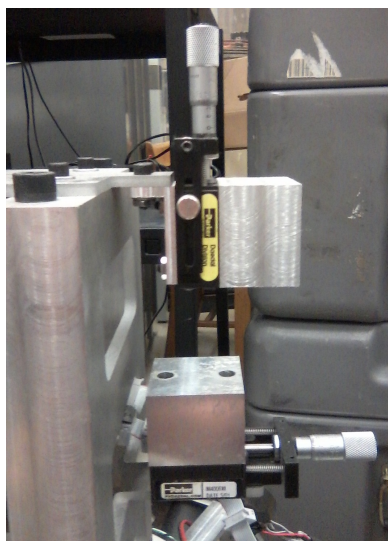


Figure 6.3: Linear Stage Mass Adjusters from the Crowell Testbed

6.1.3.2 SLEW Determine the maximum slew rate available to the testbed, the torques produced by the reaction wheels, and the slew time and accuracy of the testbed operating in the slew mode and statistically compare with the slew rates, times, and pointing accuracy predicted by the ADCS simulation.

6.1.3.3 STABILIZATION Determine the attitude determination accuracy, attitude control accuracy, and rate control of the testbed operating in the stabilization mode (which is the nominal mode of operation for the spacecraft) and statistically compare with the accuracies predicted by the ADCS simulation.

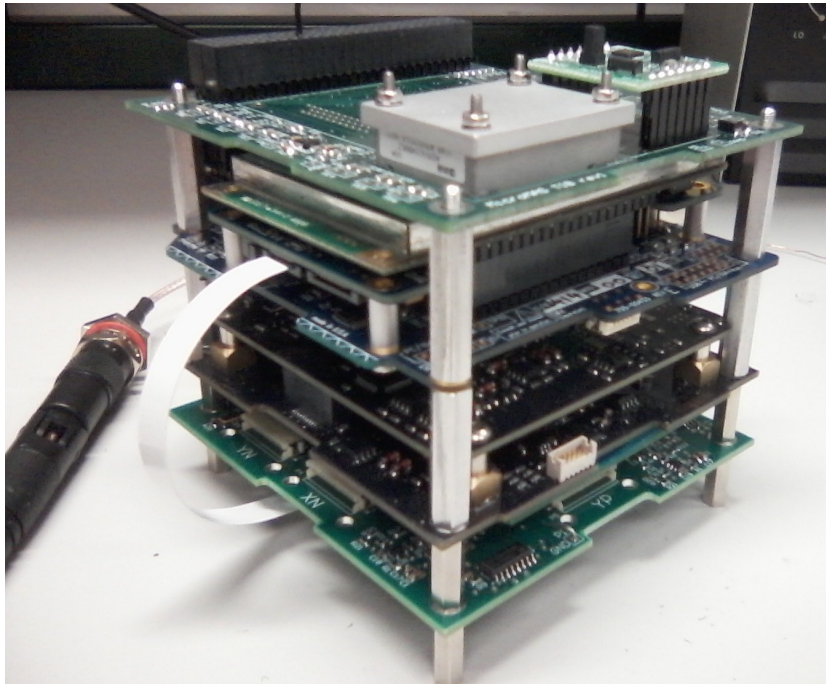


Figure 6.4: Micromas Test Avionics Stack. The two components on the top interface board are the IMU and magnetometer, the board below them houses the Microhard modem and PIC24F microcontroller, and two boards below that are the ClydeSpace EPS. The bottom board houses the sun sensor interface and the MAI-400 interface.

6.1.3.4 PAYLOAD SPINUP Determine the transient torque produced by the payload during spinup, the attitude determination accuracy, the attitude control accuracy, and rate control of the testbed operating in the stabilization mode while spinning up the payload from zero rotation and statistically compare with the torques and accuracies predicted by the ADCS simulation.

6.1.4 Limitations

Operating the testbed in the atmosphere of the laboratory will produce drag effects that are difficult to model and do not reflect the drag conditions on orbit. Also, the gravity gradient torque behaves differently for an object on orbit versus the testbed. Additionally, the testbed's range of slew cannot exceed 30 degrees in the two horizontal axes.

6.1.5 Test Resources

6.1.5.1 TEST FACILITIES The M.I.T. Space System Laboratory's attitude dynamics testing facility consists of a three-degree-of-freedom air bearing (see Figure 6.5) with unlimited rotation about the vertical axis and 30 degrees of rotation about the two horizontal axes, a dynamically controllable three-degree-of-freedom Helmholtz cage with a uniform field volume slightly less than a cubic meter (Figure 6.6), a stationary fixed sun simulator, and a revolving Earth limb thermal simulator (Figure 6.7).²

Figure 6.6 shows the air bearing pedestal contained within the Helmholtz cage (left) and the Helmholtz cage's drivers and amplifiers (rack on the right).

Instrumentation additional to the testbed's integrated sensors includes an external camera and computer to track the fiducial markers on the testbed to provide a truth measurement for slew rate and pointing angle adapting the algorithms developed for the VERTIGO project.³ Also, a separate computer running the spacecraft simulation will collect the sensor and actuator data via radio and compare them real-time to the ADCS simulation.

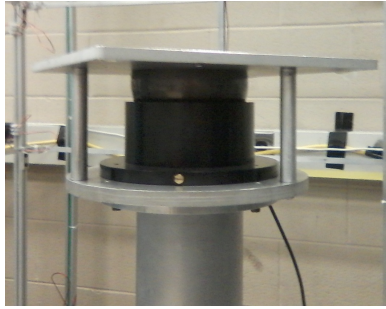


Figure 6.5: 3-DoF Hemispherical Air Bearing

² Prinkey, "CubeSat Attitude Control Testbed Design: Merritt 4-Coil Per Axis Helmholtz Cage and Spherical Air Bearing".



Figure 6.6: 3-DoF Air Bearing and 3-DoF Helmholtz Cage and Drivers

6.2 TEST AND EVALUATION

This section presents the detailed objectives and measures of performance for each test case. Testing is scheduled to take place over the months of June and July 2013.

6.2.1 General Test Objectives

The overall test objective of this effort is to determine the performance of the ADCS with comparisons to the ADCS simulation predictions for the purposes of model validation.

6.2.2 Objective 1: Detumbling Mode

6.2.2.1 MEASURE OF PERFORMANCE 1: STATE TRAJECTORY Determine the magnetic dipole produced by the MAI-400 magnetic torque coils, the torque produced by these torque coils acting against the magnetic field, the duration of the detumbling operation to steady state, and the rate of the spacecraft as measured by the MAI-400's differencing algorithm, the rate determined by the testbed's IMU, and the rate determined by the external machine vision rotation sensor.

6.2.2.2 INSTRUMENTATION REQUIREMENTS

- Success Criterion

Data collection will be considered complete after data from five detumbling mode runs have been collected. The initial rates for these runs should be approximately 2, 4, 6, 8, and 10 degrees per second.

- Evaluation Criterion

The data will be considered satisfactory after they have been converted to consistent units between data sources and found to agree with each other in order of magnitude.

- Final Data Products

For each tipoff rate, the state trajectories and control histories as determined by the onboard testbed computer and the external truth sensor will be collected and plotted against each other in the test report. A plot of their differences over the test duration will also be included.

- Data Requirements

The magnetic dipole commanded by the MAI-400 magnetic torque coils, the local magnetic field as measured by the on-board magnetometer, and the rate of the spacecraft as measured by the MAI-400's differencing algorithm, testbed's IMU, and the external machine vision rotation sensor will be collected for every time step of the experiment. Additionally, the duration of the detumbling will be collected via stopwatch.

- Algorithms/Processes

The magnetic torque produced by the magnetic torque rods is the cross-product of the magnetic dipole moment produced by the torque rods and the local magnetic field. When including the control law in the equation, a proportional control torque appears, minus the uncontrollable axis about



Figure 6.7: Revolving Earth Limb Simulator. The air bearing pedestal is the cylinder in the lower left, and the two kapton-covered hotplates attached to the arm simulate the Earth's horizon.

the local magnetic field line:

$$\begin{aligned}
 \tau &= m \times B \\
 &= \frac{k}{B^T B} (\omega \times B) \times B \\
 &= \underbrace{-k\omega}_{\substack{\text{standard derivative} \\ \text{control term}}} + k \underbrace{\frac{\omega^T B}{B^T B} B}_{\substack{\text{vector projection} \\ \text{of } \omega \text{ onto } B}}
 \end{aligned} \tag{6.1}$$

- Test Methodology

The testbed will be configured to initialize with no ADCS control mode and switch to its detumbling mode after a command from the remote computer. Initial tipoff rate will be provided via a digital impulse from a test administrator. After the initial rate has been established and recorded, the test administrator will command the testbed to begin rate damping. The remote computer and the truth sensor computer will record data through the experiment until the spacecraft has reached its steady-state angular velocity.

- Expected Results

It is expected that the state values gathered during testing will be very close to those predicted by the dynamical simulation. The current estimated detumbling time for the spacecraft with an initial tipoff rate of 10 degrees per second is c. 90 minutes.

6.2.2.3 MEASURE OF PERFORMANCE 2: SIMULATION COMPARISON Validation of the simulation results will be accomplished via a statistical analysis of the dipole, torque, detumbling duration, and rate determination from each of the detumbling mode tests.

- Success Criteria

Data collection will be considered complete after five detumbling mode runs are complete. These runs should include tipoff rates of up to 10 degrees per second.

- Evaluation Criteria

The ADCS simulation will be considered satisfactory if the predicted state values at each time step are greater than the collected values from this test. A 95-percent one-sided confidence interval (student's *t*-distribution) will be used to determine the statistical significance of the data collected when compared to the simulation. For statistical clarification, the following are the null (H_0) and alternate (H_1) hypotheses:

$$H_0 : s \leq \mu, \tag{6.2a}$$

where s represents the sample mean (collected data), and μ represents the population mean (simulation prediction); and

$$H_1 : s > \mu. \tag{6.2b}$$

An increase to the simulation prediction may be required to give the 95-percent confidence. If so, an appropriate recommendation will be made as to how the simulation should be altered to effect the increase.

- Final Data Products

A table containing the statistical analysis numbers will be included in the test report. A plot of the student's t -distribution with the confidence interval shown will be included in an appendix.

- Algorithms/Processes

To determine the 95-percent confidence interval using the student's t -distribution, the following equation will be used:

$$\mu \in \left(-\infty, x + \frac{t_{\alpha/2, n-1} s}{\sqrt{n}} \right). \quad (6.3)$$

- Test Methodology

This equation will be used with the appropriate values for the collected data. The resulting value will be compared to the simulation. If the resulting value is greater or significantly less, then a recommendation will be made to alter the simulation to reconcile the results.

- Expected Results

It is expected that the simulation value will be very close to the value gathered during testing. The simulation currently offers no method for providing a confidence interval—therefore, if the test is conducted with the same initial tipoff rates as those in the simulation, there is a 50-percent probability that any given detumbling duration will exceed the predicted value.

6.2.3 Mission Suitability

The MICROMAS spacecraft will be evaluated for its ability to meet the ADCS requirements. Specific areas to be addressed are the pointing knowledge, reaction wheel saturation time, and power draw. The analysis team must be careful not to extrapolate to performance not tested (e.g., rapid slewing while spinning the payload)—in such cases, a recommendation for further testing is instead warranted.

7

CONCLUSIONS

“MIT doesn’t know when to quit designing,” they said. “They have a bunch of prima donnas who want to make everything perfect regardless of how long it takes.”

—Dick Battin¹

¹ Battin, “Some Funny Things Happened on the Way to the Moon”

The simulation results show that the current control design meets the requirements laid out in Chapter 1.

Future Work

- The next step in estimator design is to explore redundancy in attitude determination. Does our ADS degrade gracefully with the loss of a single sensor? How can we adapt to different configurations?
- The next step in estimator implementation is include failure detection and correction. By monitoring state-error estimate noise covariance growth and measurement errors in the Kalman filter, we can determine when the filter is producing bad data and may diverge.
- The next step in simulation and testing is to thoroughly characterize the hardware to ensure that it is in agreement with the product specification sheets.

7.1 NOVEL WORK

This thesis synthesized previous work on ADCS estimator and controller design to produce an attitude control system to meet tight pointing requirements in a small spacecraft with limited processor capabilities. The dynamical simulation used to verify the estimator and controller and the test setup used to validate the simulation are both extensible to future cubesat missions. ■

BIBLIOGRAPHY

- Andrews, Stephen F., Stephen Bilanow, and Frank Bauer. "Recent Flight Results of the TRMM Kalman Filter". AIAA Paper 2002-5047. Monterey, CA: AIAA/AAS Astrodynamics Specialist Conference, 2002 (cit. on p. 16).
- Andrews, Stephen and Wendy Morgenstern. "Design, Implementation, Testing, and Flight Results of the TRMM Kalman Filter". AIAA Paper 98-4509. Guidance, Navigation, and Control Conference, Aug. 1998 (cit. on pp. 13, 16).
- Bar-Itzhack, I. Y. and Y. Oshman. "Attitude Determination from Vector Observations: Quaternion Estimation". In: *IEEE Transactions on Aerospace and Electronic Systems* 21.1 (Jan. 1985), pp. 128–36 (cit. on p. 16).
- Bate, Roger R., Donald D. Mueller, and Jerry E. White. *Fundamentals of Astrodynamics*. New York: Dover Publications, 1971 (cit. on pp. 20, 57).
- Battin, Richard H. "The Theodore von Kármán Lecture: Some Funny Things Happened on the Way to the Moon". AIAA Paper 89-0861. Reno, Nevada: 27th Aerospace Sciences Meeting, Jan. 1989 (cit. on pp. 37, 42, 79).
- Bhandari, Dan D. V. "Spacecraft Attitude Determination with Earth Albedo Corrected Sun Sensor Measurements". ISBN 87-90664-26-4. Ph. D. Dissertation. Aalborg, Denmark: Aalborg University, Aug. 2005 (cit. on p. 42).
- Bierman, Gerald J. *Factorization Methods for Discrete Sequential Estimation*. Orlando, FL: Academic Press, 1977 (cit. on p. 54).
- Bilimoria, Karl D. and Bong Wie. "Time-Optimal Three-Axis Reorientation of a Rigid Spacecraft". In: *Journal of Guidance, Control, and Dynamics* 16.3 (June 1993), pp. 446–52 (cit. on p. 54).
- Blackwell, W. J. et al. "Improved All-Weather Atmospheric Sounding Using Hyperspectral Microwave Observations". In: *Geoscience and Remote Sensing Symposium (IGARSS), 2010 IEEE International*. Honolulu, HI: IEEE, July 2010, pp. 734–37 (cit. on p. 13).
- Bradley, Ben K. et al. "Earth Orientation Parameter Considerations for Precise Spacecraft Operations". AAS Paper 11-539. Girdwood, AK: AAS/AIAA Astrodynamics Specialist Conference, Aug. 2011 (cit. on p. 21).
- Brown, Robert Grover and Patrick Y. C. Hwang. *Introduction to Random Signals and Applied Kalman Filtering: With MATLAB Exercises and Solutions*. 3rd ed. New York: Wiley, 1997 (cit. on pp. 49, 52, 53).

- Chen, L. C. and J. R. Wertz. "Analysis of SMS-2 Attitude Sensor Behavior Including OABIAS Results". Technical Memorandum NASA-CR-189266, NAS 1.26:189266, csc/TM-75/6003. Computer Sciences Corporation, Apr. 1975 (cit. on p. 42).
- Chobotov, Vladimir A. *Spacecraft Attitude Dynamics and Control*. Orbit, a Foundation Series. Malabar, FL: Krieger, 1991 (cit. on p. 38).
- Coffee, Brian G., Kerri Cahoy, and Rebecca L. Bishop. "Propagation of Cube-Sats in LEO Using NORAD Two Line Element Sets: Accuracy and Update Frequency". (to be published). Boston, MA: AIAA Guidance, Navigation, and Control Conference, Aug. 2013 (cit. on p. 46).
- Crassidis, John L. and John L. Junkins. *Optimal Estimation of Dynamic Systems*. 2nd ed. Chapman & Hall/CRC Applied Mathematics & Nonlinear Science 24. Boca Raton, FL: CRC Press, 2012 (cit. on pp. 16, 51).
- Crowell, Corey Whitcomb. "Development and Analysis of a Small Satellite Attitude Determination and Control System Testbed". S.M. Thesis. Cambridge, MA: Massachusetts Institute of Technology, 2011 (cit. on p. 72).
- Eterno, John S. "Attitude Determination and Control". In: *Space Mission Analysis and Design*. Ed. by Wiley J. Larson and James R. Wertz. 3rd ed. Vol. 8. Space Technology Library. El Segundo, CA: Microcosm Press, 1999, pp. 354–380 (cit. on p. 27).
- Fallon, Lawrence III. "Gyroscope Models". In: *Spacecraft Attitude Determination and Control*. Ed. by James R. Wertz. Vol. 73. Astrophysics and Space Science Library. Dordrecht, The Netherlands: D. Reidel Publishing Company, 1978, pp. 266–70 (cit. on p. 43).
- Farrenkopf, R. "Generalized Results for Precision Attitude Reference Systems Using Gyros". AIAA Paper 74-903. Anaheim, CA: Mechanics and Control of Flight Conference, Aug. 1974 (cit. on p. 50).
- Finlay, C. C. et al. "International Geomagnetic Reference Field: The Eleventh Generation". In: *Geophysical Journal International* 183.3 (2010), 1216–30 (cit. on p. 40).
- Fleming, Andrew, Pooya Sekhavat, and I Michael Ross. "Minimum-Time Re-orientation of a Rigid Body". In: *Journal of Guidance, Control, and Dynamics* 33.1 (Feb. 2010), pp. 160–70 (cit. on p. 54).
- Galante, Joseph M. and Robert M. Sanner. "A Nonlinear Adaptive Filter for Gyro Thermal Bias Error Cancellation". AIAA Paper 2012-4475. Minneapolis, MN: AIAA Guidance, Navigation, and Control Conference, Aug. 2012 (cit. on p. 50).
- Gottlieb, Robert G. "Fast gravity, Gravity Partials, Normalized Gravity, Gravity Gradient Torque and Magnetic Field: Derivation, Code and Data". Contractor Report NASA CR-188243. Houston, TX: McDonnell Douglas Space Systems, Feb. 1993 (cit. on p. 58).
- Grewal, Mohinder S. and Angus P. Andrews. *Kalman Filtering: Theory and Practice using MATLAB*. 3rd ed. Hoboken, NJ: Wiley, 2008 (cit. on p. 53).

- Grewal, Mohinder S. and James Kain. "Kalman Filter Implementation With Improved Numerical Properties". In: *IEEE Transactions on Automatic Control* 55.9 (Sept. 2010), pp. 2058–68 (cit. on p. 54).
- Hashmall, Joseph A. and Joseph Sedlak. "An Algorithm for Converting Static Earth Sensor Measurements into Earth Observation Vectors". Tech. rep. Greenbelt, MD: Flight Mechanics Symposium, Oct. 2003 (cit. on p. 42).
- Hoots, Felix R. and R. L. Roehrich. "Models for Propagation of NORAD Element Sets". Spacetrack Report No. 3. Colorado Springs, CO: U.S. Air Force Aerospace Defense Command, 1980 (cit. on p. 46).
- Junkins, John L. and James D. Turner. *Optimal Spacecraft Rotational Maneuvers. Studies in Astronautics* 3. Amsterdam: Elsevier, 1986 (cit. on p. 54).
- Keat, J. et al. "Earth Horizon Modeling and Application to Static Earth Sensors on TRMM Spacecraft". In: Greenbelt, MD: Flight Mechanics/Estimation Theory Symposium, May 1995, pp. 229–39 (cit. on p. 58).
- Kimber, Lemon and Bryan W. Welch. "Comparison of Nonlinear Filtering Techniques for Lunar Surface Roving Navigation". Technical Memorandum NASA/TM-2008-215152, E-16352. Cleveland, OH: Glenn Research Center, May 2008 (cit. on p. 53).
- Kuipers, Jack B. *Quaternions and Rotation Sequences: A Primer with Applications to Orbits, Aerospace, and Virtual Reality*. English. Princeton, NJ: Princeton University Press, 1999 (cit. on pp. 22, 48).
- Lefferts, Eugene J., F. Landis Markley, and Malcolm D. Shuster. "Kalman Filtering for Spacecraft Attitude Estimation". AIAA Paper 82-70. Orlando, FL: AIAA 20th Aerospace Sciences Meeting, Jan. 1982 (cit. on p. 16).
- Lerner, Gerald M. "Three-Axis Attitude Determination". In: *Spacecraft Attitude Determination and Control*. Astrophysics and Space Science Library 73. Dordrecht, The Netherlands: Kluwer Academic Publishers, 1978, pp. 420–28 (cit. on p. 42).
- Likins, P. W. "Attitude Stability Criteria for Dual Spin Spacecraft". In: *Journal of Spacecraft and Rockets* 4.12 (Dec. 1967), pp. 1638–43 (cit. on p. 15).
- Markley, F. Landis. "Attitude Determination Using Vector Observations: A Fast Optimal Matrix Algorithm". English. In: *The Journal of Astronautical Sciences* 41.2 (June 1993), pp. 261–80 (cit. on p. 53).
- Markley, F. Landis. "Equations of Motion". English. In: *Spacecraft Attitude Determination and Control*. Ed. by James R. Wertz. Astrophysics and Space Science Library 73. Dordrecht, The Netherlands: Kluwer Academic Publishers, 1978, pp. 510–23 (cit. on p. 22).
- Markley, F. Landis. "Matrix and Vector Algebra". English. In: *Spacecraft Attitude Determination and Control*. Ed. by James R. Wertz. Astrophysics and Space Science Library 73. Dordrecht, The Netherlands: Kluwer Academic Publishers, 1978, pp. 744–57 (cit. on pp. 16, 50).
- Markley, F. Landis. "Optimal Attitude Matrix from Two Vector Measurements". English. In: *Journal of Guidance, Control, and Dynamics* 31.3 (May 2008), pp. 765–68 (cit. on p. 16).

- Markley, F. Landis. "Response to Torques". In: *Spacecraft Attitude Determination and Control*. Ed. by James R. Wertz. Astrophysics and Space Science Library 73. Dordrecht, The Netherlands: D. Reidel Publishing Company, 1978, pp. 498–502 (cit. on p. 26).
- Markley, F. Landis and Frank H. Bauer. "Attitude Error Representations for Kalman Filtering". In: *Journal of Guidance, Control, and Dynamics* 26.2 (Apr. 2003), pp. 311–17 (cit. on p. 48).
- Markley, F. Landis and Frank H. Bauer. "Attitude Representations for Kalman Filtering". AAS Paper 01-309. Goddard Space Flight Center: NASA, 2001 (cit. on p. 48).
- Markley, F. Landis and Frank H. Bauer. *Spacecraft Attitude Determination Methods*. Ithaca, NY, Nov. 2000 (cit. on p. 16).
- Markley, F. Landis and Daniele Mortari. "How to Estimate Attitude from Vector Observations". AAS Paper 99-427. Girdwood, AK: AAS/AIAA Astrodynamics Specialist Conference, Aug. 1999 (cit. on pp. 16, 52).
- Markley, F. Landis and Daniele Mortari. "New Developments in Quaternion Estimation from Vector Observations". In: College Station, TX: Richard H. Battin Astrodynamics Symposium, Mar. 2000 (cit. on p. 16).
- McIntyre, J. E. and M. J. Gianelli. "Bearing Axis Wobble for a Dual Spin Vehicle". In: *Journal of Spacecraft and Rockets* 8.9 (Sept. 1971), pp. 945–51 (cit. on pp. 15, 35).
- Mindell, David A. *Digital Apollo: Human and Machine in Spaceflight*. Cambridge, MA: The M.I.T. Press, 2008 (cit. on p. 16).
- Murrell, J. "Precision Attitude Determination for Multimission Spacecraft". AIAA Paper 78-1248. Guidance and Control Conference, Aug. 1978 (cit. on p. 16).
- Natanson, Gregory and Jonathan Glickman. "A Study of TRMM Static Earth Sensor Performance Using On-Orbit Sensor Data". AIAA Paper 2000-4245. Denver, CO: AIAA Guidance, Navigation, and Control Conference, May 2000 (cit. on pp. 16, 42).
- Ortiz, Vincent Michael. "Evaluation of Energy-Sink Stability Criteria for Dual-Spin Spacecraft". M.S. Thesis. Monterey, CA: Naval Postgraduate School, June 1994 (cit. on p. 15).
- Phenneger, M. C. et al. "Infrared Horizon Sensor Modeling for Attitude Determination and Control: Analysis and Mission Experience". Technical Memorandum NASA-TM-86181. Greenbelt, MD: Goddard Space Flight Center, Mar. 1985 (cit. on pp. 42, 58).
- Phillips, Kevin J. "Linearization of the Closed-Loop Dynamics of a Dual-Spin Spacecraft". In: *Journal of Spacecraft and Rockets* 8.9 (Sept. 1971), pp. 938–45 (cit. on p. 15).
- Pong, Christopher et al. "High-Precision Pointing and Attitude Determination and Control on ExoplanetSat". AIAA Paper 2012-4783. Minneapolis, MN: AIAA Guidance, Navigation, and Control Conference, Aug. 2012 (cit. on pp. 15, 44, 49, 50, 54).

- Potter, James and Robert Stern. "Statistical Filtering of Space Navigation Measurements". AIAA Paper 63-333. Cambridge, MA: AIAA Guidance and Control Conference, Aug. 1963 (cit. on p. 54).
- Prinkey, Meghan. "CubeSat Attitude Control Testbed Design: Merritt 4-Coil Per Axis Helmholtz Cage and Spherical Air Bearing". (to be published). Boston, MA: AIAA Guidance, Navigation, and Control Conference, Aug. 2013 (cit. on p. 74).
- Rogers, Robert M. *Applied Mathematics in Integrated Navigation Systems*. 2nd ed. AIAA education series. Reston, VA: American Institute of Aeronautics and Astronautics, 2003 (cit. on p. 43).
- "Spacecraft Earth Horizon Sensors". English. Special Publication NASA-SP-8033. Dec. 1969 (cit. on p. 42).
- Springmann, John C. et al. "The Attitude Determination System of the RAX Satellite". In: *Acta Astronautica* 75 (June 2012), pp. 120–35 (cit. on pp. 15, 40).
- Standish, E. M. "JPL Planetary and Lunar Ephemerides, DE405/LE405". English. Interoffice Memorandum 312.F-98-048. Pasadena, CA: Jet Propulsion Laboratory, Aug. 1998 (cit. on p. 21).
- Tangyin, Sergei and Malcolm D. Shuster. "The Many TRIAD Algorithms". AAS Paper 07-104. Sedona, AZ: AAS/AIAA Spaceflight Mechanics Meeting, Feb. 2007 (cit. on pp. 16, 53).
- The Astronomical Almanac for the Year 2013 and its Companion The Astronomical Almanac Online: Data for Astronomy, Space Sciences, Geodesy, Surveying, Navigation, and Other Applications*. 2013th ed. Washington: U.S. Government Printing Office, 2012 (cit. on pp. 20, 21).
- Tisa, Paul and Paul Vergez. "Performance Analysis of Control Algorithms for FalconSat-3". English. AAS Paper 06-149. Tampa, FL: 16th AAS/AIAA Space Flight Mechanics Conference, Jan. 2006 (cit. on p. 13).
- Truncale, A., W. Koenigsberg, and R. Harris. "Spectral Density Measurements and Gyro Noise". Report E-2641. Cambridge, MA: M.I.T. Draper Laboratory, Feb. 1973 (cit. on p. 50).
- Tweddle, Brent Edward. "Computer Vision Based Navigation for Spacecraft Proximity Operations". S.M. Thesis. Cambridge, MA: Massachusetts Institute of Technology, 2010 (cit. on pp. 49, 74).
- Vallado, David A and Wayne D McClain. *Fundamentals of Astrodynamics and Applications*. Third Edition. Space Technology Library Volume 21. Hawthorne, CA: Microcosm Press, 2007 (cit. on pp. 20–22, 57, 58).
- Wahba, Grace. "A Least Squares Estimate of Satellite Attitude". English. In: *SIAM Review* 7.3 (July 1965), p. 409 (cit. on p. 16).
- Weinberg, Harvey. "Calibrating iMEMS Gyroscopes". Application Note AN-1049. Norwood, MA: Analog Devices, 2009 (cit. on p. 50).
- Wertz, James R. "Torque-Free Motion". English. In: *Spacecraft Attitude Determination and Control*. Astrophysics and Space Science Library 73. Dordrecht, The Netherlands: D. Reidel Publishing Company, 1978, pp. 487–497 (cit. on p. 32).

- Wertz, James Richard, David F. Everett, and Jeffery John Puschell, eds. *Space Mission Engineering: The New SMAD*. English. Space Technology Library Volume 28. Hawthorne, California: Microcosm Press, 2011 (cit. on p. 38).
- Wie, Bong. *Space Vehicle Dynamics and Control*. English. Ed. by Joseph A. Schetz. 2nd ed. AIAA Education Series. Reston, VA: AIAA, 2008 (cit. on pp. 22, 30).
- Wie, Bong, H. Weiss, and A. Arapostathis. "Quaternion Feedback Regulator for Spacecraft Eigenaxis Rotations". In: *Journal of Guidance, Control, and Dynamics* 12.3 (June 1989), pp. 375–80 (cit. on p. 55).
- Wright, W. H. "Wobble Correction for a Dual-Spin Vehicle". In: *Journal of Spacecraft and Rockets* 11.4 (Apr. 1974), pp. 255–57 (cit. on pp. 16, 35).